UNIVERSITY OF Southampton

University of Southampton Research Repository
ePrints Soton

Copyright © and Moral Rights for this thesis are retained by the author and/or other copyright owners. A copy can be downloaded for personal non-commercial research or study, without prior permission or charge. This thesis cannot be reproduced or quoted extensively from without first obtaining permission in writing from the copyright holder/s. The content must not be changed in any way or sold commercially in any format or medium without the formal permission of the copyright holders.

When referring to this work, full bibliographic details including the author, title, awarding institution and date of the thesis must be given e.g.

AUTHOR (year of submission) "Full thesis title", University of Southampton, name of the University School or Department, PhD Thesis, pagination

http://eprints.soton.ac.uk

UNIVERSITY OF SOUTHAMPTON

FACULTY OF NATURAL AND ENVIRONMENTAL SCIENCES

School of Chemistry

NUCLEIC ACID DENATURATION AT AN ELECTRODE SURFACE

by

Robert Peter Johnson

Thesis for the degree of Doctor of Philosophy

September 2011

UNIVERSITY OF SOUTHAMPTON

ABSTRACT

FACULTY OF NATURAL AND ENVIRONMENTAL SCIENCES

School of Chemistry

Doctor of Philosophy

NUCLEIC ACID DENATURATION AT AN ELECTRODE SURFACE

By Robert Peter Johnson

This thesis describes the development and improvement of an assay for the detection and discrimination of DNA sequences based on surface enhanced Raman spectroscopy (SERS) and electrochemically driven denaturation. A DNA helix can be immobilised at a nano-structured gold electrode and then denatured into its constituent components by driving the potential at the surface cathodic (electrochemical melting). This denaturation is typically monitored by observing changes in the SERS spectra of a reporter molecule attached to one of the two strands that comprises the helix. The ease of denaturation (defined as the potential required to denature half of the DNA at the electrode surface) was found to be directly related to the thermodynamic stability of the duplex. In addition to dsDNA structure, the effect of varying environmental conditions during an electrochemical melting experiment (pH and ionic strength) was explored.

A number of possible mechanisms for electrochemical melting have been ruled-out, including electrostatic repulsion from the electrode surface. It was found that peptide nucleic acid (an uncharged analogue of DNA) could be denatured electrochemically. Local pH changes were also ruled-out as a possible mechanism through experiments in which the surface pH and electrochemical melting were monitored simultaneously.

A method for detecting surface immobilised DNA without the need for the attachment of a synthetic label is described. This presents a significant milestone towards the development of a point-of care electrochemical melting assay, because no synthetic pre-treatment of the sample is required prior to analysis.

Table of Contents

1. Introduction 1
1.1. DNA Structure, Detection and Discrimination 1
1.1.1. Overview 1
1.1.2. The Structure of DNA 2
1.1.3. Mutations in DNA 4
1.1.4. Detection and Discrimination of DNA 4
1.2. Surface Enhanced Raman Spectroscopy 7
1.2.1. Raman Spectroscopy 7
1.2.2. Surface Enhanced Raman Spectroscopy (SERS) 8
1.2.3. Sphere Segment Void Substrates 12
1.3. Detection and Discrimination of DNA using SSV Substrates 16
1.3.1. SERS Melting 16
1.3.2. Electrochemical Melting 17
1.4. Research Objectives and Thesis Overview 18
1.5. References 20
2. Materials and Methods 25
2.1. Materials 25
2.2. Reference Electrodes 26
2.3. Preparation of Sphere Segment Void Substrates 26
2.3.1. Assembly of Colloidal Templates 26
2.3.2. Electrodeposition 28
2.3.3. Characterisation 30
2.4. Raman Spectroscopy 30
2.5. DNA Preparation 31
2.5.1. Synthesis 31
2.5.2. Structures and Sequences 32
2.5.3. Immobilisation of DNA onto SSV Substrates 34
2.5.4. Surface Coverage Determination 35
2.6. PNA Preparation 37
2.6.1. Structures and Sequences 37
2.6.2. Immobilisation of PNA onto SSV Substrates 37
2.5.5. Surface Coverage Determination 38
2.7. DNA and PNA Denaturation 38
2.7.1. Thermal Denaturation in Solution 38
2.7.2. Thermal and Electrochemical Melting at an SSV Surface 38
2.8. References 40
3. The Effect of Nucleic Acid Structure on Electrochemical Melting 41
3.1. Overview 41
3.2. DNA Thermodynamics 42
3.2.1. The Van't Hoff Equation 42
3.2.2. Nearest Neighbour Models 43
3.3. The Effect of dsDNA Structure on the Melting Potential 44
3.3.1. DNA Preparation and Design 45
3.3.2. Solution Based-Thermal Melting 47
3.3.3 Electrochemical Melting 47
3.4. The Effect of Experimental Temperature on the Electrochemical Melting Potential 54
3.4.1. Electrochemical Cell Calibration 54
3.4.2. Effect of Experimental Temperature on Melting Potential 55
3.5. Electrochemical Melting of Peptide Nucleic Acid 59
3.5.1. Overview 59

3.5.2. Oligonucleotide Design and Probe Immobilisation....60
3.5.3. Surface Coverage Determination....61
3.5.4. Thermal Melting of PNA in Solution....63
3.5.5. Electrochemical Melting of PNA Containing Duplexes....66
3.5.6. Discussion....69
3.6. Summary....72
3.7. References....73
4. The Effect of the Aqueous Environment on Electrochemical Melting....75
4.1. Overview....75
4.2. The Effect of pH on Electrochemical Melting....75
4.2.1 Choice and Calibration of Probe Molecule....76
4.2.2 Use of the pH Probe in Combination with Immobilised dsDNA....78
4.2.3. Use of the pH probe in an Electrochemical Melting Experiment....81
4.3. Effect of Ionic Strength on the Electrochemical Melting Potential....85
4.3.1. Reference Electrode Calibration....87
4.3.2. Effect of Ionic Strength on the Melting Potential....88
4.3.3. Discussion....91
4.3.4. The relationship between Ionic Strength, Strand Length, and Melting Potential....97
4.4. The Effect of Different Cations on the Electrochemical Melting Potential....99
4.4.1. Overview....99
4.4.2. Discussion....101
4.5. Summary....104
4.6. References....105
5. Label Free DNA Detection and Discrimination....107
5.1. Overview....107
5.2. DNA Binding Molecules....109
5.2.1. Modes of Binding....109
5.2.2. Choice of Binding Agent....110
5.3. DNA Preparation and Design....112
5.4. Label Free Detection of DNA....112
5.4.1. Detection of dsDNA at an SSV Surface....112
5.4.2. Peak Assignments and Binding Orientation....115
5.5. Thermally Driven DNA Melting....121
5.5.1. Methylene Blue....121
5.6 Electrochemically Driven Melting....123
5.6.1. The Electrochemistry of Methylene Blue....123
5.6.2. Discrimination of Mutations with Leuco-Methylene Blue....125
5.6.3. Discrimination of Mutations with To-PRO® 3....128
5.7. Summary....131
5.8. References....132
6. Conclusions & Further Work....135
6.1. Overview....135
6.2. Understanding Electrochemical Melting....136
6.2.1. Disproved Mechanisms for Electrochemical Melting....136
6.2.2. Current Theory....139
6.3. Further Work....142
6.3.1. Understanding Electrochemical Melting....142
6.3.2. Improving Electrochemical Melting Assays....143
6.4. References....146

DECLARATION OF AUTHORSHIP

I, ROBERT PETER JOHNSON

declare that the thesis entitled

NUCLEIC ACID DENATURATION AT AN ELECTRODE SURFACE

and the work presented in the thesis are both my own, and have been generated by me as the result of my own original research. I confirm that:

- this work was done wholly or mainly while in candidature for a research degree at this University;
- where any part of this thesis has previously been submitted for a degree or any other qualification at this University or any other institution, this has been clearly stated;
- where I have consulted the published work of others, this is always clearly attributed;
- where I have quoted from the work of others, the source is always given. With the exception of such quotations, this thesis is entirely my own work;
- I have acknowledged all main sources of help;
- where the thesis is based on work done by myself jointly with others, I have made clear exactly what was done by others and what I have contributed myself;
- parts of this work have been published as:

R. P. Johnson, S. Mahajan, M. E. Abdelsalam, R. M. Cole, A. E. Russell, J. J. Baumberg, P. N. Bartlett; SERS from two-tier sphere segment void substrates; *Phys. Chem. Chem. Phys.* **Advance Article, DOI: 10.1039/C1CP21126A**

R. P. Johnson, R. Gao, T. Brown and P. N. Bartlett; Effect of dsDNA structure on electrochemical melting; *Bioelectrochemistry*; **Submitted.**

R. P. Johnson, J. A. Richardson, T. Brown and P. N. Bartlett; Real-time SERS monitoring of local pH conditions during electrochemical melting of dsDNA; Langmuir; **Submitted.**

Signed:

Date: 1st **September 2011**

Acknowledgments

I would like to start by thanking my supervisor Phil Bartlett and my advisor Andrea Russell for all of their help and support; not only during the past three years but also in my final years as an undergraduate as well. Your enthusiasm and passion has been an inspiration and one of the reasons for my continuing interest in science.

Perhaps the most rewarding aspect of my PhD has been the opportunity to work and collaborate with such a wide range of researchers, both from Southampton and elsewhere. I would particularly like to acknowledge the help and expertise provided by Tom Brown and his research group, and specifically, James Richardson, Nittaya Gale, Marta Gerowska and Rachel Gao for the design and synthesis of the nucleic acids used in this project. I would also like to acknowledge those who I have worked with on the SERS project: - Ahmet Celiktas, Jon Speed, Jatin Sinha, Damion Corrigan and Pietro Marafini.

I owe a debt of gratitude to Patrick Hendra for the design and construction of the spectro-electrochemical cells, and Alistair Clarke for the preparation of gold-coated microscope slides that were critical to the success of this work.

Next I would like to thank all of my colleagues and friends from the electrochemistry group with whom I have worked over the past three years, and especially over the course of this year, which at times has not been easy for me. In particular, I would like to express my gratitude to Mara Serrapede, Maciek Sosna, Laura Calvillo, Anna Wise and Matthew Roberts.

Outside of the university, I would like to express my thanks to Shelley and Alan who kindly ‘loaned’ me their office above the Herb Pot when I needed somewhere quiet to write this thesis. I don’t think I’d have made very much progress without all of those cups of tea!

Finally, I’d like to thank all of my family for their continuing support and encouragement. At last, you can tell people that I am going to get a ‘proper’ job!

1. Introduction

1.1. DNA Structure, Detection and Discrimination

1.1.1. Overview

Deoxyribose nucleic acid (DNA) contains the genetic information required for development and function of all life on Earth. Since the initial determination of the DNA duplex structure by Watson and Crick in 1953[1] there has been intense interest in understanding the way in which DNA stores and replicates information. By interrogating the structure of DNA, it is possible to obtain a wealth of useful information about a person. DNA based testing, commonly known as genetic testing, has found significant use in clinical healthcare for the diagnosis of genetic diseases such as cystic fibrosis[2] and Huntington's disease[3]. More recently, genetic testing has generated interest in the emerging field of pharmacogenetics[4-7], where a person's pre-disposition to certain medications can be determined. Such knowledge can help healthcare professionals choose the drugs that provide the highest medical efficacy whilst minimising side-effects.

Whilst genetic testing has proven to be a highly beneficial tool in early diagnosis, it is generally expensive and requires highly trained personnel working in a laboratory. Bringing genetic testing directly to the patient would significantly reduce the cost and length of time required for diagnosis and allow for medical treatment decisions to be taken earlier. To this end, a number of research groups are working towards the development of new technologies for the rapid and cost-effective detection and discrimination of DNA.

In this chapter, methods of DNA detection and discrimination that are currently in the public domain are reviewed, assessing in particular their potential for integration into a point-of-care environment. Of interest to this project is the detection and discrimination of DNA using surface enhanced Raman spectroscopy (SERS); and this technique is reviewed in detail in Section 1.2, with particular emphasis on the choice of substrate. Since the discrimination of different sequences of DNA generally relies

on the ability to detect changes in DNA structure, this chapter begins with an overview of nucleic acid chemistry and how genetic mutations can cause changes to DNA.

1.1.2. The Structure of DNA

DNA is a biological polymer consisting of repeating nucleotide monomer units linked together by a sugar-phosphate backbone (Figure 1.1). The monomer unit itself is one of four nitrogen-containing heterocyclic bases; adenine, guanine cytosine or thymine. A short, single strand of DNA consisting of multiple repeating monomer units is termed an oligonucleotide. The bases that are present together with the sequence in which they appear comprise the primary structure of DNA.

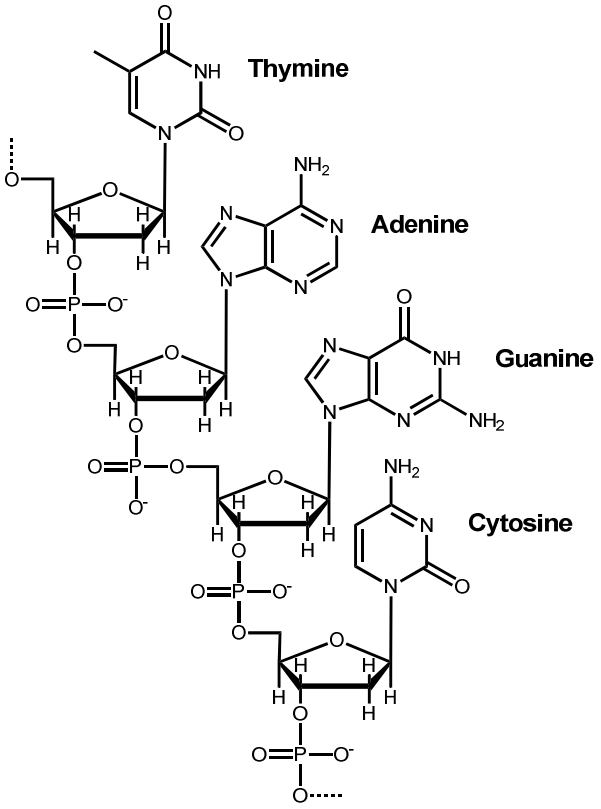

Figure 1.1. The structure of single-stranded DNA (ssDNA). The bases thymine, adenine, guanine and cytosine that comprise the DNA sequence are linked together by a sugar-phosphate backbone.

Two single strands of DNA can form a duplex through a hydrogen bonding interaction between bases, which comprises the DNA secondary structure. This base-

pairing interaction is highly specific, where adenine (A) binds preferentially with thyamine (T), and guanine (G) binds preferentially with cytosine (C). Two hydrogen bonds form between AT base-pairs, whilst three hydrogen bonds form between GC base-pairs (Figure 1.2). This base-pairing interaction plays a crucial role in the stability of double-stranded (duplex) DNA, where increasing the GC content will result in an increase in stability because of the increased number of hydrogen bonds holding the two strands together.

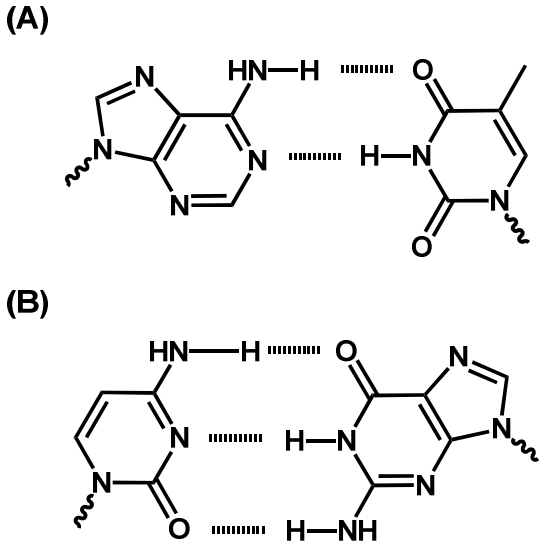

Figure 1.2. The base-pair interactions between (A) adenine and guanine; and (B) thymine and cytosine. AT base pairs are linked by two hydrogen bonds, whilst GC base-pairs are linked by three hydrogen bonds.

Whilst the stability of double-stranded DNA (dsDNA) is primarily determined by its base-pair composition, the overall sequence also plays an important role[8]. The two constituent strands that comprise dsDNA form the shape of a double helix, and this gives rise to favourable stacking interactions between the overlapping pi-orbitals of neighbouring base pairs. The helical shape a DNA duplex comprises its tertiary structure.

1.1.3. Mutations in DNA

Mutations in DNA are caused by changes in the genomic sequence, and can be caused spontaneously during DNA replication or arise as a result of irradiative or chemical damage.

Typically, mutations are categorised based on their effect on DNA structure[9]; and are described as point-mutations, insertions or deletions. Point mutations are the result of the exchange of one nucleotide for another, with the most common being an exchange of a purine base for a purine base (e.g. A to G), or a pyrimidine base for a pyrimidine base (e.g. C to T). This is termed a transition. Less common is the exchange of purine base for a pyrimidine base, or vice versa. This is termed a transversion. Insertions and deletions are caused by the addition or removal of nucleotides from the DNA sequence. Mutations result in serious health consequences, such as incorrect protein expression or even inhibition of protein expression altogether. Point mutations, insertions and deletions all result in a sequence of base-pairs that is different to the wild-type (non-mutated) sequence[9].

1.1.4. Detection and Discrimination of DNA

The most common method of discriminating between different DNA structures, and in particular, mutations, is through differential denaturation. A typical differential denaturation experiment is performed by monitoring the ease with which dsDNA is denatured when, for example, the temperature or solution composition is changed. A mutated sequence will possess base pair mismatches and/or other defects when bound to a probe designed to be perfectly complementary to the wild-type (non-mutated) target. The resulting duplex will therefore be less stable, and more readily denatured[10].

The existing methods described in the literature can be broadly categorised as either solution or surface based. The most widely used solution based methods are fluorescent detection schemes such as those used in Molecular Beacons[11], Taqman®[12], Scorpions®[13], or Hybridization Probes[14]. In these methods, typically, a gradual change in fluorescent signal is monitored during temperature ramping to bring about denaturation of dsDNA in solution[15].

Surface based methods have gained prominence because of the attraction of an array-based approach to the detection of mutations, the opportunity to control the conditions locally at a surface, and the ability to produce simple, portable biosensor devices. In these experiments the target DNA strand is hybridised to a probe strand immobilised at the surface. Denaturation of the DNA duplex can be achieved either thermally (that is by ramping the temperature) or by using a series of solutions with sequentially reduced salt concentrations (stringency washing).

Various surface-based approaches have been used to detect DNA. In particular, electrochemical techniques[16-18], including redox probes[19-23] and impedance[24-27], have proven popular because only relatively simple and low-cost equipment is required. This is of particular advantage when consideration is given to the development of a point of care device.

Recently, Nasef *et al.* have demonstrated that differential pulse voltameterry (DPV) can be combined with thermal denaturation of DNA to discriminate between a perfectly complementary and mutated target oligonucleotide[28, 29]. The signal from the redox probe reduces as the DNA denatures and moves away from the surface. The redox probe used can be either covalently bound (in the case of ferrocene[28]) or intercalated (in the case of methylene blue[29]).

DNA detection at a surface has also been demonstrated with refractive index measurements using surface plasmon resonance[30, 31] and measurements of mass change using the quartz crystal microbalance (QCM)[32, 33]. Fluorescent based methods, which are commonly used for solution based differential denaturation studies, have also been employed for surface bound detection and discrimination of mutations[34, 35].

Surface enhanced Raman or resonant Raman scattering SERS has recently gained interest as an alternative method in DNA detection assays because it possesses several key advantages, particularly in comparison to fluorescence[36-39]. These include the ability to make multiplexed measurements because of the narrow line width (~ 10 nm) of the SERS signals, the molecular specificity of SERS spectra[37, 40, 41], the flexibility in the choice of labels[39, 42, 43], insensitivity to quenching by oxygen or other

species[36], and excellent sensitivity[39, 44]. In addition the SERS process is highly surface selective, unlike fluorescence, so that there is no interference from labelled molecules not bound at the surface[45, 46].

Several techniques to detect DNA using SERS have been developed, including the use of roughened silver surfaces and the use of colloidal particles. Roughened silver surfaces have been used by Vo-Dinh and colleagues to demonstrate detection of DNA either directly attached to the roughened surface[38, 47, 48], or via a nitrocellulose membrane intermediate[49]. Flocculating colloidal particles have also been shown by Graham and co-workers to be an effective SERS method for DNA detection[39, 42, 43, 50-52], including the use of different labels for genotype multiplexing[52] and the ability to detect DNA directly from a PCR product without purification[53].

More elaborate detection methods utilising SERS have also been reported. Halas *et al.* have recently demonstrated a label-free method for DNA detection based on the substitution of adenine in a surface-immobilised probe sequence with 2-amino purine[54]. This substitution removes the characteristic adenine bands that typically dominate the SERS spectra of DNA[55]. A target oligonucleotide can then be detected by re-appearance of adenine bands in the spectra upon hybridisation.

Work within our research group has led to the development of a SERS based platform for detecting and discriminating mutations in DNA sequences that utilises a thin structured gold film with a regular array of spherical cavities, a sphere segment void (SSV) surface[56, 57]. The development of these surfaces and their use for DNA detection and discrimination assays is discussed further in Section 1.3. First, the principles of Raman and surface enhanced Raman spectroscopy are described in more detail.

1.2. Surface Enhanced Raman Spectroscopy

1.2.1. Raman Spectroscopy

Raman spectroscopy is a non-destructive method for analysing and identifying molecules based on the way in which they scatter incident photons. When a light source, commonly a laser, is incident on a molecule, the constituent photons will be scattered. This can be either elastically (termed Raleigh scattering) or inelastically (termed Raman scattering). Raman scattering was first demonstrated in 1928, and named after its discoverer, C.V. Raman[58].

Inelastic scattering arises from a two-step process. First, the absorption of a photon by a molecule causing it to enter a 'virtual' electronic state of higher energy. Second, the relaxation from this virtual electronic state to a vibrational energy level in the ground electronic state that is either lower or higher in energy than that from which it was initially excited. The result is the release of a photon with a net change in energy, as illustrated in Figure 1.3.

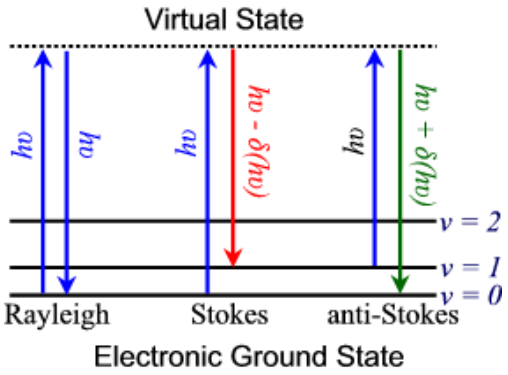

Figure 1.3. Raman scattering results in a net change in energy of the scattered photon, whereas in Raleigh scattering there is no net change in the photon energy.

The Raman effect is a result of a molecule's intrinsic 'polarisability'. Under the influence of an applied electric field, an oscillating dipole will be induced in the electron cloud surrounding a molecule, momentarily raising the molecule to an excited state. This is the virtual state referred to in Figure 1.3, so called because it is not a fixed energy level such as an excited electronic or vibrational state.

Raman spectroscopy offers significant advantages over other complementary methods such as infra-red and fluorescence spectroscopy in that it can detect several molecular species simultaneously, requires no sample preparation, and can be performed through glass and water, both of which are transparent to visible laser and Raman scattered light. However, the Raman scattering effect is incredibly weak, with on1y 1 in 10^7 incident photons scattered. Low-level detection is therefore incredibly difficult unless steps are taken to enhance the scattering effect.

1.2.2. Surface Enhanced Raman Spectroscopy (SERS)

Surface enhanced Raman spectroscopy (SERS) was first observed in 1974 for pyridine absorbed at a roughened silver electrode[59]. The observed spectra were a million fold more intense than anticipated with conventional Raman. Three years later, Van Duyne and Jeanmarie[60] and (independently), Albrecht and Creighton[61] attributed this enhancement to a localized electromagnetic field at the electrode surface.

Although even today the exact mechanism by which the enhancement occurs is still subject to some debate, the generally accepted theory suggests that there are two main contributory factors. Firstly, the charge transfer enhancement, which arises from the chemisorption of the adsorbate at the metal surface[62-65]; and secondly, the electromagnetic enhancement, a non-adsorbate specific enhancement arising from the focusing of the electric field via plasmon resonances at the metallic surface[66, 67]. The second and larger electromagnetic enhancement relies on the presence of localised electromagnetic fields, which are strongly dependent on the morphology (structural features) of the enhancing substrate at the nanoscale.

Early SERS substrates were often nothing more than electrochemically roughened gold[68, 69] or silver[70-72] surfaces. Whilst very good SERS enhancement for these surfaces has been reported, the reproducibility is inherently very poor, as surface plasmon generation at the right energy occurs only at positions on the substrate where the surface morphology is correct. These positions are generally described as ‘hot spots’. In addition to gold and silver, SERS has also been demonstrated at the

roughened surface of a number of transition metals by Tian and co-workers[73], although the observed enhancement is significantly lower than for that observed for gold or silver.

Designing a substrate with the 'ideal' morphology for SERS enhancement has been of intense interest in the SERS community for over forty years[74-76], and in that time a number of novel SERS substrates have been described. Typically, these substrates fall into two distinct categories: - colloidal nanoparticles and rationally designed arrays.

Metallic nanoparticles can be used as SERS substrates under conditions in which they are permitted to aggregate. SERS measurements have been demonstrated from colloidal suspensions of gold[77-79], silver[78, 80], platinum[81, 82] and even gallium[83] nanoparticles. A significant advantage of colloidal particles is that they are easy to prepare and can be easily adapted to a wide range of analytical applications. In particular, colloidal particles have shown promise for SERS studies *in vivo*; where they can be injected into live cells in order to obtain spectral information. This general method has been utilised successfully for the detection of tumours in mice[84, 85] and for mapping local pH changes of living cells[86-88].

Rationally designed arrays are metal substrates that have regular, repeating features on the nanoscale. This greater control over the surface morphology means that, unlike colloidal particles or roughened substrates, the observed SERS enhancement is more reproducible from place to place. In addition, rationally-designed substrates typically have a much longer shelf-life due to their increased robustness. These types of substrate provide much better reproducibility than randomly roughened surfaces or colloids. A wide range of examples of rationally designed nanostructures for SERS have been described, including nano-rings[89], nano-triangles[90], nano-flowers[91], spherical nano-shells[92, 93], nano-pits[76] and nano-tip arrays[94].

Advanced lithographic techniques, such as electron beam lithography, are common 'top-down' methods for preparing rationally-designed SERS substrates[74]. Lithographic methods involve preparing a nano-structured template, and then coating it with a SERS-active coinage metal such as gold or silver. For example, in electron beam lithography, a concentrated electron beam is used to pattern a responsive

material known as a 'photo-resist'. A solvent is then used to rinse away those areas of the photo-resist exposed to the electron beam, leaving a nano-patterned array.

Unfortunately, most basic lithographic techniques are incapable of producing surface morphologies small enough for SERS enhancement[74], and those more advanced methods that are, such as electron beam lithography, require very expensive and specialist equipment. In contrast, self-assembled arrays of colloidal particles can be used to prepare templates for SERS substrates using simple bench-top methods in the laboratory[75]. The 'bottom-up' approach of colloidal particle assembly has a significant cost advantage over the soft-lithographic techniques. Colloidal particle templates have been used extensively to prepare a range of SERS substrates with differing nanoscale morphologies[95-101] (Figure 1.4).

Typically, the colloidal particle template is used as a mask, onto or through which a metal is deposited. Sometimes metal deposition is followed by dissolution of the template. Since it is possible to change both the sphere-size and metal deposition thickness, there is some element of control over the final morphology of substrates prepared in this way. For example, the absorption wavelength of the metal film-over-nanosphere substrate (Figure 1.4c) can be altered over the visible range by changing the thickness of the deposited silver[99]. This is very important for 'tuning' the substrate to give the largest possible SERS enhancement by controlling the plasmonics – a theme discussed further in Section 1.2.3.

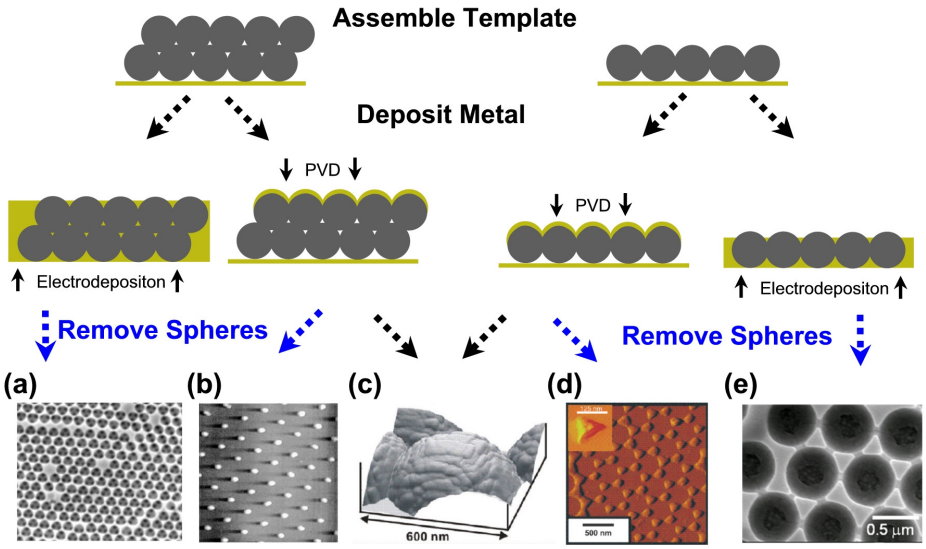

Figure 1.4. A wide-variety of nano-structured SERS substrates can be prepared from colloidal particle arrays, including (a) metal honeycombs[101] (b) nano-dots[96, 97] (c) film-over-nanosphere[99]. (d) nano-triangles[95, 98] and (e) sphere segment voids[100].

A number of groups have shown that large SERS enhancements can be obtained from inverse opal ('honeycomb') arrays[101-103]. However, the precise number of layers in the honeycomb and the geometry of the top surface are generally not systematically controlled, leading to variations in SERS enhancement across the substrate.

Research in our group has led to the development of the sphere segment void (SSV) substrate; a thin layer metallic film with a regular array of spherical cavities prepared from just a monolayer of hexagonally close packed polystyrene spheres[100, 104-107]. SSV substrates have been prepared from a variety of SERS-active metals, including gold[100, 105-109], silver[110], platinum[111] and palladium[111, 112]. By correctly choosing both the sphere size and the deposition height through the template, it is possible to obtain a tuneable electromagnetic enhancement with only ~10% standard deviation in signal variation across the surface[100, 113].

1.2.3. Sphere Segment Void Substrates

The tunable and reproducible nature of the SERS enhancement from sphere segment void (SSV) substrates is due to the consistency with which surface plasmons can be generated at the substrate surface. Surface plasmons give rise to the SERS effect via coupling with incident radiation of comparable energy at the substrate surface, which is then scattered by the adsorbed molecule. Since the scattered radiation is also coupled by plasmons, the plasmons must be resonant with both the incoming and outgoing light for the maximum SERS enhancement.

A surface plasmon is defined as a coherent (collective) oscillation of electrons at a metal-dielectric interface[114] (Figure 1.5). When coupled with an incident electromagnetic field (e.g. from a laser), and under the right conditions, these surface plasmons can enter an excited state[106, 114]. These excited plasmons are sometimes referred to as surface plasmon polaritons.

Plasmon polaritons cannot form on a flat surface because of a 'momentum mismatch' between the incident photons and the surface plasmons pinned at the metal-dielectric boundary[106]. One of the ways of providing the additional momentum required is by structuring the surface of metal, either through nano-scale defects caused by roughening or by utilising a period metal diffraction grating[115, 116], such as that provided by the regular structure of the SSV substrate[106, 107, 114].

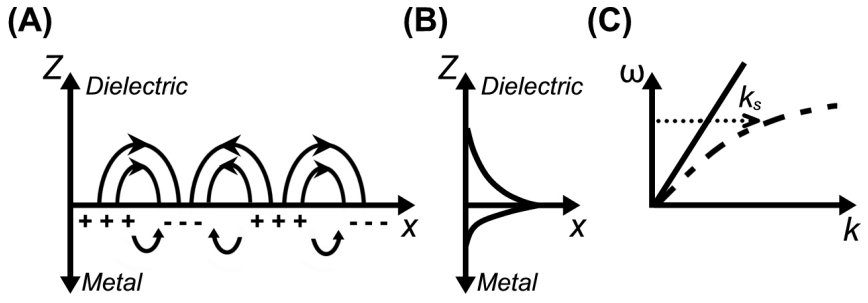

Figure 1.5. (A) Surface plasmons are electromagnetic waves that propagate along the surface of a metal. (B) Since the wave decays exponentially across the interface into both media, the plasmons are pinned to the metal-dielectric boundary. (C) Additional momentum is required to match the momentum of surface plasmons (k_s; dashed line) at the metal-dielectric boundary for a given frequency ω. In a SSV substrate this is provided through scattering of incident photons at a periodic metal diffraction

grating[106].

Three main types of plasmon mode can be distinguished on a sphere segment void structure[106, 107, 114]:

- Those that reside on the top surface of the sample; which are referred to as the Bragg plasmons (Figure 1.6). These plasmons modes are delocalised, and can propagate over relatively long distances across the substrate.
- Those that reside within the truncated voids of the sample; which are referred to as the Mie plasmons (Figure 1.6). These plasmons modes are highly localised and confined to within the voids.
- Those that reside at the upper rim of the voids. These plasmon modes are referred to as Rim plasmons. These modes are thought to be due to the build up of charge at the rim of the voids.

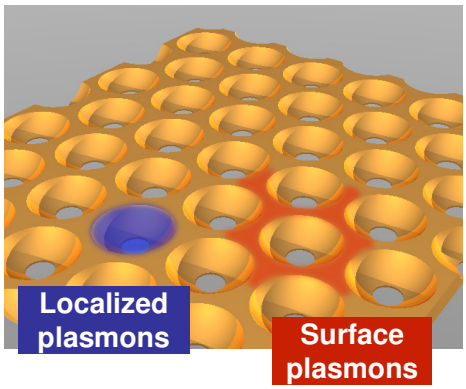

Figure 1.6. Approximate locations of plasmons distinguishable on an SSV substrate. De-localised surface (Bragg) plasmon modes propagate across the top surface, whilst localised Mie plasmons modes are confined to within the segment voids. A third type of plasmon mode, rim plasmons, are theorised to occupy the upper rim of the segment voids. (not shown).

The energy and appearance of a particular plasmon mode is highly dependent on the structural morphology of substrate, which for a sphere segment void structure, can be controlled by altering the sphere diameter from which the template is constructed or the height through the template to which gold is deposited.

Consider a sphere segment void substrate prepared from a template with spheres of diameter 600 nm. At low deposition thicknesses, the morphology of the substrate resembles shallow dishes (Figure 1.7a). Plasmon modes associated with the top-

surface dominate this type of structure, and can be modelled effectively with Bragg diffraction. These types of plasmon are termed 'Bragg plasmons'. The energy of these types of plasmon is highly dependent on the angle of the incident radiation responsible for generating the plasmon[106, 107].

As the deposition thickness increases to approximately half the sphere height (0.5d), the continuity of the top surface is disrupted (Figure 1.7b), and Bragg plasmons are no longer generated at the substrate. Beyond 0.5d, the top-surface begins to re-form, and Bragg plasmons are again present at the substrate surface (Figure 1.7c). The presence of truncated spherical cavities at these deposition thicknesses also gives rise to plasmons that are highly localised within the cavity. These plasmons can be modelled with Mie theory, and are termed 'Mie plasmons'. These modes are independent of the angle of incident radiation, and their energy typically decreases with an increasing film height[106, 107].

The third type of plasmon, the Rim mode, appears only when there is a complete rim about the top edge of the cavity. This occurs when the film height is below 0.3d (Figure 1.7a) and above 0.7d (Figure 1.7c). These modes form as a result of a build-up of charge at the void rim, and are referred to as 'Rim modes'.

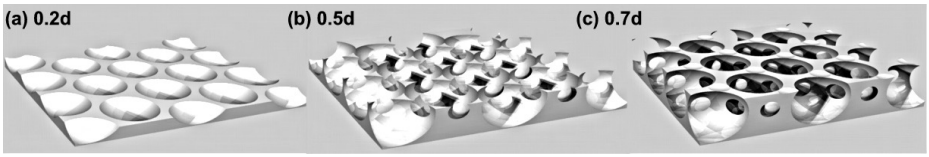

Figure 1.7. Computer generated cross-sectional images of an SSV substrate at (a) 0.2d, (b) 0.5d and (c) 0.7d, where (d = 600 nm). The type of plasmon mode that can be generated at the surface is highly dependent on the morphology. Bragg modes are present when the top surface is continuous (a, c). Rim plasmons are present when there is a complete rim about the top edge of the cavity (a, c). Mie modes are present only when there are truncated spherical voids (c).

In addition to the three types of plasmon mode described above, many more plasmon modes can be observed experimentally at an SSV substrate. These are typically a result of plasmon hybridisation, or interference (coupling) between plasmon modes[117, 118]. This is similar to the formation of a molecular orbital from the mixing of two atomic orbitals. Plasmon modes can couple only if they are of the same symmetry[117,

[118]. Overlap ('mixing') of the Mie and Rim plasmon modes results in the formation of two new energy modes; one of higher energy around 2eV, and one of lower energy. The higher energy mode generated by this plasmon hybridisation is particularly useful for achieving resonance with a 633 nm pump laser (633 nm = 1.96 eV).

Thus, by controlling the surface morphology it is possible to obtain plasmon mixing in such a way as to 'tune' the electromagnetic fields to be resonant at a selected wavelength. In the case of the work presented in this thesis, substrates were tuned to be resonant at a pump wavelength of 633 nm, which corresponds to a 600 nm void diameter and a film height of 450 nm – 480 nm. The highly tuneable properties of the SSV substrate make it ideal for a variety of analytical studies. Furthermore, the robust all-metallic nature of the SSV substrate mean that it is ideally suited for use as an electrode – so that analytes at the surface can be studied with both SERS and electrochemistry simultaneously[110, 113].

1.3. Detection and Discrimination of DNA using SSV Substrates

1.3.1. SERS Melting

We have recently developed a SERS based platform for detecting and discriminating mutations in DNA sequences utilising sphere segment void (SSV) surfaces[56, 119]. In a typical DNA discrimination assay using SERS on an SSV surface a modified probe strand is first attached to the gold surface via a series of three di-thiol linkers at a coverage of around 1.5×10^{12} molecules per cm^2. The surface density is low to ensure that hybridisation with DNA from solution is not sterically hindered[34, 35, 56]. The surface is then passivated by treatment with mercaptohexanol. This prevents the non-specific adsorption of DNA at the gold surface[120, 121], and reorients the probes DNA strand to stand out from the surface[120-123]. The target DNA strand with a Raman active label is introduced from solution and allowed to hybridise to the bound probe strand to form double-stranded DNA (dsDNA) at the surface. By applying an external driving force, the bound dsDNA can be denatured, and the ease with which this is achieved is a function of both the base-pair composition and any mutations present.

The gradual denaturation of the dsDNA on the surface is monitored by measuring the intensity of the Raman signal from the labelled target DNA. The SERS enhancement is very strongly surface selective, and as the labelled DNA diffuses away from the enhanced electromagnetic field localised within ~50 nm of the SSV surface that is responsible for the SERS enhancement, the signal intensity drops. The point at which half of the surface-bound dsDNA has denatured (when the Raman signal is reduced to 50% of its maximum) is defined as the melting point. The external force used to drive duplex denaturation on the SSV surface can be solution composition (stringency washing), temperature (thermal melting), or electrode potential (electrochemical melting).

1.3.2. Electrochemical Melting

Electrochemical melting is of particular interest as a driving force for DNA denaturation because it offers several advantages as the basis of a DNA discrimination method in point of care applications, where there is a particular demand for simple, low-cost devices that can produce rapid results.

The first reported observation of electrochemical melting (or 'unwinding') of native DNA was at a mercury drop electrode in 1974[124, 125]. Despite several other observations of electrochemically driven DNA denaturation in the interlude[126, 127], there was no attempt to utilise electrochemical denaturation to discriminate between DNA duplexes until 1997, when Sonowski *et al.* immobilised DNA in a silicon nitride gel at a platinum electrode[128]. They demonstrated that it was possible to discriminate a duplex containing a single-base mismatch from wild-type by observing the relative drop in florescence upon application of a negative bias. In 2001 Heaton *et al.* demonstrated the discrimination of a two-base mismatch by monitoring changes in surface plasmon resonance upon exposure of gold-immobilised duplexes to an electric field of -300 mV vs. Ag/AgCl[129]. Electrochemical denaturation has also been observed with chemiluminesence[130] and impedance[131]. However, in all of these examples a constant bias voltage was used, and because of the low magnitude of the applied voltage only partial denaturation was observed. More recently, complete DNA denaturation has been monitored with the aid of square wave stripping voltammetery[132], although the technique was not utilised to discriminate between duplexes of different structures.

In contrast, the SERS electrochemical melting assays developed by our group have proven effective at discriminating between multiple DNA structures, and has been utilised to discriminate mutations in the gene responsible for coding for the Cystic Fibrosis Transmembrane Regulator (CFTR) protein[56]. Discrimination of the wild type 1653C/T single nucleotide polymorphism and ΔF508 triplet deletion using spectra recorded from just 12,000 molecules of surface bound dsDNA (0.02 attomole) has been demonstrated. The same approach has also been used to discriminate STR sequences as used in DNA fingerprinting[133] at a similar level and through

measurements on DNA produced by asymmetric PCR without the need for a subsequent purification step[56].

Electrochemical melting offers several advantages as the basis of a simple DNA discrimination method, particularly in point of care applications. However, the mechanism behind electrochemical melting is not well established, and in order to design better discrimination assays it is desirable to both understand the underlying mechanism at the electrode surface, and to relate electrochemical melting to existing models describing DNA stability.

1.4. Research Objectives and Thesis Overview

The research described in this thesis builds upon the initial SERS electrochemical melting experiments that were used to discriminate between mutations and short tandem repeats in DNA. The overall research objective has been to better understand the electrochemical melting mechanism, and to improve the technology such that it can become viable in a point-of-care environment.

In Chapter two, the equipment, chemicals and methods used throughout this thesis are described. A detailed description of the preparation of sphere segment void (SSV) substrates and their use in electrochemical melting assays is given.

In Chapter three, the effect of dsDNA structure on electrochemical melting is described. The stability of an electrode-immobilised duplex under an applied potential is discussed in the context of existing thermodynamic (nearest neighbour) models that describe the thermal stability of dsDNA in solution. The work described in this chapter has laid the foundation for the design of better electrochemical discrimination assays in the future.

In Chapter four, the effect of the buffer composition on electrochemical melting is explored in order to better understand the mechanism responsible for the denaturation. Firstly, the effect of solution pH on duplex stability is described. A novel method for monitoring both DNA denaturation and the local pH simultaneously using surface

enhanced Raman spectroscopy (SERS) is demonstrated. Secondly, the effect of solution ionic strength and ion composition on duplex stability is described. The observed changes in stability are explained in terms of the presence of the electrical double layer (EDL) at the dsDNA immobilised electrode surface.

In Chapter five, the discrimination of mutations in the CTFR gene without the need to attach a Raman label dye to the desired target nucleotide is demonstrated. The results present a significant milestone towards the development of a point-of-care electrochemical melting assay, because label-free detection methods offer a way of detecting the target nucleotide directly and without the need for synthetic treatment prior to measurement.

In Chapter six, conclusions and suggestions for further work are presented. The results of the previous chapters are discussed in terms of the insight gained into electrochemical melting, and a mechanism for the denaturation is proposed. Finally, some future experiments that should help further our understanding of the process are proposed.

1.5. References

1. J. D. Watson and F. H. C. Crick, *Nature*, 1953, **171**, 737-738.
2. B. Kerem, J. Rommens, J. Buchanan, D. Markiewicz, T. Cox, A. Chakravarti, M. Buchwald and L. Tsui, *Science*, 1989, **245**, 1073-1080.
3. F. O. Walker, *Lancet*, 2007, **369**, 218-228.
4. S. J. Gardiner and E. J. Begg, *Pharmacol. Rev.*, 2006, **58**, 521-590.
5. U. A. Meyer, *Nat. Rev. Genet.*, 2004, **5**, 669-676.
6. R. M. Weinshilboum and L. Wang, *Annu. Rev. Genom. Hum. G.*, 2006, **7**, 223-245.
7. D. B. Goldstein, S. K. Tate and S. M. Sisodiya, *Nat Rev Genet*, 2003, **4**, 937-947.
8. J. SantaLucia and D. Hicks, *Annu. Rev. Biophys. Biomol. Struct.*, 2004, **33**, 415-440.
9. R. H. Garrett and C. M. Grisham, *Biochemistry*, Brooks/Cole, Cengage Learning, Boston, MA, 2010.
10. M. J. Heller, *An. Rev. Biomed. Eng.*, 2002, **4**, 129-153.
11. S. Tyagi and F. R. Kramer, *Nat Biotech*, 1996, **14**, 303-308.
12. P. M. Holland, R. D. Abramson, R. Watson and D. H. Gelfand, *Proc. Nat Acad. Sci.*, 1991, **88**, 7276-7280.
13. D. Whitcombe, J. Theaker, S. P. Guy, T. Brown and S. Little, *Nat Biotech*, 1999, **17**, 804-807.
14. C. T. Witter, M. G. Hermann, A. A. Moss and R. P. Rasmussen, *Biotechniques*, 1997, **22**, 130 - 131.
15. K. M. Ririe, R. P. Rasmussen and C. T. Wittwer, *Anal. Biochem.*, 1997, **245**, 154-160.
16. T. G. Drummond, M. G. Hill and J. K. Barton, *Nat Biotech*, 2003, **21**, 1192-1199.
17. J. J. Gooding, *Electroanalysis*, 2002, **14**, 1149-1156.
18. K. Kerman, M. Kobayashi and E. Tamiya, *Meas. Sci. Technol.*, 2004, **15**, R1 - R11.
19. K. Hashimoto, K. Ito and Y. Ishimori, *Anal. Chem.*, 1994, **66**, 3830-3833.
20. T. Ihara, M. Nakayama, M. Murata, K. Nakano and M. Maeda, *Chem. Commun.*, 1997, 1609-1610.
21. K. M. Millan and S. R. Mikkelsen, *Anal. Chem.*, 1993, **65**, 2317-2323.
22. J. Wang, D. Xu, A.-N. Kawde and R. Polsky, *Anal. Chem.*, 2001, **73**, 5576-5581.
23. C. J. Yu, Y. Wan, H. Yowanto, J. Li, C. Tao, M. D. James, C. L. Tan, G. F. Blackburn and T. J. Meade, *J. Am. Chem. Soc.*, 2001, **123**, 11155-11161.
24. T.-Y. Lee and Y.-B. Shim, *Anal. Chem.*, 2001, **73**, 5629-5632.
25. C.-Z. Li, Y.-T. Long, J. S. Lee and H.-B. Kraatz, *Chem. Commun.*, 2004, 574-575.
26. X. Li, J. S. Lee and H.-B. Kraatz, *Anal. Chem.*, 2006, **78**, 6096-6101.
27. Y.-T. Long, C.-Z. Li, T. C. Sutherland, H.-B. Kraatz and J. S. Lee, *Anal. Chem.*, 2004, **76**, 4059-4065.
28. H. Nasef, V. Beni and C. K. O'Sullivan, *Electrochem. Commun.*, 2010, **12**, 1030-1033.
29. H. Nasef, V. Beni and C. K. O'Sullivan, *Anal. Method.*, 2010, **2**, 1461-1466.
30. K. Nakatani, S. Sando and I. Saito, *Nat Biotech*, 2001, **19**, 51-55.

31. A. J. Thiel, A. G. Frutos, C. E. Jordan, R. M. Corn and L. M. Smith, *Anal. Chem.*, 1997, **69**, 4948-4956.
32. F. Caruso, E. Rodda, D. N. Furlong, K. Niikura and Y. Okahata, *Anal. Chem.*, 1997, **69**, 2043-2049.
33. Y. Okahata, M. Kawase, K. Niikura, F. Ohtake, H. Furusawa and Y. Ebara, *Anal. Chem.*, 1998, **70**, 1288-1296.
34. U. Rant, K. Arinaga, S. Fujita, N. Yokoyama, G. Abstreiter and M. Tornow, *Nano Lett.*, 2004, **4**, 2441-2445.
35. U. Rant, K. Arinaga, S. Scherer, E. Pringsheim, S. Fujita, N. Yokoyama, M. Tornow and G. Abstreiter, *Proc. Nat Acad. Sci.*, 2007, **104**, 17364-17369.
36. G. Braun, S. J. Lee, M. Dante, T.-Q. Nguyen, M. Moskovits and N. Reich, *J. Am. Chem. Soc.*, 2007, **129**, 6378-6379.
37. Y. C. Cao, R. Jin and C. A. Mirkin, *Science*, 2002, **297**, 1536-1540.
38. M. Culha, D. Stokes, L. R. Allain and T. Vo-Dinh, *Anal. Chem.*, 2003, **75**, 6196-6201.
39. K. Faulds, R. P. Barbagallo, J. T. Keer, W. E. Smith and D. Graham, *Analyst*, 2004, **129**, 567-568.
40. R. J. Stokes, A. Macaskill, J. A. Dougan, P. G. Hargreaves, H. M. Stanford, W. E. Smith, K. Faulds and D. Graham, *Chem. Commun.*, 2007, 2811-2813.
41. R. J. Stokes, A. Macaskill, P. J. Lundahl, W. E. Smith, K. Faulds and D. Graham, *Small*, 2007, **3**, 1593-1601.
42. K. Faulds, W. E. Smith and D. Graham, *Anal. Chem.*, 2003, **76**, 412-417.
43. D. Graham, W. E. Smith, A. M. T. Linacre, C. H. Munro, N. D. Watson and P. C. White, *Anal. Chem.*, 1997, **69**, 4703-4707.
44. S. E. J. Bell and N. M. S. Sirimuthu, *J. Am. Chem. Soc.*, 2006, **128**, 15580-15581.
45. L. Fabris, M. Dante, G. Braun, S. J. Lee, N. O. Reich, M. Moskovits, T.-Q. Nguyen and G. C. Bazan, *J. Am. Chem. Soc.*, 2007, **129**, 6086-6087.
46. C. Fang, A. Agarwal, K. D. Buddharaju, N. M. Khalid, S. M. Salim, E. Widjaja, M. V. Garland, N. Balasubramanian and D.-L. Kwong, *Biosens. Bioelectron.*, 2008, **24**, 216-221.
47. N. R. Isola, D. L. Stokes and T. Vo-Dinh, *Anal. Chem.*, 1998, **70**, 1352-1356.
48. T. Vo-Dinh, L. R. Allain and D. L. Stokes, *J. Raman. Spec.*, 2002, **33**, 511-516.
49. T. Vo-Dinh, K. Houck and D. L. Stokes, *Anal. Chem.*, 1994, **66**, 3379-3383.
50. K. Faulds, L. Fruk, D. C. Robson, D. G. Thompson, A. Enright, W. Ewen Smith and D. Graham, *Faraday Discuss.*, 2006, **132**, 261-268.
51. K. Faulds, F. McKenzie, W. E. Smith and D. Graham, *Angew. Chem. Int. Ed.*, 2007, **46**, 1829-1831.
52. D. Graham, B. J. Mallinder, D. Whitcombe, N. D. Watson and W. E. Smith, *Anal. Chem.*, 2002, **74**, 1069-1074.
53. D. van Lierop, K. Faulds and D. Graham, *Anal. Chem.*, 2011, **83**, 5817 - 5821.
54. A. Barhoumi and N. J. Halas, *J. Am. Chem. Soc.*, 2010, **132**, 12792-12793.
55. A. Barhoumi, D. Zhang, F. Tam and N. J. Halas, *J. Am. Chem. Soc.*, 2008, **130**, 5523-5529.
56. S. Mahajan, J. Richardson, T. Brown and P. N. Bartlett, *J. Am. Chem. Soc.*, 2008, **130**, 15589-15601.
57. S. Mahajan, University of Southampton, Southampton, 2008, p. 194.
58. C. V. Raman and K. S. Krishnan, *Nature*, 1928, **121**, 501 - 502.

59. M. Fleischmann, P. J. Hendra and A. J. McQuillan, *Chem. Phys. Lett.*, 1974, **26**, 163-166.
60. D. L. Jeanmaire and R. P. Van Duyne, *J. Electroanal. Chem.*, 1977, **84**, 1-20.
61. M. G. Albrecht and J. A. Creighton, *J. Am. Chem. Soc.*, 1977, **99**, 5215-5217.
62. A. Campion, J. E. Ivanecky, C. M. Child and M. Foster, *J. Am. Chem. Soc.*, 1995, **117**, 11807-11808.
63. A. Campion and P. Kambhampati, *Chem. Soc. Rev.*, 1998, **27**, 241-250.
64. D. P. Fromm, A. Sundaramurthy, A. Kinkhabwala, P. J. Schuck, G. S. Kino and W. E. Moerner, *J. Chem. Phys.*, 2006, **124**, 061101-061104.
65. X. Hu, T. Wang, L. Wang and S. Dong, *J. Phys. Chem. C.*, 2007, **111**, 6962-6969.
66. K. Kneipp, H. Kniepp, I. Itzkan, R. R. Dasari and M. S. Feld, *J. Phys.: Condens. Matter*, 2002, **14**, 597 - 624.
67. S. Lal, N. K. Grady, J. Kundu, C. S. Levin, J. B. Lassiter and N. J. Halas, *Chem. Soc. Rev.*, 2008, **37**, 898-911.
68. A. G. Brolo, D. E. Irish and J. Lipkowski, *J. Phys. Chem. B.*, 1997, **101**, 3906-3909.
69. P. Gao, D. Gosztola, L.-W. H. Leung and M. J. Weaver, *J. Electroanal. Chem.*, 1987, **233**, 211-222.
70. S. Hayashi, *Surf. Sci.*, 1985, **158**, 229-237.
71. D. D. Tuschel, J. E. Pemberton and J. E. Cook, *Langmuir*, 1986, **2**, 380-388.
72. M. A. Bryant and J. E. Pemberton, *Langmuir*, 1990, **6**, 751-758.
73. Z.-Q. Tian, B. Ren and D.-Y. Wu, *J. Phys. Chem. B.*, 2002, **106**, 9463-9483.
74. M. J. Banholzer, J. E. Millstone, L. Qin and C. A. Mirkin, *Chem. Soc. Rev.*, 2008, **37**, 885-897.
75. M. R. Jones, K. D. Osberg, R. J. Macfarlane, M. R. Langille and C. A. Mirkin, *Chem. Rev.*, 2011, **111**, 3736-3827.
76. N. M. B. Perney, J. J. Baumberg, M. E. Zoorob, M. D. B. Charlton, S. Mahnkopf and C. M. Netti, *Opt. Express*, 2006, **14**, 847-857.
77. K. C. Grabar, R. G. Freeman, M. B. Hommer and M. J. Natan, *Anal. Chem.*, 1995, **67**, 735-743.
78. P. C. Lee and D. Meisel, *J. Phys. Chem.*, 1982, **86**, 3391-3395.
79. A. M. Schwartzberg, C. D. Grant, A. Wolcott, C. E. Talley, T. R. Huser, R. Bogomolni and J. Z. Zhang, *J. Phys. Chem. B.*, 2004, **108**, 19191-19197.
80. J. J. Mock, M. Barbic, D. R. Smith, D. A. Schultz and S. Schultz, *J. Chem. Phys.*, 2002, **116**, 6755-6759.
81. L. Nguyen Viet and et al., *Nanotechnology*, 2010, **21**, 035605.
82. N. Tian, Z.-Y. Zhou, S.-G. Sun, L. Cui, B. Ren and Z.-Q. Tian, *Chem. Commun.*, 2006, 4090-4092.
83. P. C. Wu, C. G. Khoury, T.-H. Kim, Y. Yang, M. Losurdo, G. V. Bianco, T. Vo-Dinh, A. S. Brown and H. O. Everitt, *J. Am. Chem. Soc.*, 2009, **131**, 12032-12033.
84. M. V. Yigit, L. Zhu, M. A. Ifediba, Y. Zhang, K. Carr, A. Moore and Z. Medarova, *ACS Nano*, 2010, **5**, 1056-1066.
85. C. L. Zavaleta, B. R. Smith, I. Walton, W. Doering, G. Davis, B. Shojaei, M. J. Natan and S. S. Gambhir, *Proc. Nat Acad. Sci.*, 2009, **106**, 13511-13516.
86. J. Kneipp, H. Kneipp, B. Wittig and K. Kneipp, *Nano Lett.*, 2007, **7**, 2819-2823.
87. S. Zong, Z. Wang, J. Yang and Y. Cui, *Anal. Chem.*, 2011, **83**, 4178-4183.

88. J. Kneipp, H. Kneipp, B. Wittig and K. Kneipp, *J. Phys. Chem. C.*, 2010, **114**, 7421-7426.
89. J. Aizpurua, P. Hanarp, D. S. Sutherland, auml, M. ll, G. W. Bryant, Garc, iacute and F. J. a de Abajo, *Phys. Rev. Lett.*, 2003, **90**, 057401.
90. C. L. Haynes and R. P. Van Duyne, *J. Phys. Chem. B.*, 2003, **107**, 7426-7433.
91. J. Xie, Q. Zhang, J. Y. Lee and D. I. C. Wang, *ACS Nano*, 2008, **2**, 2473-2480.
92. J. B. Jackson and N. J. Halas, *Proc. Nat. Acad. Sci.*, 2004, **101**, 17930-17935.
93. S. J. Oldenburg, R. D. Averitt, S. L. Westcott and N. J. Halas, *Chem. Phys. Lett.*, 1998, **288**, 243-247.
94. N. C. Linn, C. H. Sun, A. Arya, P. Jiang and B. Kiang, *Nanotechnology*, 2009, **20**, 225303.
95. A. J. Haes, S. Zou, G. C. Schatz and R. P. Van Duyne, *J. Phys. Chem. B.*, 2003, **108**, 109-116.
96. C. L. Haynes and R. P. Van Duyne, *J. Phys. Chem. B.*, 2001, **105**, 5599-5611.
97. J. C. Hulteen and R. P. V. Duyne, *J. Vac. Sci. Technol. A*, 1995, **13**, 1553-1558.
98. J. C. Hulteen, D. A. Treichel, M. T. Smith, M. L. Duval, T. R. Jensen and R. P. Van Duyne, *J. Phys. Chem. B.*, 1999, **103**, 3854-3863.
99. M. Litorja, C. L. Haynes, A. J. Haes, T. R. Jensen and R. P. Van Duyne, *J. Phys. Chem. B.*, 2001, **105**, 6907-6915.
100. S. Cintra, M. E. Abdelsalam, P. N. Bartlett, J. J. Baumberg, T. A. Kelf, Y. Sugawara and A. E. Russell, *Faraday Discuss.*, 2006, **132**, 191-199.
101. P. M. Tessier, O. D. Velev, A. T. Kalambur, J. F. Rabolt, A. M. Lenhoff and E. W. Kaler, *J. Am. Chem. Soc.*, 2000, **122**, 9554-9555.
102. D. M. Kuncicky, B. G. Prevo and O. D. Velev, *J. Mater. Chem.*, 2006, **16**, 1207-1211.
103. L. Lu and A. Eychmüller, *Acc. Chem. Res.*, 2008, **41**, 244-253.
104. P. N. Bartlett, J. J. Baumberg, S. Coyle and M. E. Abdelsalam, *Faraday Discuss.*, 2004, **125**, 117-132.
105. R. M. Cole, J. J. Baumberg, F. J. Garcia de Abajo, S. Mahajan, M. Abdelsalam and P. N. Bartlett, *Nano Lett.*, 2007, **7**, 2094-2100.
106. T. A. Kelf, Y. Sugawara, R. M. Cole, J. J. Baumberg, M. E. Abdelsalam, S. Cintra, S. Mahajan, A. E. Russell and P. N. Bartlett, *Phys. Rev. B.*, 2006, **74**, 245415.
107. S. Mahajan, R. M. Cole, B. F. Soares, S. H. Pelfrey, A. E. Russell, J. J. Baumberg and P. N. Bartlett, *J. Phys. Chem. C.*, 2009, **113**, 9284-9289.
108. S. Mahajan, M. Abdelsalam, Y. Suguwara, S. Cintra, A. Russell, J. Baumberg and P. Bartlett, *Phys. Chem. Chem. Phys.*, 2007, **9**, 104-109.
109. S. Mahajan, J. J. Baumberg, A. E. Russell and P. N. Bartlett, *Phys. Chem. Chem. Phys.*, 2007, **9**, 6016-6020.
110. M. Abdelsalam, P. N. Bartlett, A. E. Russell, J. J. Baumberg, E. J. Calvo, N. s. G. Tognalli and A. Fainstein, *Langmuir*, 2008, **24**, 7018-7023.
111. M. E. Abdelsalam, S. Mahajan, P. N. Bartlett, J. J. Baumberg and A. E. Russell, *J. Am. Chem. Soc.*, 2007, **129**, 7399-7406.
112. L. Cui, S. Mahajan, R. M. Cole, B. Soares, P. N. Bartlett, J. J. Baumberg, I. P. Hayward, B. Ren, A. E. Russell and Z. Q. Tian, *Phys. Chem. Chem. Phys.*, 2009, **11**, 1023-1026.
113. M. E. Abdelsalam, P. N. Bartlett, J. J. Baumberg, S. Cintra, T. A. Kelf and A. E. Russell, *Electrochem. Commun.*, 2005, **7**, 740-744.
114. S. Mahajan, PhD Thesis, University of Southampton, Southampton, 2008.

115. W. L. Barnes, A. Dereux and T. W. Ebbesen, *Nature*, 2003, **424**, 824-830.
116. P. Vukusic and J. R. Sambles, *Nature*, 2003, **424**, 852-855.
117. E. Prodan, C. Radloff, N. J. Halas and P. Nordlander, *Science*, 2003, **302**, 419-422.
118. H. Wang, D. W. Brandl, P. Nordlander and N. J. Halas, *Acc. Chem. Res.*, 2006, **40**, 53-62.
119. S. Mahajan, J. Richardson, N. B. Gaied, Z. Zhao, T. Brown and P. N. Bartlett, *Electroanalysis*, 2009, **21**, 2190-2197.
120. T. M. Herne and M. J. Tarlov, *J. Am. Chem. Soc.*, 1997, **119**, 8916-8920.
121. J. N. Murphy, A. K. H. Cheng, H.-Z. Yu and D. Bizzotto, *J. Am. Chem. Soc.*, 2009, **131**, 4042-4050.
122. D. Erts, B. Polyakov, H. Olin and E. Tuite, *J. Phys. Chem. B.*, 2003, **107**, 3591-3597.
123. C.-Y. Lee, P. Gong, G. M. Harbers, D. W. Grainger, D. G. Castner and L. J. Gamble, *Anal. Chem.*, 2006, **78**, 3316-3325.
124. P. Valenta and H. W. Nürnberg, *Eur. Biophys. J.*, 1974, **1**, 17-26.
125. E. Palecek, *Collect. Czech. Chem. Commun.*, 1974, **39**, 3449 - 3460.
126. V. Brabec and E. Palecek, *Biophys. Chem.*, 1976, **4**, 79-92.
127. E. Palecek, *Bioelectrochem. Bioenerg.*, 1992, **28**, 71-83.
128. R. G. Sosnowski, E. Tu, W. F. Butler, J. P. O'Connell and M. J. Heller, *Proc. Nat Acad. Sci.*, 1997, **94**, 1119-1123.
129. R. J. Heaton, A. W. Peterson and R. M. Georgiadis, *Proc. Nat Acad. Sci.*, 2001, **98**, 3701-3704.
130. A.-M. Spehar-Deleze, L. Schmidt, R. Neier, S. Kulmala, N. de Rooij and M. Koudelka-Hep, *Biosens. Bioelectron.*, 2006, **22**, 722-729.
131. F. Wei, B. Sun, W. Liao, J. Ouyang and X. Sheng Zhao, *Biosens. Bioelectron.*, 2003, **18**, 1149-1155.
132. M. Bartošík and E. Paleček, *Electroanalysis*, 2011, 1311 - 1319.
133. D. K. Corrigan, N. Gale, T. Brown and P. N. Bartlett, *Angew. Chem.*, 2010, **122**, 6053-6056.

2. Materials and Methods

The experimental procedures in this chapter are a general description of the methods used. Details of specific experimental conditions accompany the results in the relevant chapter of this thesis.

2.1. Materials

All aqueous solutions were prepared using deionised water (resistivity 18 MΩ cm) from a Purite select water purifying system. An extensive list of the chemicals and materials is provided alphabetically in Table 2.1.

Table 2.1. List of chemicals and materials used.

Chemical/Material	Purity	Supplier
Acridine orange	99.8 %	Sigma-Aldrich
Ammonium chloride	99.9 %	Sigma-Aldrich
Argon	99.988 %, Pureshield	Boc Gases
Brightener (E3)	-	Metalor Technologies
Caesium chloride	99.9 %	Sigma-Aldrich
4',6-diamidino-2-phenylindole	98 %	Invitrogen
Dimethylformamide	HPLC grade	Rathburn Chemicals
Dimethlysulfoxide	Glass distilled grade	Rathburn Chemicals
DRAQ 5™	-	Invitrogen
Ethanol	HPLC grade	Rathburn Chemicals
Gold Plating Solution (ECF 60)	-	Metalor Technologies
Gold wire	0.05 mm diameter, 99.995%	Alfa-Aeasar
Hoechst 33258	98 %	Invitrogen
Hydrochloric acid	Aristar grade	BDH (VWR)
Lithium chloride	99.9%	Sigma-Aldrich
Magnesium chloride	98 %	Sigma-Aldrich

Mercaptohexanol	97 %	Sigma-Aldrich
Mercury	99.9998 %	Alfa-Aesar
Mercury (I) chloride	99.5 %	Alfa-Aesar
Methylene Blue	99.8 %	Sigma-Aldrich
para-Mercaptobenzoic acid	90 %	Sigma-Aldrich
Potassium chloride	99.9 %	Sigma-Aldrich
Polystyrene colloidal spheres	1 % wt. Solutions	Duke Scientific
Platinum wire	99.995 %	Alfa-Aeasar
Sodium chloride	99.9 %	Sigma-Aldrich
Sodium hydroxide	99.99 %	Sigma-Aldrich
Sodium phosphate monobasic	≥ 98 %	Sigma-Aldrich
Sulfuric acid	Aristar grade	BDH (VWR)
To-Pro 3	-	Invitrogen
Trizma® Base	99.8 %	Sigma-Aldrich

2.2. Reference Electrodes

Home made saturated calomel electrodes (SCE) and silver/silver chloride electrodes (Ag/AgCl) were prepared in accordance with standard procedures[1], and stored in saturated potassium chloride solution when not in use.

2.3. Preparation of Sphere Segment Void Substrates

2.3.1. Assembly of Colloidal Templates

Sphere Segment Void (SSV) substrates were prepared from the electrodeposition of metal through a colloidal crystal template. The construction of colloidal crystal templates has been described extensively[2-5], and a wide variety of techniques can be used to prepare both mono and multi-layers of closely packed colloidal particles.

The method of template preparation described in this section is based on the convective assembly process studied extensively by Nagayama and co-workers[6-8], in which a monolayer of hexagonally close packed polystyrene spheres is assembled from a mono-disperse solution of colloidal particles during a controlled evaporation process (Figure 2.1). The capillary emersion forces that arise during the controlled evaporation of water from the colloidal particle solution drives the formation of the colloidal crystal template.

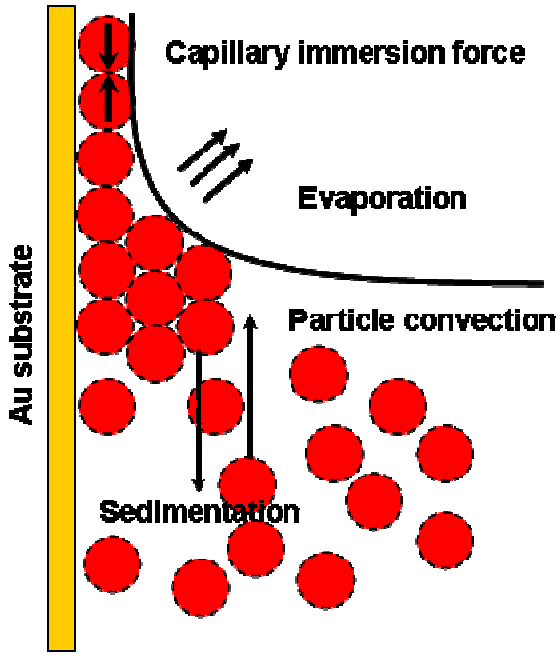

Figure 2.1. Illustration showing the self-assembly of colloidal spheres at a gold substrate. Controlled evaporation of water from the colloidal particle solution results in a capillary immersion force that attracts the particles towards each other, forming the colloidal crystal template.

A thin layer cell filled with colloidal particles and kept at a defined temperature and orientation was used to control the evaporation process. A standard gold-chrome coated microscope slide was prepared by thermal vapour deposition of approximately 200 nm gold (99.9 %, Agar) on to a standard microscope glass slide (76 mm x 26 mm, Menzel-Gläser). The gold-chrome coated microscope slide was carefully cut into eight sections (19 mm x 13 mm), and each was cleaned by sonication in ethanol (HPLC grade, Rathburn) for 2 h.

A thin layer cell (Figure 2.2) was then constructed from a glass cover slip (Menzel-Gläser, 24 x 24 mm, thickness 17 mm) and a section of the gold separated from the

gold surface by a Parafilm (Pechiney Plastic Inc.) spacer approximately 100 microns thick.

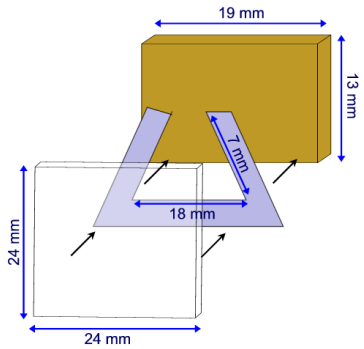

Figure 2.2. Schematic (not to scale) showing the preparation of a thin layer cell for the convective assembly of a monolayer colloidal crystal template. Typical dimensions are included. The three components are held together by gently melting the Parafilm allowing it to stick to both the gold and the cover slip.

A gap was left at the top of the thin layer cell to allow for filling of the colloidal sphere solution by capillary action. The template was then incubated at 13 °C and held at a 15 ° inclination for two days to allow controlled convective assembly of the colloidal template.

The templates used in this work were prepared from mono-disperse spheres of 600 nm diameter (size distribution 12.2 nm), but the methods described can be used to prepare large, well-ordered arrays for wide variety of sphere sizes ranging 200 to 1600 nm by altering the temperature and inclination angle during the evaporation process[9].

2.3.2. Electrodeposition

Electrodeposition was carried out using a conventional three-electrode system from a commercial gold plating solution (ECF 60, Metalor) containing 100 µL brightener (E3, Metalor) per 20 ml plating solution. During electrodeposition, the brightener acts as a catalyst, enhancing the nucleation of gold, preventing an uneven deposit and ensuring that the deposited metal is a true cast of the polystyrene template[10]. The colloidal template was used as the working electrode, with redundant areas insulated (using common clear nail varnish) to prevent conduction. A large area platinum gauze

was used as the counter-electrode and a homemade saturated calomel electrode (SCE) was used as the reference.

Gold was deposited from solution by applying a potentiostatic pulse at –0.72 V vs. SCE, and the volume of gold deposited monitored from the charge passed. A typical current-time transient is shown in Figure 2.3. After the initial nucleation and first few layer of the gold deposition, the shape of transient is dominated by the geometry of the template. As the film height increases, the area of exposed gold decreases and reaches a minimum when the deposition film height is equal to the radius of the spheres (0.5d). Further deposition beyond 0.5d results in an increase in the surface area and therefore the measured current again increases.

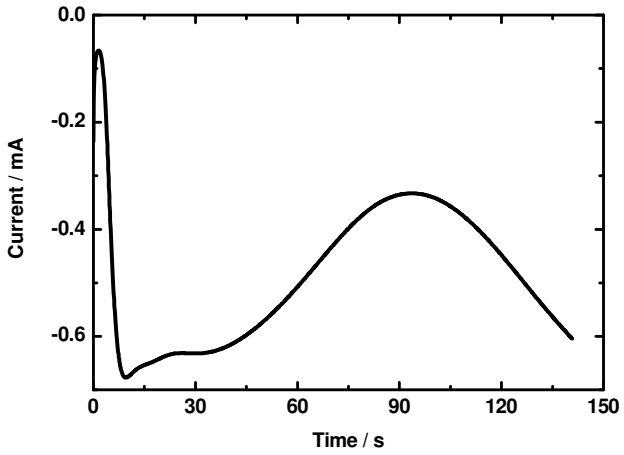

Figure 2.3. Current-time transient for the electrochemical deposition of gold through a 600 nm colloidal crystal template to 480 nm. The geometric area of the template was 0.3 cm^{-2}. A potential of -0.72 V *vs*. SCE was applied in a commercial gold plating bath (ECF 60/E3, Metalor Technologies).

After deposition the polystyrene spheres were removed by immersion in dimethylformamide (DMF) for thirty minutes, and the substrates were rinsed in deionised water before immediate use. The construction of sphere segment void substrates is summarised in Figure 2.4.

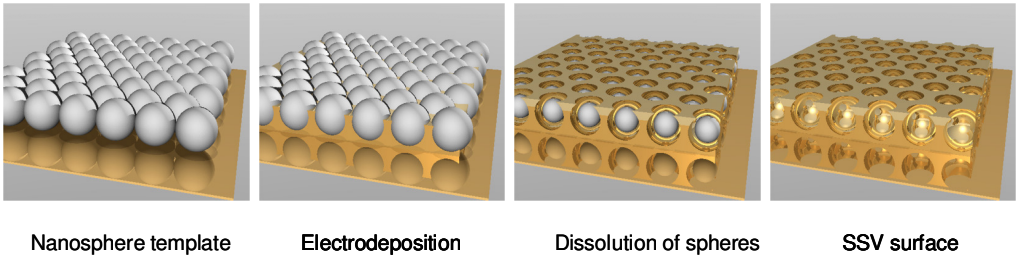

Figure 2.4. Summary of the method used to prepare sphere segment void substrates from a monolayer of polystyrene spheres on gold.

2.3.3. Characterisation

The structure and morphology of sphere segment void substrates were inspected in the first instance using a Philips XL30 environmental scanning electron microscope (ESEM) using a 30 kV accelerating voltage. High resolution images were acquired with a Jeol 6500F Field Emission Gun Scanning Electron Microscope (FEGSEM) with the electron beam energized at 15 kV. SEM images of varying resolutions for a typical sphere segment void substrate prepared from a 600 nm colloidal crystal template are shown in Figure 2.5. The deposition thickness was 480 nm.

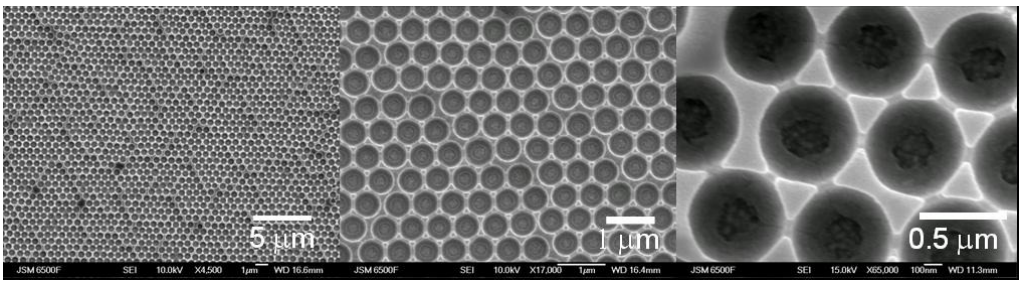

Figure 2.5. SEM micrographs of a 0.8d (d = 600 nm) gold sphere segment void substrate at varying resolutions.

2.4. Raman Spectroscopy

All Raman measurements were carried out using a Renishaw 2000 Raman spectrometer, equipped with a Renishaw 633 nm He-Ne laser and a Lecia DMLM series microscope. The maximum power output of the laser (as measured at the sample) was 2.7 mW, although typically lower powers were used during data

acquisition. The precise collection parameters used varied widely, and specific details are described where appropriate in the results chapters.

Scattered light was collected at the sample by employing a microscope objective with a ×50 magnification, which had either a short working distance (0.37 mm) or a long working distance (8 mm). The numerical apertures of the short and long working distance objectives were 0.75 and 0.55 respectively.

Prior to each use, the spectrometer grating was calibrated by measuring the position of the most prominent band from a silicon (111) wafer, which should be present at 520.6 cm^{-1}.

2.5. DNA Preparation

The oliogonucleotides described in this section were designed and synthesised by either James Richardson or Rachel Gao.

2.5.1. Synthesis

Standard DNA phosphoramidites, solid supports and additional reagents were purchased from Link Technologies, Sigma and Applied Biosystems. Synthesis columns were obtained from Link Technologies for 3'- C7-aminoalkyl oligonucleotides and the dithiol phosphoramidite was purchased from Glen Research. All oligonucleotides were synthesized on an Applied Biosystems 394 automated DNA/RNA synthesizer using a standard 0.2 or 1.0 μmole phosphoramidite cycles of acid-catalyzed detritylation, coupling, capping and iodine oxidation. Stepwise coupling efficiencies and overall yields were determined by the automated trityl cation conductivity monitoring facility and in all cases were >98.0%. All β-cyanoethyl phosphoramidite monomers were dissolved in anhydrous acetonitrile to a concentration of 0.1 M immediately prior to use. The coupling time for normal (A, G, C, T) monomers was 35 s and the coupling time for the dithiol monomers was extended to 600 s. Cleavage of oligonucleotides from the solid support and deprotection was achieved by exposure to concentrated aqueous ammonia for 60 min

at room temperature followed by heating in a sealed tube for 5 h at 55 °C. The 3'-Texas red-labelled oligonucleotides were synthesized by post-synthetic labeling of 3'-aminoalkyl oligonucleotides which were assembled using C7-aminolink solid support described above.

To incorporate the Texas Red chromophore at the 3'-end of C7-aminoalkyl oligonucleotide, 50-150 nmol of the oligonucleotide in 70 µL of 0.5 M Na_2CO_3/$NaHCO_3$ buffer (pH 8.75) was incubated overnight at room temperature with 625 µg of the succinimidyl ester of Texas Red (Invitrogen) in 40 µL of DMSO. The crude oligonucleotides were purified by reversed-phase HPLC and desalted by NAP-10 gel-filtration according to the manufacturer's instructions (GE Healthcare). Reversed-phase HPLC purification was carried out on a Gilson system using an Phenomenex column (C8), 10 mm x 250 mm, pore size 100 Å.

The following HPLC conditions were used: run time 20 min, flow rate 4 mL per min, binary system, gradient: time in min (% buffer B); 0 (0); 3 (0); 3.5 (15); 15 (60); 16 (100); 17 (100); 17.5 (0); 20 (0). Elution buffer A: 0.1 M ammonium acetate, pH 7.0, buffer B: 0.1 M ammonium acetate with 50% acetonitrile pH 7.0. Elution of oligonucleotides was monitored by ultraviolet absorption at 295 nm. Texas Red oligonucleotides gave two product peaks corresponding to the 5- and 6- regioisomers of Texas Red. The first peak (5-isomer) was collected and used in the subsequent SERS experiments and the second peak was discarded. After HPLC purification oligonucleotides were desalted using NAP-10 Sephadex columns (GE Healthcare), aliquoted into eppendorf tubes and stored at –20 ºC. All oligonucleotides were characterized by MALDI-TOF mass spectrometry and capillary electrophoresis.

2.5.2. Structures and Sequences

An exhaustive list of the DNA sequences used is provided in Table 2.2. Generally, thiol modifications were placed at 5' end of the 'probe' DNA strand whilst reporter molecules were placed at the 3' end of the complementary 'target' strand. Proximity of the label to the surface ensured the maximum possible SERS signal was obtained.

Table 2.2. List of DNA sequences and modifications used.

Code	5' Mod*	Sequence (5' – 3')	3' Mod
Res1561	HXHXHX	AGG AAA CAC CAA AGA TGA TAT T	/
Res1567	/	TCC TTT GTG GTT TCT ACT ATA A	Texas Red
Res0653	/	TCC TTT GTG GCT ACT ATA A	Texas Red
Res1528	/	TCC TTT GTG GTT TCT ACT ATA A	/
Res1568	/	TCC TTT GTG GTT TTT ACT ATA A	/
Res1569	/	TCC TTT GTG GCT ACT ATA A	/
A6894	HXHXHX	GCC TGT CAG ATA	/
A6895	/	TAT CTG ACA GGC T	Cy3
Res0587	HXHXHX	ATT TCA GTC AAG TC	/
Res0585	HXHXHX	ATT TCA GTC GAG TC	/
A5500	HXHXHX	ATC TCA GTC GAG TC	/
Res0586	HXHXHX	ATC TCG GTC GAG TC	/
Res0588	HXHXHX	ATC TCG GGC GAG TC	/
Res0591	Texas Red	GAC TTG ACT GAA AT	/
Res0589	Texas Red	GAC TCG ACT GAA AT	/
A5196	Texas Red	GAC TCG ACT GAG AT	/
Res0590	Texas Red	GAC TCG ACC GAG AT	/
Res0592	Texas Red	GAC TCG CCC GAG AT	/

Typically, the label chosen as the reporter molecule was a commonly used flurophore, since their SERS spectra and attachment chemistry are well documented. Choice of a label that has an adsorption (λ_{max}) overlap with the Raman excitation laser (633 nm) can also result in additional enhancement to the signal obtained, due to surface enhanced resonant Raman scattering (SERRS). Structures of the labels, and the linker used to synthetically attach them to the oligonucleotide are shown in Figure 2.6.

* HXHXHX represents a thiol anchor that has been specifically designed with hexaethyleneglycol spacer groups to provide a large molecular footprint (Figure 2.7).

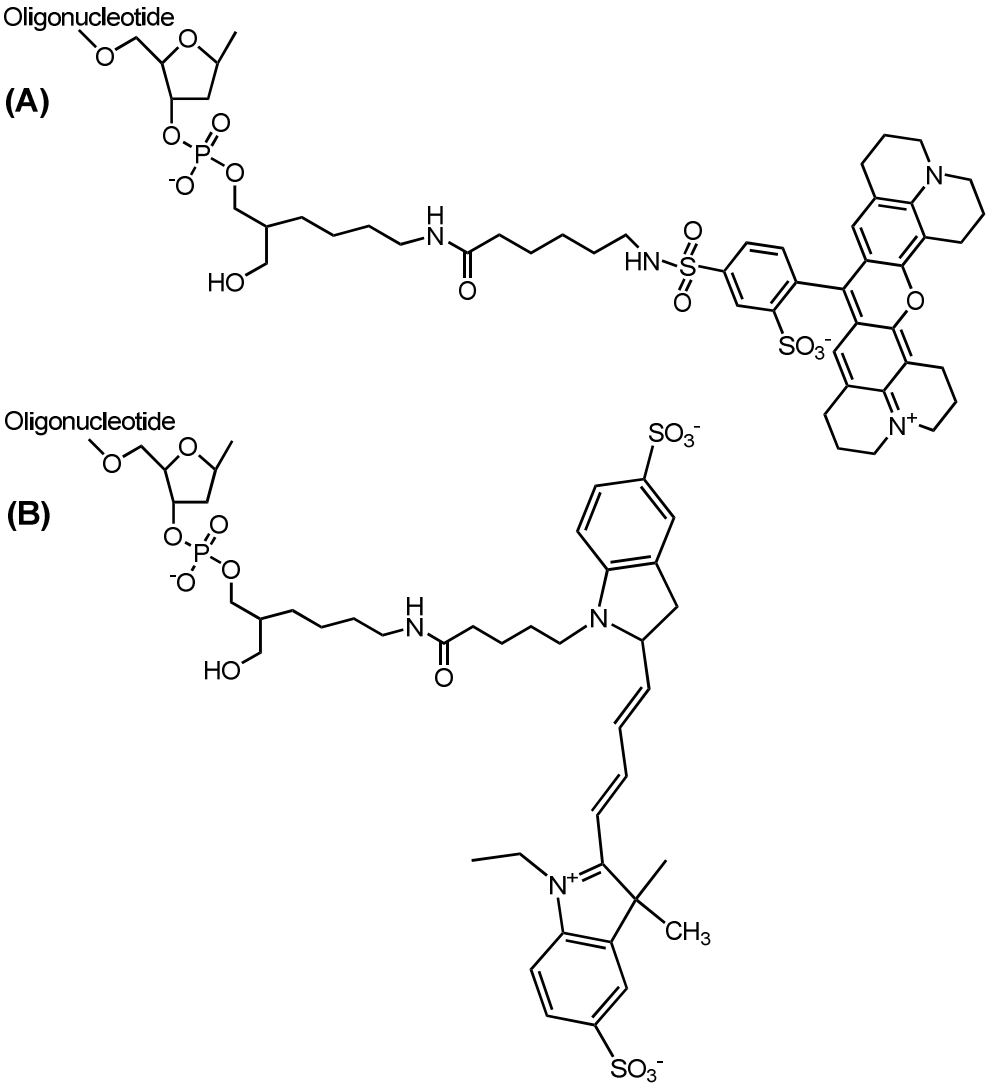

Figure 2.6. Chemical structures and attachment chemistry for the Raman labels (a) Texas Red, and (b) cy3®.

2.5.3. Immobilisation of DNA onto SSV Substrates

Thiol modified DNA samples were diluted to 1 μM in 10 mM Tris buffer solution (pH 7.2) containing 1 M NaCl. Sphere segment void (SSV) substrates were immersed into the 1 μM DNA solutions for 24 h at 4 °C, yielding an approximate surface coverage of 1.5×10^{12} molecules cm^{-2}.[9, 11]

The combination of a high salt concentration in the buffer and long immobilisation time ensures the maximum possible surface coverage. That is, the surface coverage is determined exclusively by the molecular footprint of the thiol anchor, minimising the

possibility of surface coverage variation between experiments. The thiol anchor has been specifically designed with hexaethyleneglycol spacer groups (Figure 2.7) that provide a large molecular footprint. This maximises the efficiency of hybridisation upon introduction of a target nucleic acid by preventing steric hindrance.

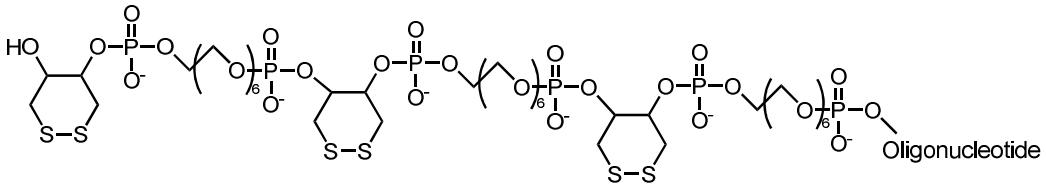

Figure 2.7. Chemical structure of the thiol anchor nucleotide modification. The three di-thiol groups ensure strong binding to the surface of the gold substrate, whilst the hexaethyleneglycol spacers ensure a large molecular footprint.

After immobilisation of the probe oligonucleotide, the remainder of the surface was passivated by soaking the SSV substrate into a 1 mM solution of mercapothexanol in 10 mM Tris buffer solution (pH 7.2) containing 1 M NaCl for 30 min. The mercaptohexanol forms a dense sub-layer that prevents non-specific binding[12, 13] and forces the bound DNA into an upright conformation[14, 15]. Substrates were rinsed thoroughly with a10 mM Tris buffer solution (pH 7.2) containing 1 M NaCl before being used in electrochemical experiments.

2.5.4. Surface Coverage Determination

The surface coverage of the immobilised oligonucleotides was determined by using the coloumetric method described by Steel and co-workers[16]. A three electrode system was used for the measurements, where the DNA covered SSV surface and a platinum gauze were used as the working and counter electrodes respectively. A saturated calomel electrode (SCE) was used as the reference.

A 500 ms pulse at -400 mV vs. SCE was applied from an initial potential of 100 mV in the presence and absence of ruthenium hexamine. The supporting electrolyte used was a 10 mM Tris (pH 7.2) buffer containing 10 mM NaCl which was purged with argon for 30 min and blanketed with argon thereafter.

The integrated charge Q at time t is given by the following expression:

$$Q = \frac{2nFAD_0^{\frac{1}{2}} c_0 t^{\frac{1}{2}}}{\pi^{\frac{1}{2}}} + Q_{dl} + nFA\Gamma_0 \qquad 2.1$$

Where t is the time, n is the number of electrons transferred, F is the Faraday constant, A is the area of the electrode, D_0 is diffusion coefficient of the electro-active species in solution and c_0 the bulk concentration of $[Ru(NH_3)_6]^{3+}$, Q_{dl} is the double layer charge, and Γ_0 is the surface coverage of bound $[Ru(NH_3)_6]^{3+}$.

Under conditions of saturation, that is, when the charge of the phosphate backbone is entirely compensated by the redox marker, the surface coverage of the DNA can be determined from the following expression:

$$\Gamma_{DNA} = \Gamma_0 (z/m) N_A \qquad 2.2$$

Where Γ_{DNA} is the surface coverage of the DNA, m is the number of phosphate residues, z is the charge of the redox molecule, and N_A is Avogadro's number.

2.6. PNA Preparation

Peptide nucleic acid sequences (PNA) were purchased from ATD Bio (Southampton), and used without further purification.

2.6.1. Structures and Sequences

The PNA sequences used are detailed in Table 2.3. In common with the design of DNA oligonuclotides, thiol modifications were placed at 3' end of the 'probe' DNA strand whilst reporter molecules were placed at the 5' end of the complementary 'target' strand, ensuring the maximum possible SERS signal was obtained. The thiol anchor modification used to ensure binding to the gold surface was identical to that used for DNA, shown in Figure 2.6.

Table 2.3. List of DNA sequences and modifications used.

Code	5' Mod	Sequence (5' – 3')	3' Mod
P264	HXHXHX	GCCTGTCAGATA	/
P265	/	TATCTGACAGGCT	Cy3

2.6.2. Immobilisation of PNA onto SSV Substrates

Purified PNA samples were diluted to 1 μM in a 50:50 co-solvent of DMSO and 10 mM Tris (pH 7.2), containing 1 M NaCl. Sphere segment void (SSV) substrates were immersed into the 1 μM DNA solutions for 24 h at 4 °C.

After immobilisation of the probe oligonucleotide, the remainder of the surface was passivated by soaking the SSV substrate into a 1 mM solution of mercapothexanol in 10 mM Tris buffer solution (pH 7.2) containing 1 M NaCl for 30 min. The mercapothexanol forms a dense sub-layer that prevents non-specific binding and forces the bound PNA strands into an upright conformation. Substrates were rinsed thoroughly with a 10 mM Tris buffer solution (pH 7.2) containing 1 M NaCl before being used in electrochemical experiments.

2.5.5. Surface Coverage Determination

The surface coverage of the immobilised PNA was determined using the same method as that described in section 2.5.2 for DNA. Although there are no phosphate groups on the PNA itself, the hexaethylene glycol linker that anchors the PNA to the gold surface is that same as that used for the DNA and contains three phosphate groups that can interact with the added ruthenium hexamine.

2.7. DNA and PNA Denaturation

2.7.1. Thermal Denaturation in Solution

Solution-based thermal denaturation was carried out on a Varian Cary 4000 UV-Visible spectrophotometer. 1 μM solutions (1 ml) of dsDNA or PNA/DNA duplexes were prepared in the desired buffer solution, and the temperature ramped at 1 °C per minute after an initial annealing step. Denaturation of duplex was measured from changes in UV adsorption spectrum at 260 nm.

2.7.2. Thermal and Electrochemical Melting at an SSV Surface

Both thermal and electrochemical melting at a sphere segment void substrate surface was carried out in a custom built spectro-electrochemical Raman cell designed by Ventacon ltd. (Figure 2.8). The cell was specifically designed for use with a Renishaw 2000 Raman microscope equipped with a standard Prior microscope stage. It utilises a horizontal geometry for viewing under the microscope. A thin 150 μl liquid film is maintained on the substrate. Thermal control is provided by a water jacket, whilst electrochemical control is provided by a three-electrode arrangement inside the cell, where the SERS substrate is used as the working electrode, and a platinum wire as the counter with a pseudo silver/silver chloride as the reference.

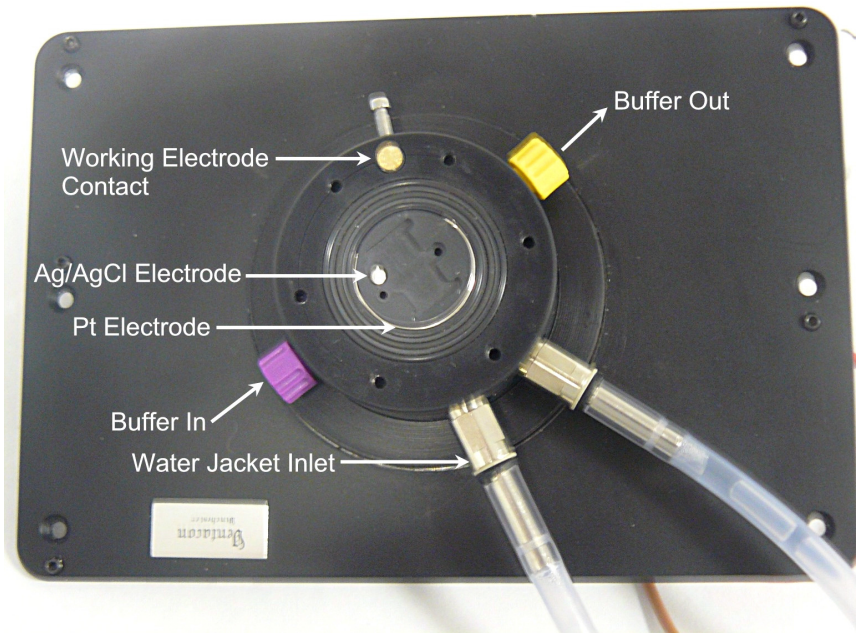

Figure 2.8. Photograph of the spectro-electrochemical cell designed for DNA detection and denaturation. The cell utilises a three-electrode system (with the SERS substrate as the working electrode) and a water jacket so that both the temperature and potential can be effectively controlled.

In a typical thermal melting experiment the temperature was ramped at 1 °C per minute by flowing water through the cell jacket via a computer controlled water bath (Grant). The temperature discrepancy between the water bath and the substrate surface was monitored by a thermocouple embedded into the cell.

In a typical electrochemical melting experiment the cell potential was swept at 0.05 mV s^{-1} or 0.1 mV s^{-1} from a starting potential of -0.3 V up to -1.6 V vs. Ag/AgCl. All electrochemical measurements were carried out using an EcoChemie μAutolabIII potentiostat/galvanostat at room temperature unless otherwise stated.

In both cases the nucleic acid denaturation was monitored from changes in the Raman spectra of a reporter molecule, which was either a label covalently attached to the target strand (such as Texas red) or a DNA binding agent (such as methylene Blue). A wide range of collection parameters were used for the acquisition of Raman data, and specific collection parameters accompany the relevant data in the results chapters.

2.8. References

1. P. N. Bartlett, *Biosensors: A Practical Approach*, Oxford University Press, Oxford, 1990.
2. H. Yang and P. Jiang, *Langmuir*, 2010, **26**, 13173-13182.
3. B. Jose, R. Steffen, U. Neugebauer, E. Sheridan, R. Marthi, R. J. Forster and T. E. Keyes, *Phys. Chem. Chem. Phys.*, 2009, **11**, 10923-10933.
4. V. L. Colvin, *MRS Bull.*, 2001, **26**, 637-641.
5. P. M. Tessier, O. D. Velev, A. T. Kalambur, J. F. Rabolt, A. M. Lenhoff and E. W. Kaler, *J. Am. Chem. Soc.*, 2000, **122**, 9554-9555.
6. N. Denkov, O. Velev, P. Kralchevski, I. Ivanov, H. Yoshimura and K. Nagayama, *Langmuir*, 1992, **8**, 3183-3190.
7. A. S. Dimitrov and K. Nagayama, *Langmuir*, 1996, **12**, 1303-1311.
8. K. Nagayama, *Colloid. Surface. A.*, 1996, **109**, 363-374.
9. S. Mahajan, PhD Thesis, University of Southampton, Southampton, 2008.
10. P. Wilkinson, *Gold Bull.*, 1986, **19**, 75 - 81.
11. S. Mahajan, J. Richardson, T. Brown and P. N. Bartlett, *J. Am. Chem. Soc.*, 2008, **130**, 15589-15601.
12. R. J. Heaton, A. W. Peterson and R. M. Georgiadis, *Proc. Nat Acad. Sci.*, 2001, **98**, 3701-3704.
13. T. M. Herne and M. J. Tarlov, *J. Am. Chem. Soc.*, 1997, **119**, 8916-8920.
14. D. Erts, B. Polyakov, H. Olin and E. Tuite, *J. Phys. Chem. B.*, 2003, **107**, 3591-3597.
15. C.-Y. Lee, P. Gong, G. M. Harbers, D. W. Grainger, D. G. Castner and L. J. Gamble, *Anal. Chem.*, 2006, **78**, 3316-3325.
16. A. B. Steel, T. M. Herne and M. J. Tarlov, *Anal. Chem.*, 1998, **70**, 4670-4677.

3. The Effect of Nucleic Acid Structure on Electrochemical Melting

3.1. Overview

The stability of a DNA duplex is determined by its structural composition. DNA duplexes are bound through a series of hydrogen bonds that link the constituent base pairs. In the case of an AT pair, there are two hydrogen bonds; and in the case of a GC pair, there are three hydrogen bonds. These hydrogen bonds can be broken to form two single strands of DNA when sufficient energy is provided, where the energy required is dependent on the base-pair composition. In addition to hydrogen bonding, base-pair stacking interactions are also important in determining duplex stability[1, 2]. The nitrogenous bases of DNA are flat and aromatic, and generally stack favourably on top of one another with overlapping π-bonds.

This first part of this chapter introduces the concept of DNA thermodynamics, and demonstrates how existing models for DNA stability can be used to predict the results for an electrochemical melting experiment based on the fundamental thermodynamic properties of a DNA duplex. The results presented are significant because they can be exploited in the future to design electrochemical melting assays with known melting potentials.

The second part of this chapter explores the electrochemical melting of duplexes that contain peptide nucleic acid (PNA); a DNA analogue with a neutral backbone that forms significantly stronger duplex structures[3]. It is demonstrated that PNA duplexes immobilised at an electrode surface can be denatured under an applied electric field, suggesting that a simple electrostatic repulsion mechanism for electrochemical melting can be ruled out.

3.2. DNA Thermodynamics

3.2.1. The Van't Hoff Equation

The stability of a DNA duplex is described mathematically by the Van't Hoff equation. The equation is the starting point for a derivation that describes the melting temperature of a duplex in terms of the fundamental thermodynamic properties and the total concentration of the duplex[1, 2].

Consider the hybridisation of two nucleic acid strands, A and B, which together form the DNA duplex AB. The equilibrium constant, *K*, for this system is:

$$K = \frac{[\mathrm{AB}]}{[\mathrm{A}][\mathrm{B}]} \qquad 3.1$$

The relationship between temperature, *T*, and the equilibrium constant is described thermodynamically by the Van't Hoff equation:

$$-\ln K = \frac{\Delta H}{RT} - \frac{\Delta S}{R} \qquad 3.2$$

Where R is the gas constant and ΔH and ΔS are the change in enthalpy and the change in entropy for the system respectively.

Rearranging the Van't Hoff equation, gives:

$$\frac{1}{T} = -\frac{R}{\Delta H}\ln K + \frac{\Delta S}{\Delta H} \qquad 3.3$$

Assuming no other nucleic acids are present the equilibrium constant can be re-written in terms of the extent of DNA hybridisation, α, and the total concentration, C_T:

$$\frac{1}{T} = -\frac{R}{\Delta H}\ln\left(\frac{2\alpha}{(1-\alpha)^2 C_T}\right) + \frac{\Delta S}{\Delta H} \qquad 3.4$$

where:

$$C_T = [\mathrm{A}] + [\mathrm{B}] + 2[\mathrm{AB}] \qquad 3.5$$

and, assuming [A] = [B], then:

$$\alpha = \frac{[\mathrm{AB}]}{[\mathrm{A}] + [\mathrm{AB}]} \qquad 3.6$$

The melting temperature, T_m, is described as the point at which half of the DNA strands present in the system will be in a single-stranded form and half will be in duplex form. Thus, at the melting temperature, the extent of DNA hybridisation will be α = ½:

$$\frac{1}{T_m} = \frac{R}{\Delta H} \ln\left(\frac{C_T}{4}\right) + \frac{\Delta S}{\Delta H} \qquad 3.7$$

3.2.2. Nearest Neighbour Models

The values used for the enthalpy and entropy change upon DNA denaturation are generally determined from nearest neighbour models, in which the DNA duplex is treated as a string of interactions between neighbouring base-pairs with an additional correction made for the base-pair solvent interaction at either end of the strand.

Thus, the enthalpy and entropy of duplex formation can be estimated by summing the individual thermodynamic parameters for neighbouring base-pair interactions. For example, the enthalpy of formation for the sequence AATGCA is calculated as follows:

$$\Delta H_{\mathrm{T}} = \mathrm{EA} + \mathrm{AA} + \mathrm{AT} + \mathrm{TG} + \mathrm{GC} + \mathrm{CA} + \mathrm{AE}$$

$$\Delta H_{\mathrm{T}} = 2.3 - 7.9 - 7.2 - 8.5 - 10.6 - 8.5 + 2.3 = -38.1 \text{ kcal mol}^{-1}$$

Typical entropy and enthalpy values for the different neighbouring base-pair interactions are given in Table 3.1[4].

Nearest-neighbour melting temperatures are calculated for and valid when the concentration of sodium chloride in the buffer is 1 M. An entropic correction is applied for calculating melting temperatures at lower salt concentrations[5, 6].

Table 3.1. Thermodynamic parameters for the possible combinations of base-pair stacks in a DNA duplex[4]. An additional entropic correction of -1.4 cal mol^{-1} K^{-1} must be made for a self-complementary strand.[4]

Base pair stack (5'- 3'/3'- 5')	ΔH / kcal mol^{-1}	ΔS / cal mol^{-1} K^{-1}
AA/TT	-7.9	-22.2
AT/TA	-7.2	-20.4
TA/AT	-7.2	-21.3
CA/GT	-8.5	-22.7
GT/CA	-8.4	-22.4
CT/GA	-7.8	-21.0
GA/CT	-8.2	-22.2
CG/GC	-10.6	-27.2
GC/CG	-9.8	-24.4
GG/CC	-8.0	-19.9
EG/EC* and EC/EG*	0.1	-2.8
ET/EA* and EA/ET*	2.3	4.1

*E is in initiation parameter that represents the interaction between the terminal base-pairs and the neighbouring solvent.

3.3. The Effect of dsDNA Structure on the Melting Potential

In a 'classic' DNA melting experiment, energy is provided by heating the duplex and monitoring the denaturation. The point at which half of the DNA strands are in the double stranded state, and half are in the single stranded state is the melting temperature, T_m. As demonstrated in Section 3.2., the melting temperature can be predicted for a duplex of known sequence by using nearest neighbour models and the Van't Hoff equation.

In an electrochemical melting experiment, the driving force behind denaturation is a change in potential at the electrode surface rather than temperature. The point at which half of the number of DNA strands at the surface in duplex form are denatured

during an electrochemical melting experiment is described as the melting potential, E_m. In order to design DNA probes with predictable electrochemical melting potentials for future assay applications, it is necessary to understand how the electrochemical melting potential is related to the thermal melting temperature. This will allow existing thermodynamic models to be used to predict DNA melting temperatures based on structure.

3.3.1. DNA Preparation and Design

Five 14-base long double stranded DNA (dsDNA) sequences (Table 3.2) were used in this investigation. Each dsDNA was composed of a 5' modified probe oligonucleotide and a corresponding complementary target oligonucleotide labelled on the 5' end with Texas Red. The probes were designed to bind to the gold substrates through three dithiol phosphoramidites and one hexaethyleneglycol (HEG) spacer attached to the probe oligonucleotide on 5' end. Each dithiol monomer can form two gold-sulphur bonds, ensuring that the probe oligonucleotide is strongly bound to the gold SSV surface.

dsDNA sequences 1 to 5 (Table 3.2) were designed to be sequentially more stable by replacing AT base pairs by GC base pairs. In principle, GC base pairs are more thermodynamically stable than AT base pairs because they have three hydrogen bonds in comparison to two hydrogen bonds for the AT base pair. The sequences were confirmed to be non self-complementary and the thermal melting temperatures were predicted using the publicly available "oligoanalyzer" application; published by Integrated DNA technologies® and available online at http://eu.idtdna.com/. This program uses the nearest neighbour method for predicting melting temperatures with an average error of ± 2 °C. In the nearest neighbour method, the binding enthalpy, ΔH_{total}, and binding entropy, ΔS_{total}, for the DNA duplex are calculated as the sum of tabulated values of ΔH and ΔS for each pair of neighbouring bases taken in sequence through the structure together with an initiation term that depends on whether the sequence starts with AT or GC. The melting temperature is then calculated from these ΔH_{total} and ΔS_{total} values taking into account the salt concentration.

Table 3.2 The different dsDNA samples used in this study. X is a disulfide (dithiol) monomer, H is a hexaethyleneglycol (HEG) spacer and TR is the Texas Red la. The GC base pair substitutions are highlighted in bold. Structures of the dithiol linker and label used are shown in Chapter 2.

dsDNA 1	5'XXXH	A	T	T	T	C	A	G	T	C	A	A	G	T	C	3'
	3'	T	A	A	A	G	T	C	A	G	T	T	C	A	G	TR5'
dsDNA 2	5'XXXH	A	T	T	T	C	A	G	T	C	**G**	A	G	T	C	3'
	3'	T	A	A	A	G	T	C	A	G	**C**	T	C	A	G	TR5'
dsDNA 3	5'XXXH	A	T	**C**	T	C	A	G	T	C	G	A	G	T	C	3'
	3'	T	A	**G**	A	G	T	C	A	G	C	T	C	A	G	TR5'
dsDNA 4	5'XXXH	A	T	C	T	C	**G**	G	T	C	G	A	G	T	C	3'
	3'	T	A	G	A	G	**C**	C	A	G	C	T	C	A	G	TR5'
dsDNA 5	5'XXXH	A	T	C	T	C	G	G	**G**	C	G	A	G	T	C	3'
	3'	T	A	G	A	G	C	C	**C**	G	C	T	C	A	G	TR5'

3.3.2. Solution Based-Thermal Melting

As expected, a linear relationship is observed between the calculated nearest-neighbour melting temperature and the experimentally determined value for the five strands (Table 3.3). The slightly higher experimental melting temperatures can be attributed to the synthetic modifications made to the oligonucleotides, where the addition of the Texas Red label is responsible for the increase in duplex stability[7]. Calculated melting temperatures are based on the stability of 1 μM of dsDNA in the presence of 0.1 M NaCl. Experimental melting temperatures were determined using UV-absorbance spectroscopy as described in Chapter 2, with 1 μM of oligonucleotide diluted in a 10 mM phosphate buffer (pH 8.1) containing 0.1 M NaCl.

Table 3.3. Melting temperatures and thermodynamic properties of the five dsDNA duplexes used in this study. Melting experiments were carried out in using UV-VIS spectroscopy in solution. The supporting buffer was 10mM phosphate (pH 8.1) containing 0.1 M NaCl and 1 μM dsDNA.

	Calculated T_m / ºC	**Experimental T_m / ºC**	**ΔH / kcal mol^{-1}**	**ΔS / cal mol^{-1} K^{-1}**
dsDNA 1	42	48.30 ± 0.19	-102.5	-283.9
dsDNA 2	45	51.96 ± 0.13	-104.9	-288.7
dsDNA 3	47	55.13 ± 0.25	-105.1	-287.5
dsDNA 4	51	58.09 ± 0.28	-107.4	-291.2
dsDNA 5	55	61.40 ± 0.15	-108.6	-290.9

3.3.3 Electrochemical Melting

Electrochemical melting (*E*-melting) experiments were performed using each of the five oliogonucleotides in order to determine the melting potential. In each experiment, after hybridisation with the target, the potential was ramped at 0.5 mV s^{-1} from a starting potential of –0.3 V to a final potential of –1.6 V *vs*. Ag/AgCl and SER spectra were recorded in 25 mV intervals.

Typical data from an *E*-melting experiment is shown in Figure 3.2. The bands at 1500 cm^{-1} and 1437 cm^{-1}, are characteristic of the Texas Red label which is pre-resonant

with the 633 nm laser used in these experiments (λ_{max} 590 nm). The Texas Red SERS signals initially rise as the potential becomes more negative before reaching a plateau at –0.875 V. This initial rise is reversible (Figure 3.1), and is attributed to a rearrangement of the Texas Red label and/or the dsDNA as a function of the applied potential[8, 9]. Reversible changes in the orientation of dsDNA at electrode surface of the type suggested here have been investigated by Rant et al. using fluorescent measurements[10, 11].

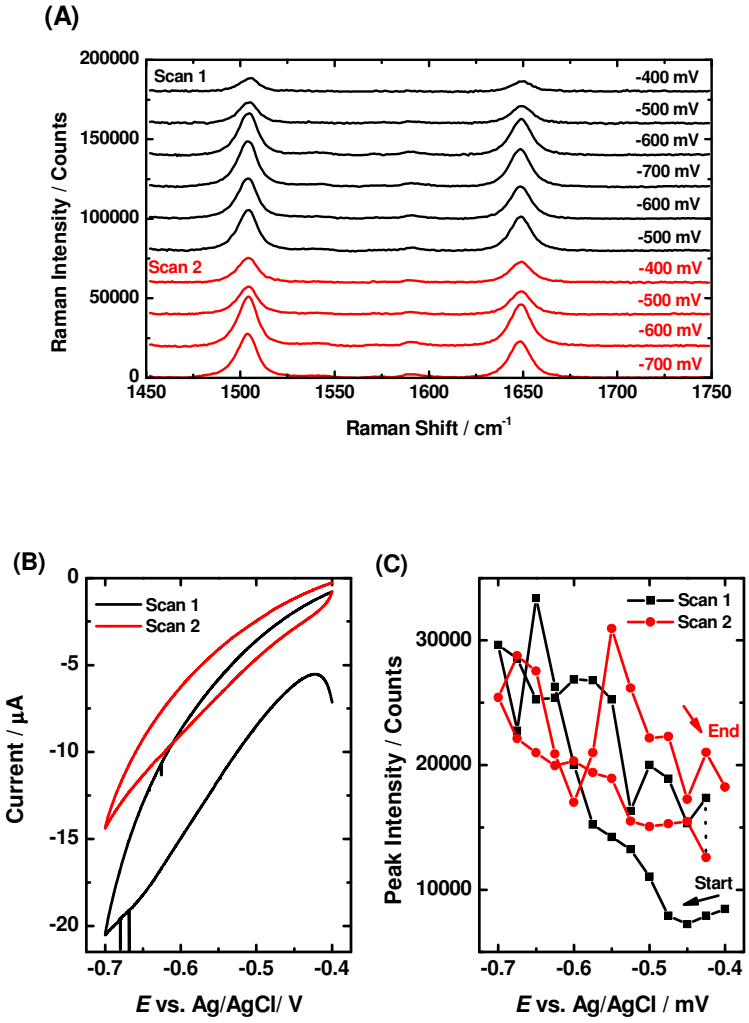

Figure 3.1. (A) Selected SERS spectra of surface immobilised dsDNA labelled with Texas red demonstrating the reversible changes in SERS signal as function of applied potential. (B) Recorded cyclic voltammograms and (C) background-corrected peak height for the 1500 cm^{-1} band as a function of applied potential. The potential was swept at 1 mV s^{-1} between -400 and -700 mV vs. Ag/AgCl in a 10 mM phosphate buffer (pH 8.1) containing 100 mM NaCl. SERS spectra were collected at 25 mV intervals in static mode using a 10 s acquisition.

On continuing to scan the potential cathodic beyond –0.975 V there is a rapid and irreversible decrease in the SERS signals for the Texas Red label (Figure 3.2.). This corresponds to denaturation of the dsDNA bound to the SSV surface and loss of the Texas Red labelled target strands to the bulk solution where they no longer contribute to the SERS signal. This corresponds to the *E*-melting process. Earlier work in our group has confirmed that the probe strand remains bound to the surface under these conditions so that the surface can be re-hybridised to target strands in solution and reused[8, 9].

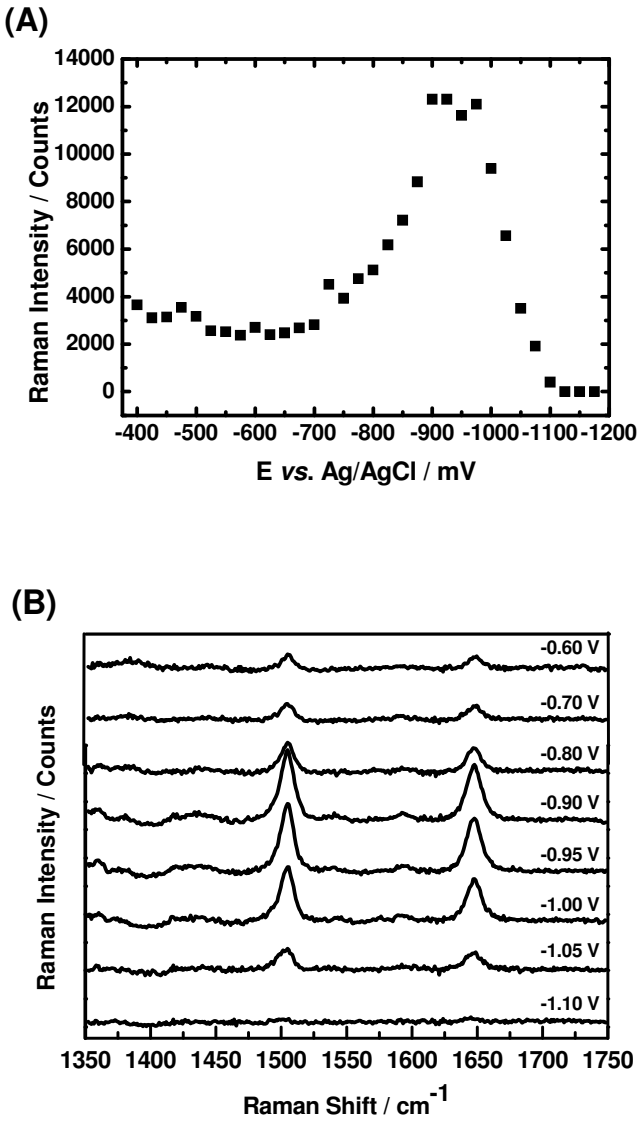

Figure 3.2. Data from dsDNA 3; representative of a typical *E*-melting experiment in which the potential was swept at 1 mV s^{-1} from an initial potential of -0.3 V in pH 8.1 10 mM phosphate buffer containing 0.1 M NaCl. (B) Representative spectra indicative of the change in peak height with applied potential. (B) The variation of the peak intensity at 1500 cm^{-1} as a function of applied potential. Spectra were acquired in static mode with a single 10 s acquisition.

The *E*-melting profiles for each of the five dsDNA strands are shown in Figure 3. A Boltzmann function was fitted to each profile and a plot of the first derivative used to define the melting potential. The sequential shift in the melting potential from dsDNA 1 through 5 is immediately apparent, and is characteristic of the increasing duplex stability.

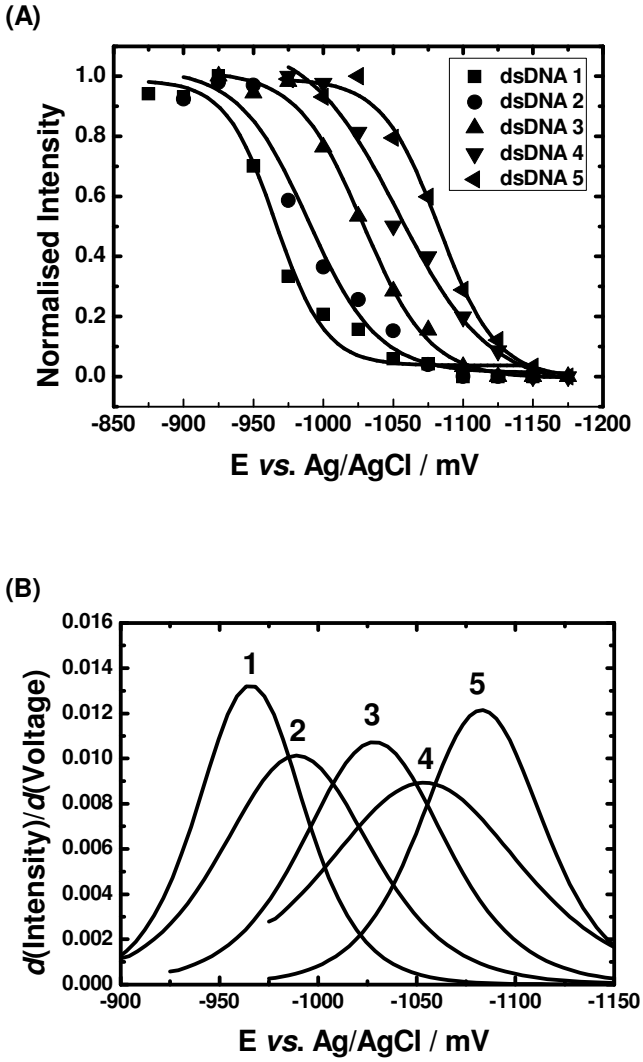

Figure 3.3. Discrimination of structural stability utilising *E*-melting. (A) The variation of the peak intensity at 1500 cm^{-1} as a function of applied potential for all five oligonuclotides. In each case the potential was swept at 1 mV s^{-1} from an initial potential of -0.3 V in pH 8.1 10 mM phosphate buffer containing 0.1 M NaCl. Spectra were acquired every 25 mV in static mode with a single 10 s acquisition. (B) First derivative plots indicative of melting potential based upon fitting a Boltzmann curve to the data set for each oligonucleotide.

The melting potentials for each of the five dsDNA strands are plotted against the corresponding calculated melting temperatures from the nearest neighbour model in Figure 3.4. The relationship clearly indicates a strong correlation between the melting temperature, T_m and the melting potential, E_m. When the stability of DNA duplex is increased by 1 °C (as measured by the experimental melting temperature), there is roughly a 9 mV shift in the melting potential.

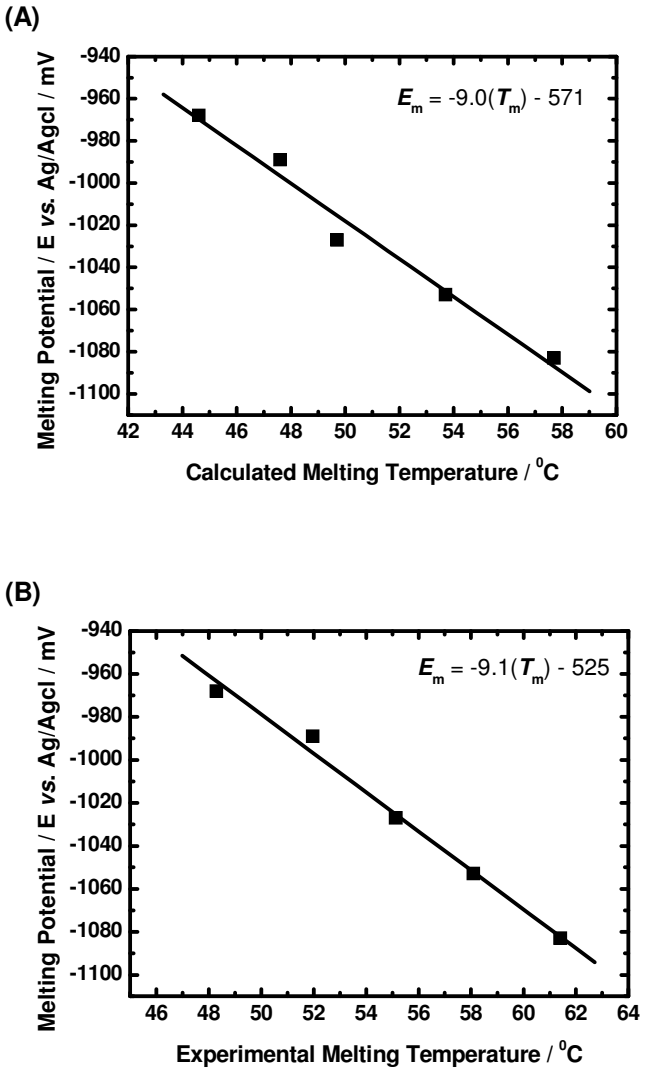

Figure 3.4. Relationship between melting potential and dsDNA stability. (A) The relationship between melting potential nearest neighbour model calculated melting temperature. (B) The relationship between melting potential and experimental melting temperature. A line of best fit has been fitted to the data in each case.

The lines of best fit shown for the data in Figure 3.4 were determined by a linear regression analysis. The relationship between the experimental melting temperature, T_m and the melting potential E_m is described mathematically by the following equation, which in the future, can be exploited to design nucleic acid probes for electrochemical melting assays that have known melting potentials:

$$\left(E_m / \mathrm{mV}\right) = -9.1\left(T_m / {}^{\circ}\mathrm{C}\right) - 525 \qquad 3.8.$$

Whilst it is difficult to draw any conclusions as to the mechanism of electrochemical melting based solely on these experiments, the results are nevertheless important because they demonstrate that the electrochemical melting potential is directly probing the structural composition of the DNA duplex. This result highlights the versatility of electrochemical melting as a tool for the study of dsDNA stability. However, caution should be advised when using Equation 3.8 to predict melting potentials based on dsDNA structure because in this study the strand length was kept constant at fourteen base-pairs. In later experiments, it was found that strand length also has an effect on the observed melting potential. This topic is discussed further in Chapter 4.

3.4. The Effect of Experimental Temperature on the Electrochemical Melting Potential

The experiments in this section were performed in collaboration with Pietro Marafini.

All of the electrochemical melting experiments described in Section 3.3 were performed at a room temperature of between 22 °C and 23 °C. Having discovered the melting potential changes by 9 mV when the melting temperature is changed by 1 °C, a series of experiments were designed to determine if the same relationship was observed during electrochemical melting at differing experimental temperatures. In order to minimise the effect of thermal denaturation the experimental temperature was kept well below the melting temperature. A refrigerated water bath (Grant) was used to control the temperature to an accuracy of ± 1 °C.

3.4.1. Electrochemical Cell Calibration

Introducing changes to the temperature at which an electrochemical melting experiment is performed requires that the temperature-dependent behaviour of the pseudo silver/silver chloride reference electrode used for the measurements is taken into account.

Whilst mathematical corrections are given in the literature for the temperature-dependent behaviour of saturated Ag/AgCl[12] and saturated calomel (SCE) reference electrodes[13, 14], there is no available data for the very specific environmental conditions that were used in the experiments described here, where the solid-phase silver chloride electrode is in contact with a buffer solution containing 10 mM phosphate buffer (pH 8.1) and 0.1 M NaCl.

A calibration experiment was performed in which the potential of the Ag/AgCl reference electrode was measured with respect to an SCE electrode as a function of temperature (Figure 3.5). Prior to measurement, the temperature of the SCE electrode was permitted to equilibrate with the system such that the temperatures of Ag/AgCl and SCE reference electrodes were the same. The measured potential *vs.* SCE was then converted to a temperature independent value against the standard hydrogen electrode using the following mathematical correction, reported by Bard and Faulkner[13]:

$$(E_{SHE}/\text{mV}) = 241.2 - 0.661(T/°\text{C}) - 1.75\times10^{-3}(T/°\text{C})^2 - 9.0\times10^{-7}(T/°\text{C})^3 \qquad 3.8$$

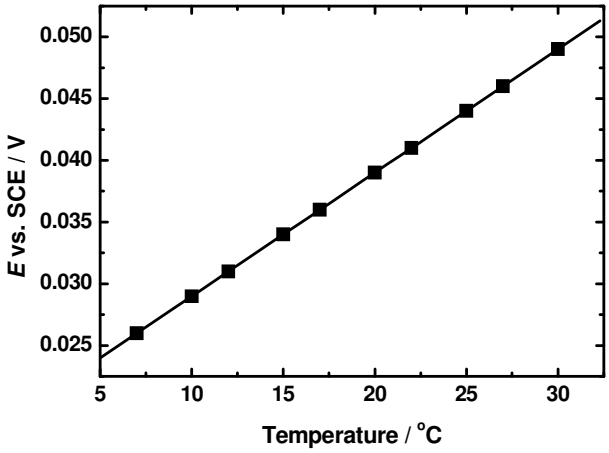

Figure 3.5. The change in the reference potential of a pseudo Ag/AgCl reference electrode (0.1 M NaCl; 0.01 M phosphate (pH 8.1) vs. SCE as a function of temperature.

3.4.2. Effect of Experimental Temperature on Melting Potential

Electrochemical melting experiments were performed at 10, 15, 20, 25 and 30 °C. In each case all of the other experimental parameters (sweep rate, Raman acquisition times) were kept the same. The cell was permitted to equilibrate for 30 minutes at the set temperature prior to the beginning of the potential sweep. The sequence of the probe DNA used in this experiment was AGGAAACACCAAAGATGATATT with a thiol anchor modification at the 5' as described in Chapter 2. The target sequence was perfectly complementary, and included a 3' Texas Red modification. Attenuation of

the Texas Red bands at 1500 cm^{-1} and 1650 cm^{-1} were used to monitor electrochemically driven denaturation.

Very little change in the melting potential was observed between 15 and 30 °C, whilst a large change in melting potential when the electrochemical melting was performed at 10 °C (Figure 3.6). In addition to the drop in the measured melting potential, the melting profile at 10 °C is also significantly sharper than those recorded at the other experimental temperatures, which are all very similar in profile.

In thermal melting experiments carried out in solution, an increase in sharpness of the melting profile generally indicates an increase in melting homogeneity; that is, the strand disassociates in a single step rather than as a series of steps. When DNA melts, it usually melts from the ends and in longer strands from 'weak' points along the duplex where base-pairs disassociate easily. If, for example, the ends of a DNA duplex are modified with end-capping monomers[15], the DNA melts more cooperatively leading to a sharper melting profile. The sharper electrochemical melting profile observed at 10 °C suggests that lowering the experimental temperature can cause the same effect, increasing duplex stability by inhibiting the thermal motions that lead to fraying at the ends of dsDNA structure.

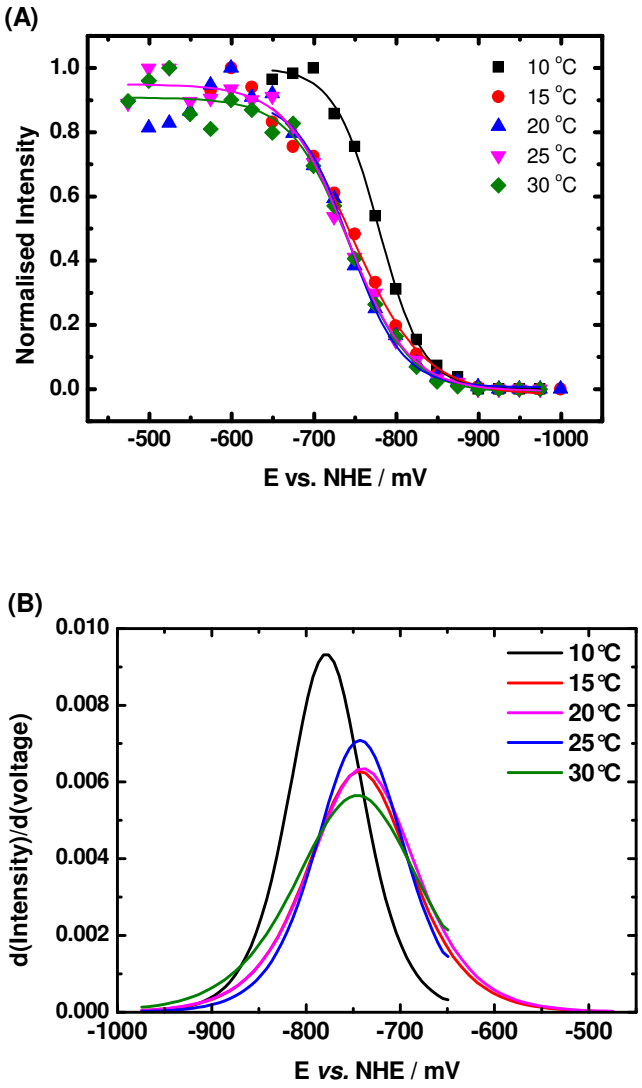

Figure 3.6. (A) Melting profiles and (B) first derivative plots illustrating the effect of experimental temperature on the melting potential. In each case the potential was swept at 1 mV s^{-1} from an initial potential of -0.3 V in pH 8.1 10 mM phosphate buffer containing 0.1 M NaCl. Spectra were acquired every 25 mV in static mode with a single 10 s acquisition.

The overall change in the melting potential as a function of experimental temperature is shown in Figure 3.7, and follows an exponential curve. The following expression can be used to predict electrochemical melting potential as a function of experimental temperature:

$$\left(E_{\mathrm{m}}\ vs.\ \mathrm{NHE}\,/\,\mathrm{mV}\right) = -1204\exp\left(\frac{-\left(T/^{\circ}\mathrm{C}\right)}{2.97}\right) - 707 \qquad 3.9.$$

This formula can be used in conjunction with that which was presented in Section 3.3 to predict the melting potential of a short dsDNA duplex as a function of both experimental temperature and structure. Whilst the lack of change in melting potential over the range 15 to 30 °C was surprising, it is also advantageous from the view-point of utilising electrochemical melting in a point-of-care device. Since there is very little variation in melting potential with temperature, it would be unnecessary to carry out experiments in a rigorously temperature controlled environment. Experiments performed over ambient temperatures (20 – 30 °C) would give near-identical values for the melting potential.

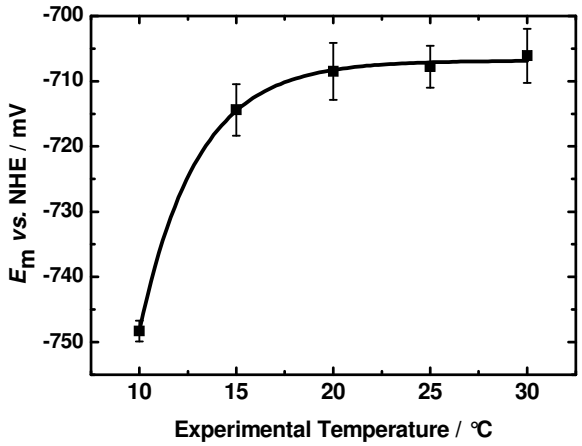

Figure 3.7. Effect of experimental temperature on the melting potential. The data has been fitted to an exponential function. For each experiment the potential was swept at 1 mV s^{-1} from an initial potential of -0.3 V in pH 8.1 10 mM phosphate buffer containing 0.1 M NaCl. Spectra were acquired every 25 mV in static mode with a single 10 s acquisition.

3.5. Electrochemical Melting of Peptide Nucleic Acid

3.5.1. Overview

Peptide nucleic acid (PNA) is an artificial DNA 'mimic' first synthesised by Peter Nielsen and co-workers at the University of Copenhagen in 1991[16]. Instead of a sugar-phosphate backbone, nucleobases are linked by peptide bonds (Figure 3.8). PNA/PNA and PNA/DNA duplexes are significantly more stable than DNA/DNA duplexes because of the reduction in electrostatic repulsion between the complementary nucleotides[3, 17]. For this reason, PNA has found a number of niche applications in molecular biology where there is a need to design probes that bind strongly to a complementary DNA target whilst keeping the probe as short as possible[18, 19]. PNA has also attracted interest for *in vivo* applications because it is not attacked by enzymes such as proteases in the body[20-22].

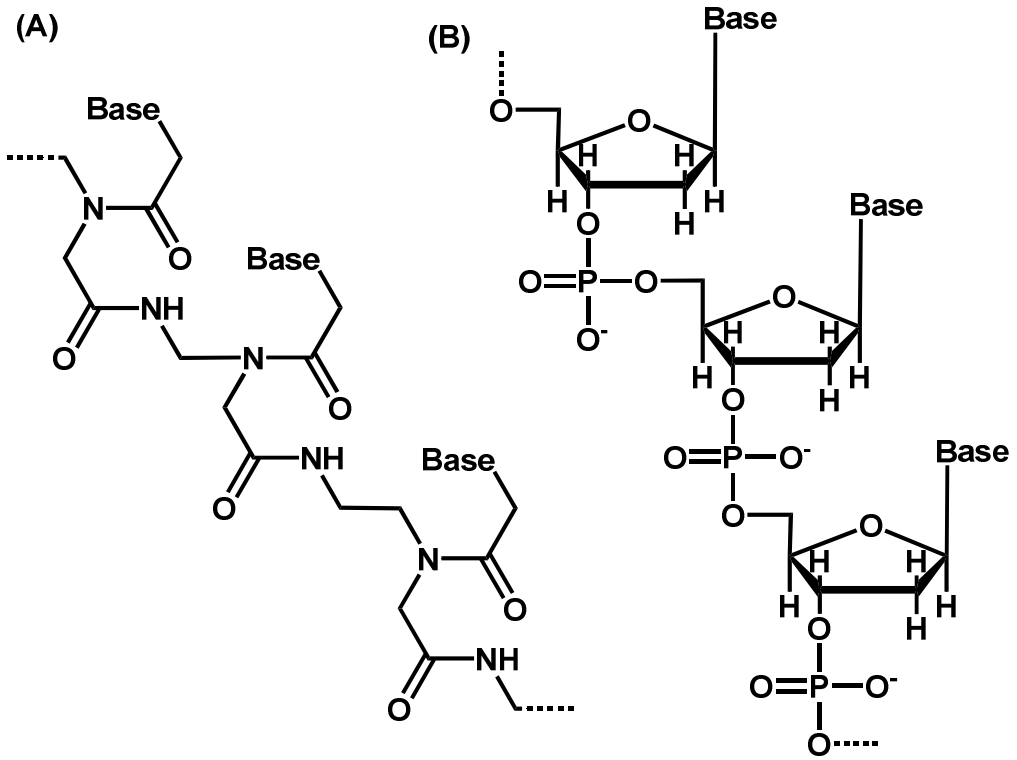

Figure 3.8. The backbone structure of (A) PNA and (B) DNA. The lack of charge on the backbone of PNA reduces electrostatic repulsion in the duplex structure.

The reasons for studying the use of PNA in an electrochemical melting experiment are three-fold. Firstly, PNA/DNA chimera are significantly more stable than DNA/DNA duplexes of the same sequence, and therefore defects in structure such as base-pair mismatches are more easily detected relative to the perfectly complementary[3, 17]. Secondly, an immobilised PNA probe strand is likely to be significantly more stable than a DNA probe strand under an applied potential because there will be no repulsion between the neutral backbone of the PNA and the electrode surface. Rant *et al.* have demonstrated previously that repulsion between the sugar-phosphate backbone of thiol-anchored ssDNA and the electrode surface makes a significant contribution to reductive desorption of the DNA[23].

Lastly, utilisation of PNA targets permits a possible mechanism for electrochemical melting to be tested. If the melting process is purely electrostatic repulsion between the target strand and the negatively-charged electrode surface, then PNA targets, which hold no formal charge, should remain stable under an applied electrode potential.

3.5.2. Oligonucleotide Design and Probe Immobilisation

In total, four oligonucleotides were synthesised, such that it was possible to produce all four possible combinations of probe and target strands at the electrode surface (Figure 3.9.).

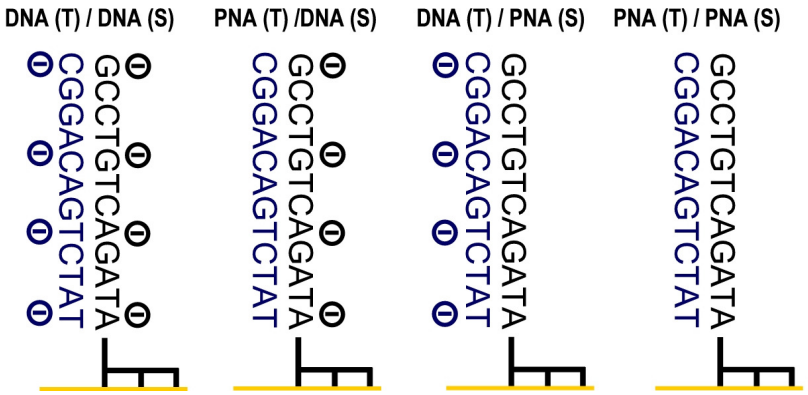

Figure 3.9. Sequences of the four oligonucleotides synthesised, in each case the target strand was modified with a 3' Cy3 group (proximal to the surface) (not shown). (S) Indicates the immobilised surface strand, and (T) the target strand.

During design, particular consideration was given to the GC content, because high GC content significantly decreases the solubility of PNA strands in aqueous media. However, it was still necessary to add dimethyl sufoxide (DMSO) to the PNA-containing immobilisation and hybridisation buffers due to the decrease in solubility caused by the addition of the thiol-anchor and label modifications to the PNA. Typically, immobilisation and hybridisation buffers for PNA contained 10% DMSO by volume. Whilst DNA containing buffers consisting of just salt and water were found to be stable and reusable for months, buffers that had added DMSO became unstable within one week as the co-solvent became immiscible over an extended period of time.

The probes were designed to bind to the gold substrates through three dithiol groups attached to the probe oligonucleotide on the 5' end. The target strands were all labelled with Cy3 at the 3' end, such that the label was proximal to the surface. This maximises the SERS signal because the intensity of the signal attenuates as a function of distance from the surface[24, 25]. Structures of the oligonucleotide modifications are shown in Chapter 2.

3.5.3. Surface Coverage Determination

The surface density of single-stranded DNA and single-stranded PNA probes on a gold electrode were determined using the method published by Steel and co-workers[26]. Reductive pulses were applied to a gold disk electrode (r = 0.5 mm) with surface-immobilised DNA or PNA, in the presence and absence of the redox probe ruthenium (III) hexamine. Ruthenium (III) hexamine displaces NaCl bound to DNA, and, under conditions of saturation, can be used to deduce the probe surface density (Figure 3.10). Full experimental details and calculations are described in Chapter 2.

Approximately 150 μM of ruthenium hexamine was required to saturate the 16 phosphate groups (13 on the DNA backbone, 3 on the thiol anchor) present on the surface immobilised DNA. A significantly lower concentration ruthenium hexamine (25 μM) was required to saturate the PNA probes. This was anticipated because in

contrast to DNA, the immobilised PNA probe molecules have only three phosphate groups, which are present on the thiol anchor.

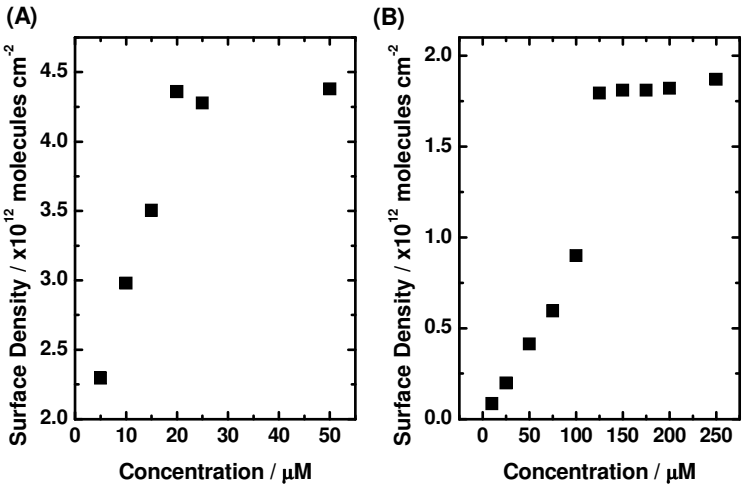

Figure 3.10. Absorption isotherms illustrating the concentration of ruthenium hexamine required for complete saturation of the phosphate groups present on surface-immobilised (A) PNA and (B) DNA. Note that whilst PNA itself does not contain any phosphate, the thiol anchor utilised to attach PNA to the gold surface contains three phosphate groups which bind ruthenium (III) hexamine. Concentrations were calculated from coulometric curves that were recorded by stepping the potential of a gold disc electrode (r = 0.5 mm) from 0.1 to -0.4 V vs. SCE. The electrolyte used was a 10 mM Tris buffer (pH 7.2) containing 10 mM NaCl.

The coulometric curves obtained under conditions of saturation were utilised to determine the surface density (Figure 3.11). The surface coverage of immobilised ssDNA was found to be 1.8×10^{12} molecules cm^{-2}, which is consistent with previous results obtained using the same immobilisation protocols and probes with the same thiol anchor group. The surface coverage of immobilised ssPNA was found to be 4.4×10^{12} molecules cm^{-2}, approximately double that for ssDNA. It is probable that the lack of charge on the backbone of PNA means that adsorbing strands do not repel one another as they adsorb on the surface, resulting in a higher surface density.

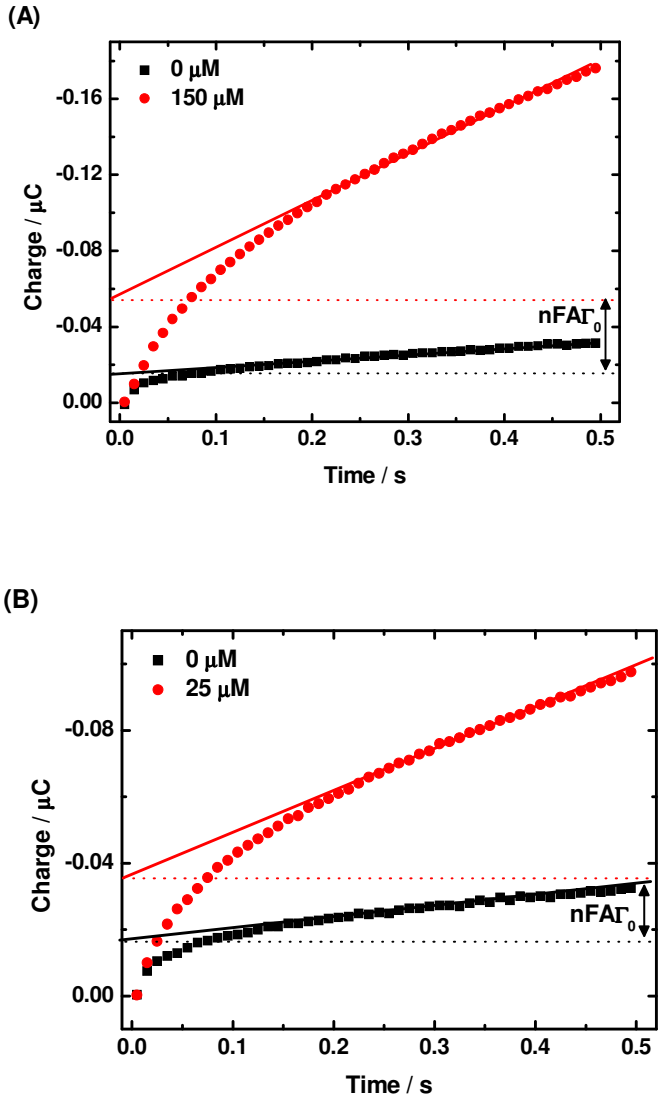

Figure 3.11. Determination of the surface density of (A) DNA and (B) PNA probes by utilising ruthenium (III) hexamine bound to phosphate groups. Note that whilst PNA itself does not contain any phosphate, the thiol anchor utilised to attach PNA to the gold surface contains three phosphate groups which bind ruthenium (III) hexamine. Coulometric curves were recorded by stepping the potential of a gold disc electrode (r = 0.5 mm) from 0.1 to -0.4 V vs. SCE. The electrolyte used was a 10 mM Tris buffer (pH 7.2) containing 10 mM NaCl.

3.5.4. Thermal Melting of PNA in Solution

Prior to performing electrochemical melting studies, the melting temperatures of three of the four probe/target combinations were measured in solution with UV-VIS spectrometry (Figure 3.12.). The absorbance at 260 nm of a solution containing 1 µM

of dsDNA in a 10mM phosphate buffer (pH 8.1) containing 0.1 M NaCl was monitored as a function of temperature. The absorbance in this region increases as the duplexes denature because in single-stranded form nucleic acid bases adsorb more light. The PNA/PNA duplex was too stable to measure using the available instrumentation, having a melting temperature greater than 80 °C.

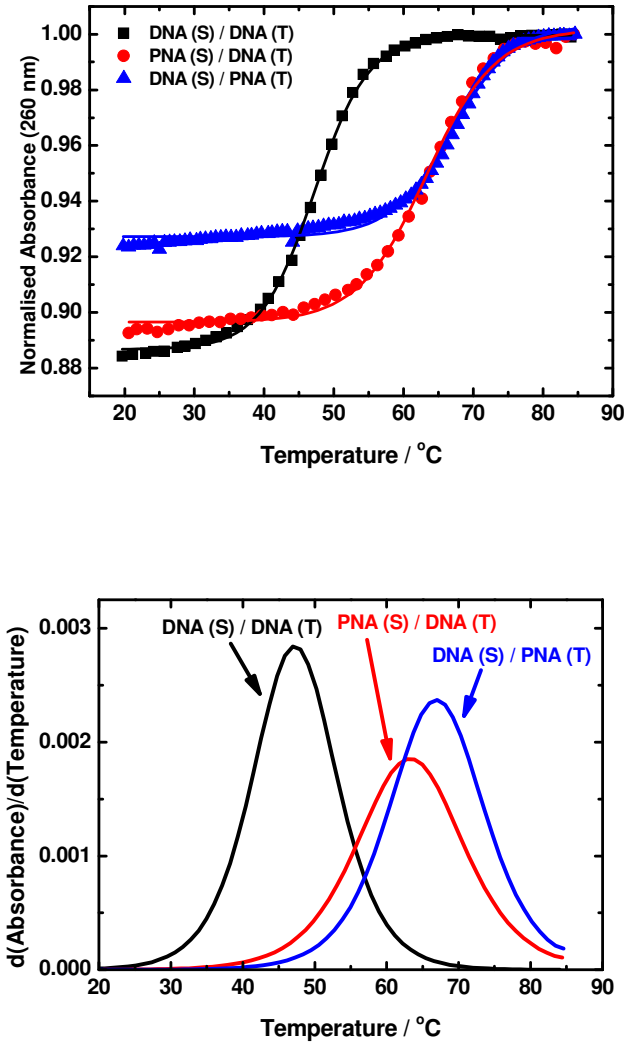

Figure 3.12. (A) The change in absorbance at 260 nm and (B) first derivative plots indicative of the thermal stability of DNA and PNA containing duplexes. The temperature of 10mM phosphate buffer (pH 8.1, 100 mM NaCl) containing 1 μM of dsDNA or PNA/DNA hybrids was ramped at 1 °C min^{-1} after an initial annealing step.

As expected, the PNA containing duplexes are significantly more (approximately 30 °C) stable than the duplex containing only DNA. However, it was also found that the stability of PNA containing duplexes differ depending on whether the labelled-target strands were constructed from PNA or from DNA.

When the target strand is constructed from PNA, the duplex is approximately 4 °C more stable. One possible explanation for the observed higher melting temperature is a stabilising effect from the Cy3 label when attached to PNA. The lack of charge on the PNA backbone may make it easier for the label to interact with the minor groove of the duplex and cause an increase in stability.

Comparison of the SERS spectra of immobilised PNA containing duplexes appears to support this explanation because there are differences in the spectra that are dependent on whether the label is attached to PNA or DNA (Figure 3.13.). The bands that appear at 1197 cm^{-1} and 1468 cm^{-1} when the label attached to DNA are red-shifted to 1219 cm^{-1} and 1487 cm^{-1} respectively when the label is attached to PNA. These bands are typically assigned to an aromatic CH in-plane bend and a CH asymmetric deformation respectively[27-29].

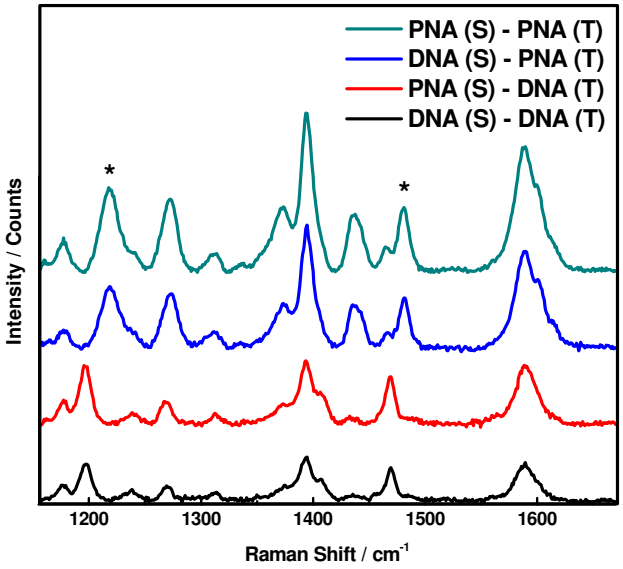

Figure 3.13. Spectra of the four possible probe-target combinations of DNA and PNA at an SSV surface. The bands marked (*) when the label is attached to PNA appear at lower wavenumbers when the label is attached to DNA. Spectra were acquired in static mode with a single 30 s acquisition.

3.5.5. Electrochemical Melting of PNA Containing Duplexes

Electrochemical melting (*E*-melting) experiments were performed using each of the four possible oligonucleotides combinations. In each experiment, after hybridisation with the target, the potential was ramped at 0.5 mV s^{-1} from a starting potential of –0.3 V to a final potential of –1.6 V *vs*. Ag/AgCl and SER spectra were recorded at 25 mV intervals.

Unlike the Texas Red labelled oligonucleotides presented in previous sections, no initial rise in intensity was observed upon driving the potential cathodic for Cy3 labelled oligonucleotides. Instead, a decrease in signal is observed before a plateau is reached, which suggests that label re-orientates in a position away from the surface as the potential is driven cathodic.

Prior to measurement, it was expected to be impossible to denature those duplexes which contained a non-anchored PNA strand because an electrostatic repulsion between the electrode surface and the sugar-phosphate backbone of the target was postulated as the mechanism of electrochemically induced denaturation However, electrochemical denaturation of an all-PNA duplex proved easily possible at moderately cathodic potentials (Figure 3.14). Denaturation of the PNA/PNA duplex was monitored through attenuation of the band at 1593 cm^{-1}, attributed to the C=N chromophore stretch.

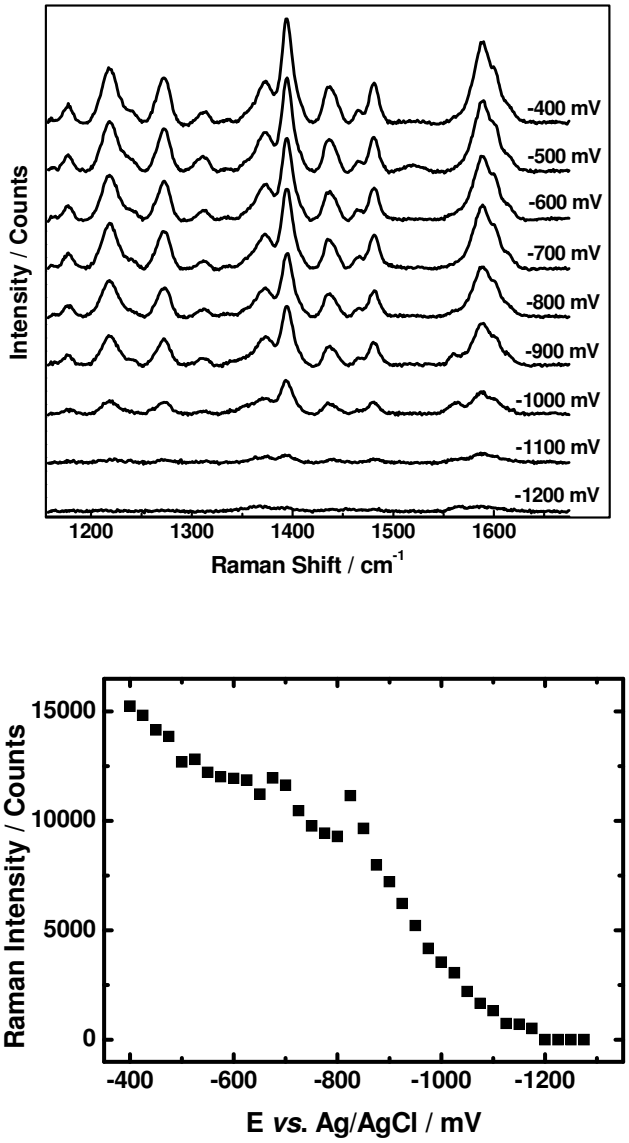

Figure 3.14. Data from the PNA/PNA duplex, which is representative of a typical E-melting experiment in which Cy3 is utilised as the reporter label. The potential was swept at 0.5 mV s^{-1} from an initial potential of -0.3 V in pH 8.1 10 mM phosphate buffer containing 0.1 M NaCl. (A) Representative spectra indicative of the change in peak height with applied potential. (B) The variation of the peak intensity at 1593 cm^{-1} as a function of applied potential. Spectra were acquired in static mode with a single 30 s acquisition.

Further electrochemical melting experiments were performed with the other three possible combinations of probe and target. It was possible to denature a surface immobilised duplex regardless of whether the target oligonucleotide was constructed

from DNA or from PNA. Electrochemical melting curves were produced by monitoring attenuation of the C=N chromophore stretch at 1593 cm^{-1}, and values for the melting potential generated from the first derivative of the melting curve (Figure 3.15.).

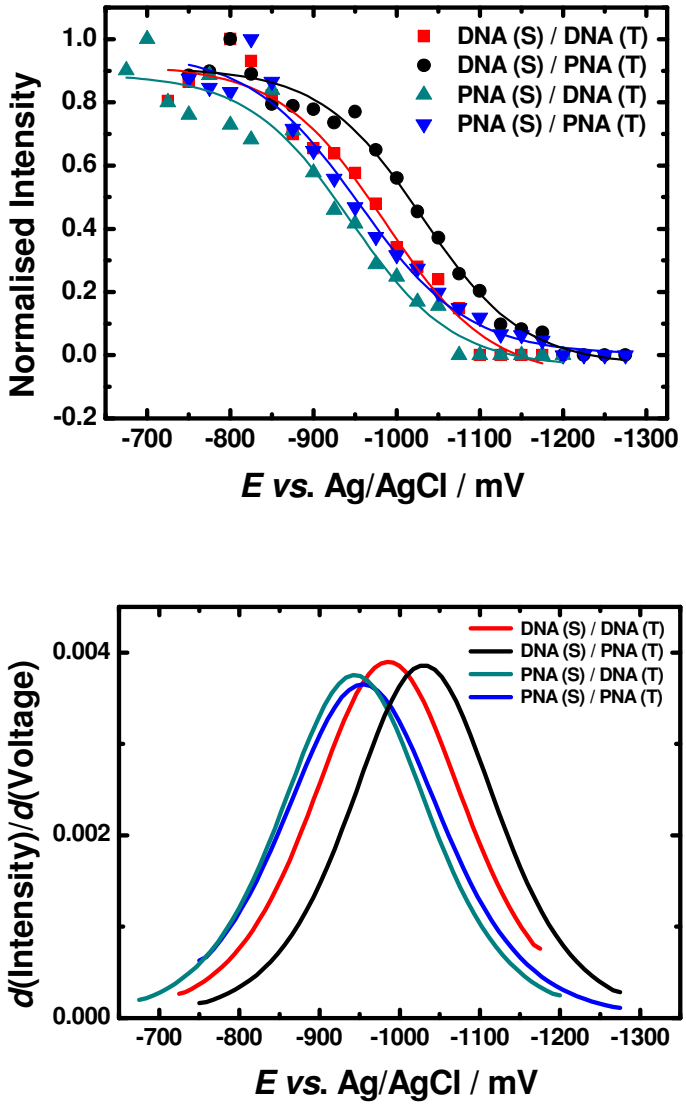

Figure 3.15. (A) The variation of the peak intensity at 1593 cm^{-1} as a function of applied potential for all four combinations of DNA and PNA. In each case the potential was swept at 0.5 mV s^{-1} from an initial potential of -0.3 V in pH 8.1 10 mM phosphate buffer containing 0.1 M NaCl. Spectra were acquired every 25 mV in static mode with a single 30 s acquisition. (B) First derivative plots indicative of melting potential based upon fitting a Boltzmann curve to the data set for each oligonucleotide. The electrochemical melting data is summarised in Table 3.4.

3.5.6. Discussion

The values of the melting potentials for the four possible combinations of probe and target showed only small variations when PNA was present in the surface immobilized duplex or not (Table 3.4.). This is in stark contrast to values for the melting temperature, where substitution of one or both strands in the oligonucleotide results in a significant (~ 30 °C) increase in thermal stability. Based on the data presented in Section 3.3, over a 270 mV cathodic shift in melting potential would have been expected when one of the strands in the immobilised duplex was substituted with PNA. The fact that duplexes consisting of PNA target can be electrochemically denatured rules out electrostatic repulsion between the electrode and the DNA backbone as possible mechanism for electrochemical melting.

Table 3.4. Predicted and Experimental values for the melting temperature (T_m) and melting potential (E_m) of the four possible probe-target duplexes. Both thermal and electrochemical melting experiments were carried out in a 10mM phosphate buffer (pH 8.1) containing 0.1 M NaCl.

Probe Strand	Target Strand	Predicted T_m* / °C	Experimental T_m /°C	Predicted E_m† /mV	Experimental E_m /mV
DNA	DNA	44.2	47	-957	-984
DNA	PNA	53.5	67	/	-1029
PNA	DNA	53.5	63	-1134	-941
PNA	PNA	/	> 80	/	-959

* Melting temperatures for all-DNA duplexes were calculated using nearest neighbor models as described in Section 3.2. Melting temperatures for PNA containing duplexes were calculated from the corresponding nearest-neighbor all-DNA duplex melting temperature using a published formula described by Norden and coworkers[15].

† Predicted melting potentials were calculated using values obtained for the experimental melting temperature, utilising Equation 3.7.

Melting potentials obtained from the experiments with PNA containing duplexes were compared to the results presented in Section 3.33 that correlated melting temperature and melting potential (Figure 3.4.). The melting potential of the all-DNA duplex was in good agreement with the predicted value, varying by only 27 mV. The melting potentials of the PNA containing duplexes were all significantly lower than expected, and varied depending on if the probe, target or both probe and target were constructed of PNA.

Substituting the thiol-modified DNA probe strand for PNA resulted in electrochemical denaturation becoming more difficult, and the melting potentials became more cathodic. Substituting the DNA labelled target strand for PNA resulted in electrochemical denaturation becoming less difficult, and the melting potentials became less cathodic.

The observed decrease in melting potential (-45 mV) upon substituting the target strand for PNA is consistent with the 4 °C difference in melting temperature observed when the labelled target strand is constructed of PNA and the thiolated probe strand from DNA instead of the reverse. This suggests that whilst the stabilising influence of the neutral backbone is largely ignored, the base-pair composition and the presence of terminal label groups does affect electrochemical melting,

The change in melting potential observed upon substituting the probe strand for PNA is more difficult to explain. Unlike for DNA, very little is known about the conformation and interaction of PNA molecules bound at an electrode surface, with few reported studies[30, 31]. One possibility is that the observed higher surface densities of immobilised PNA probes results in a decrease in duplex stability, particularly when the target strands are constructed from DNA and will readily repel one another at the electrode surface.

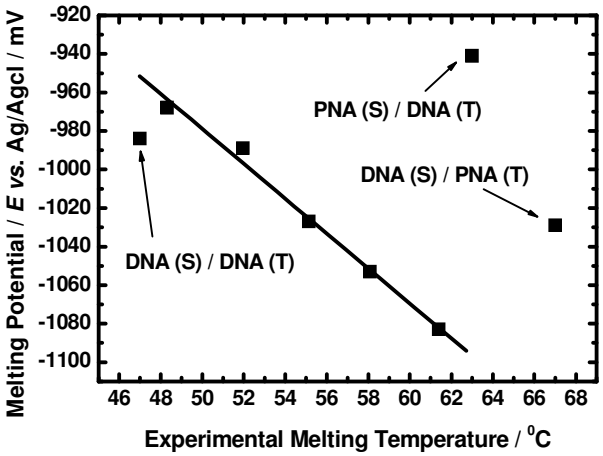

Figure 3.16. The relationship between melting potential and experimental melting temperature (from Figure 3.4), overlain with new data points that indicate the melting potentials of PNA-containing duplexes.

3.6. Summary

This chapter has introduced the concept of electrochemical melting. The electrochemical melting potential of a surface immobilised DNA duplex is directly related to its thermodynamic stability. Existing nearest neighbour models can be used to predict the stability of surface immobilised dsDNA, where a 1 °C increase in thermal stability equates to a -9 mV change in the electrochemical melting potential. This relationship can be exploited to design electrochemical melting assays with known melting potentials.

The effect of experimental temperature on electrochemical melting potential has been explored. Reducing the temperature at which the experiment is performed causes very little change in the electrochemical melting potential. Whilst unexpected, this result is advantageous when considering integration of the technology into a point-of-care device because there is little variation in results across the ambient temperature range.

Studies on the electrochemically driven denaturation of PNA containing duplexes indicate that the mechanism for electrochemical melting is not a simple electrostatic repulsion between the electrode surface and negatively charged sugar-phosphate backbone. Surface immobilised duplexes can be denatured even when the target strand is constructed from PNA, which has a neutral peptide backbone. Possible mechanisms for the electrochemical melting are discussed in further detail in Chapter 6.

3.7. References

1. J. SantaLucia, *Proc. Nat Acad. Sci.*, 1998, **95**, 1460-1465.
2. J. SantaLucia and D. Hicks, *Annu. Rev. Biophys. Biomol. Struct.*, 2004, **33**, 415-440.
3. P. E. Nielsen and G. Haaima, *Chem. Soc. Rev.*, 1997, **26**, 73-78.
4. R. Owczarzy, P. M. Vallone, F. J. Gallo, T. M. Paner, M. J. Lane and A. S. Benight, *Biopolymers*, 1997, **44**, 217-239.
5. R. Owczarzy, B. G. Moreira, Y. You, M. A. Behlke and J. A. Walder, *Biochemistry*, 2008, **47**, 5336-5353.
6. R. Owczarzy, Y. You, B. G. Moreira, J. A. Manthey, L. Huang, M. A. Behlke and J. A. Walder, *Biochemistry*, 2004, **43**, 3537-3554.
7. B. G. Moreira, Y. You, M. A. Behlke and R. Owczarzy, *Biochem. Biophys. Res. Commun.*, 2005, **327**, 473-484.
8. D. K. Corrigan, N. Gale, T. Brown and P. N. Bartlett, *Angew. Chem.*, 2010, **122**, 6053-6056.
9. S. Mahajan, J. Richardson, T. Brown and P. N. Bartlett, *J. Am. Chem. Soc.*, 2008, **130**, 15589-15601.
10. U. Rant, K. Arinaga, S. Fujita, N. Yokoyama, G. Abstreiter and M. Tornow, *Nano Lett.*, 2004, **4**, 2441-2445.
11. U. Rant, K. Arinaga, S. Scherer, E. Pringsheim, S. Fujita, N. Yokoyama, M. Tornow and G. Abstreiter, *Proc. Nat Acad. Sci.*, 2007, **104**, 17364-17369.
12. R. S. Greeley, W. T. Smith, R. W. Stoughton and M. H. Lietzke, *J. Phys. Chem.*, 1960, **64**, 652-657.
13. A. Bard and L. Faulkner, *Electrochemical Methods: Fundamentals and Applications, Second Edition*, John Wiley & Sons, New York, 2000.
14. L. Meites, ed., *Handbook of Analytical Chemistry*, McGraw-Hill, New York, 1963.
15. N. Ben Gaied, J. A. Richardson, D. G. Singleton, Z. Zhao, D. French and T. Brown, *Org. Biomol. Chem.*, 2010, **8**, 2728-2734.
16. P. Nielsen, M. Egholm, R. Berg and O. Buchardt, *Science*, 1991, **254**, 1497-1500.
17. P. E. Nielsen and M. Egholm, *Curr. Issues Mol. Biol.*, 1999, **1**, 89 - 104.
18. T. T. Nikiforov and S. Jeong, *Anal. Biochem.*, 1999, **275**, 248-253.
19. K. Petersen, U. Vogel, E. Rockenbauer, K. Vang Nielsen, S. Kølvraa, L. Bolund and B. Nexø, *Moll. Cell. Probe.*, 2004, **18**, 117-122.

20. M. Borgatti, A. Romanelli, M. Saviano, C. Pedone, I. Lampronti, L. Breda, C. Nastruzzi, N. Bianchi, C. Mischiati and R. Gambari, *Oncol. Res.*, 2003, **13**, 279-287.
21. V. V. Demidov, V. N. Potaman, M. D. Frank-Kamenetskil, M. Egholm, O. Buchard, S. H. Sönnichsen and P. E. Nlelsen, *Biochem. Pharmacol.*, 1994, **48**, 1310-1313.
22. B. M. McMahon, D. Mays, J. Lipsky, J. A. Stewart, A. Fauq and E. Richelson, *Antisense Nucleic Acid Drug Dev.*, 2002, **12**, 65-70.
23. U. Rant, K. Arinaga, T. Fujiwara, S. Fujita, M. Tornow, N. Yokoyama and G. Abstreiter, *Biophys. J.*, 2003, **85**, 3858-3864.
24. B. J. Kennedy, S. Spaeth, M. Dickey and K. T. Carron, *J. Phys. Chem. B.*, 1999, **103**, 3640-3646.
25. S. Lal, N. K. Grady, J. Kundu, C. S. Levin, J. B. Lassiter and N. J. Halas, *Chem. Soc. Rev.*, 2008, **37**, 898-911.
26. A. B. Steel, T. M. Herne and M. J. Tarlov, *Anal. Chem.*, 1998, **70**, 4670-4677.
27. K. Kneipp, H. Kneipp and M. Rentsch, *J. Mol. Struct.*, 1987, **156**, 331-340.
28. S. Mahajan, PhD Thesis, University of Southampton, Southampton, 2008.
29. H. Sato, M. Kawasaki, K. Kasatani and M.-a. Katsumata, *J. Raman. Spec.*, 1988, **19**, 129-132.
30. Y. Liu, D. Irving, W. Qiao, D. Ge and R. Levicky, *J. Am. Chem. Soc.*, 2011, **133**, 11588-11596.
31. P. Gong, K. Wang, Y. Liu, K. Shepard and R. Levicky, *J. Am. Chem. Soc.*, 2010, **132**, 9663-9671.

4. The Effect of the Aqueous Environment on Electrochemical Melting

4.1. Overview

Chapter three described how the stability of a DNA duplex is determined by its structure, and the effect that changes in DNA structure have on electrochemical melting. The aqueous environment surrounding a DNA duplex also has a profound effect on the stability of a duplex. This aqueous environment consists of the water molecules and dissolved ions that surround the duplex. This environment is typically described in terms of the ionic strength and pH of the solution. In this Chapter, the effects of solution pH and ionic strength on electrochemical melting are described and compared to the effects of ionic strength and solution pH on thermal melting experiments in bulk solution.

4.2. The Effect of pH on Electrochemical Melting

It is well known that dsDNA denatures in strongly acidic and basic solutions, and so, the possibility that electrochemically induced changes in surface pH conditions were responsible for the electrochemical denaturation process was investigated.

Typically, a pH shift to below 3 or to above 10 would be required to bring about denaturation of the DNA[1]. At high pH values, denaturation occurs because the bases of DNA become de-protonated and hydrogen bonding is disrupted. At low pH values, denaturation occurs because protonation of the base pairs disrupts hydrogen bonding, and additionally results in hydrolysis of the glycosidic bonds between purine bases in the sugar-phosphate backbone.

Several groups have demonstrated that *para*-mercaptobenzoic acid, a molecule that has a pH dependent SERS spectrum, can be used to spectroscopically monitor local pH changes at the surface of either silver[2, 3] or gold SERS substrates[4, 5]. In addition, mercaptobenzoic acid coated nanoparticles have been used extensively to map the pH

distribution within live cells[3, 6-8], and most recently in the monitoring of photodynamic treatment of cancer cells[9].

In this section, a *para*-mercaptobenzoic acid coated SERS substrate was used to monitor pH conditions *in situ* during an electrochemical melting experiment. The results demonstrate that a local pH change cannot be responsible for the voltage driven duplex denaturation observed in electrochemical melting, because no change in local pH was observed.

In addition to the increased insight gained into the electrochemical melting process, these results are of interest because pH plays an important role in many electrochemical reactions, and local pH conditions at the vicinity of an electrode surface are generally difficult to measure reliably.

4.2.1 Choice and Calibration of Probe Molecule

The SERS optical pH sensor is based on changes in the molecular structure of *p*MBA as a function of pH, as first reported by Halas and coworkers[4]. At low pH (acidic) values, the carboxylate group of the molecule is mostly protonated, and at high pH (basic) values the carboxylate group of the molecule is mostly de-protonated (Figure 4.1). These changes in molecular structure are reflected in the SERS spectra, specifically the bands at 1702 cm^{-1} (COO^-) and 1393 cm^{-1} (C=O) (Figure 1). Thus, a value for pH can be obtained from the ratio of intensities of these two peaks; (C=O) / (COO^-).

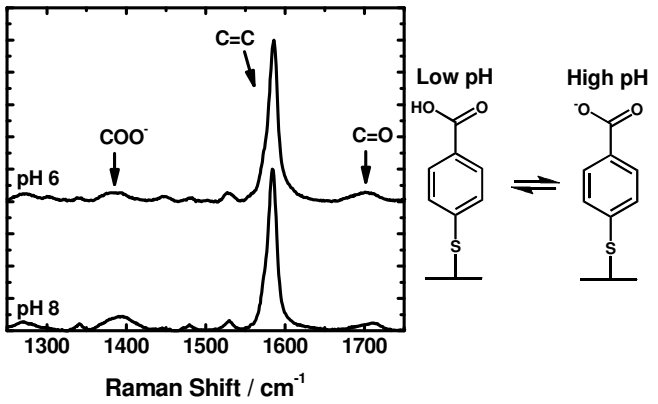

Figure 4.1. Basic principles of a *p*MBA SERS pH sensor. A change in the molecular structure of *p*MBA with pH; results in a spectral change in the C=O/COO^- peak ratio. SERS spectra were recorded in static mode with a single 10 s acquisition at a *p*MBA coated sphere segment void (SSV) substrate immersed in 10 mM phosphate buffer (0.1 M NaCl) corrected to within 0.01 units of the desired pH. The bands at 1702 cm^{-1}, 1584 cm^{-1} and 1393 cm^{-1} are assigned to the COO^-, C=C aromatic ring and C=O stretches respectively.

The SERS pH probe was calibrated over the pH range 6 – 8, the region in which electrochemical melting experiments are frequently carried out. The C=O/COO^- peak ratio changes linearly with pH, falling by circa 0.2 per increase in pH unit (Figure 4.2). The pH probe was calibrated using a dataset of 16 measurements. Although it was anticipated that the accuracy of the pH probe could be increased with a larger data set, 16 spectra were used as this is the approximate number of measurements that are obtained during an electrochemical melting experiment, and the interquartile range and mean values therefore provide a realistic representation of the range of peak ratios that can be expected during electrochemical melting.

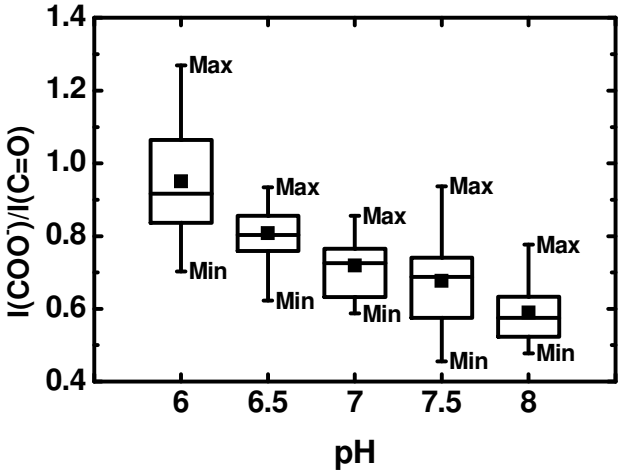

Figure 4.2. Calibration of the *p*MBA SERS pH sensor. Statistical box plot (percentages indicate quartile ranges) indicating the spectral change in the C=O/COO$^-$ peak ratio with pH. SERS spectra were recorded in static mode with a single 10 s acquisition at a *p*MBA coated sphere segment void (SSV) substrate immersed in 10mM phosphate buffer (0.1 M NaCl) corrected to within 0.01 units of the desired pH.

4.2.2 Use of the pH Probe in Combination with Immobilised dsDNA

To use *p*MBA as a pH Probe *in situ* during an electrochemical melting experiment, it was necessary to sequentially co-adsorb a number of other molecules onto the substrate surface. However, co-adsorption of multiple species at the surface of the SERS substrate results in a significant increase in the complexity of the spectral information obtained.

Mercapothexanol (MCH) and *para*-mercaptobenozic acid (*p*MBA) were added to the substrate surface in an approximately 50/50 ratio by soaking the ssDNA functionalized substrate in a 50/50 mix of *p*MBA and MCH dissolved in DMSO. Whilst the purpose of the *p*MBA is to act as the pH sensor, the MCH is used to re-orientate the immobilized DNA to an upright conformation[10, 11]. The resulting reorientation 'deactivates' any SERS signal from the DNA bases which might interfere with the signal from *p*MBA, as they now lie such that the bases are perpendicular to the substrate surface. Mercaptohexanol itself is largely Raman silent, although there is some overlap with the 1393 cm^{-1} of *p*MBA which results in changes

to the C=O/COO^- peak ratio. Additionally, the reorientation permits easy access to the bases for hybridization to a chosen labelled target nucleotide, which is introduced from solution[12-14].

Unfortunately, most commonly used Raman and fluorescent labels (e.g. cyanine dyes) have peaks that overlap with the 1393 cm^{-1} C=O band. For this reason, a nucleotide modified with Texas Red was chosen as the target strand, because Texas Red has only minimal contribution in this region. However, because Texas Red is pre-resonant with the available laser wavelength (633 nm), the response from this molecule is subject to an additional 10^2 enhancement above that which is seen for non-resonant SERS[15]. Thus, it was found initially that the signal from the Texas Red molecules overpowered the signal from the *p*MBA molecules. This issue was effectively circumnavigated by leaving approximately half of the dsDNA nucleotides unlabelled, thus reducing the overall SERS fingerprint of the Texas red relative to the *p*MBA (Figure 4.3c).

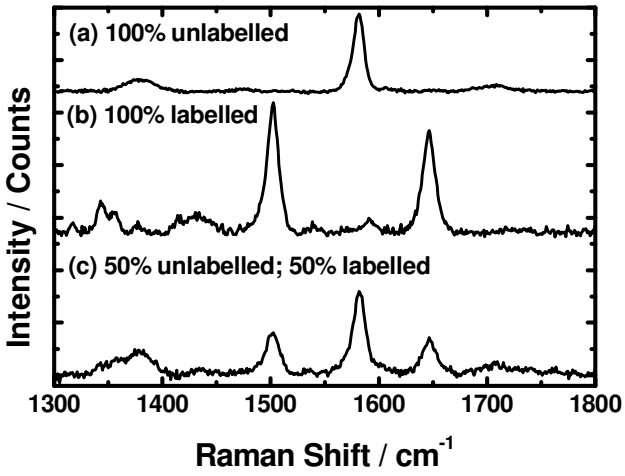

Figure 4.3. Spectra of pMBA/dsDNA sensor. The coverage of the dsDNA comprises 1% of the surface, and is hybridised to (a) 100% unlabelled target, (b) 100% labelled target, (c) 50% unlabelled and 50% labelled target. A dense under-layer covers the remaining 99% of the surface, and comprises of approximately 50% MCH and 50% *p*MBA. SERS spectra were recorded in static mode with a single 10 s acquisition at a sphere segment void (SSV) substrate immersed in 10mM phosphate buffer (0.1 M NaCl, pH 8.0). The bands at 1500 cm^{-1} and 1647 cm^{-1} are the ring stretch and NH deformation modes of Texas Red respectively. Band assignments for *p*MBA are shown in Figure 4.1.

As discussed in the preceding paragraphs, the addition of mercapothexanol, para-mercaptobenozic acid and labeled dsDNA results in changes in the spectral information acquired. To gauge the effect of co-absorption of these molecules on the C=O/COO^- peak ratio a second series of calibration experiments (Figure 4.4) were performed. This set of calibration data was then used to monitor the local pH during the subsequent electrochemical melting experiments.

In the co-immobilized system, both the C=O and the COO^- bands become more intense (relative to the *p*MBA aromatic ring stretch at 1581 cm^{-1}), and in particular the COO^- becomes significantly stronger. The result is a downward shift of the C=O/COO^- peak ratio as a function of pH. The intensity increase in the COO^- can be partially explained by some overlap with spectral features from both mercapothexanol and Texas Red. However, this does not explain the intensity increase in the C=O band (relative to the 1581 cm^{-1} *p*MBA peak). One possible explanation for these notable spectral changes can in part also be attributed to mercapothexanol having a similar reorientation effect on the *p*MBA to that which has been previously reported for DNA[10, 11, 16]. This would account for the increase in the intensity of all *p*MBA bands.

Despite the addition of numerous other molecules at the substrate surface, the data in Figure 4.4 clearly shows that the *p*MBA C=O/COO^- peak ratio still varies linearly as a function of pH, and thus its effectiveness as an optical pH probe is not compromised by the co-immobilization of the DNA and mercapothexanol at the substrate surface.

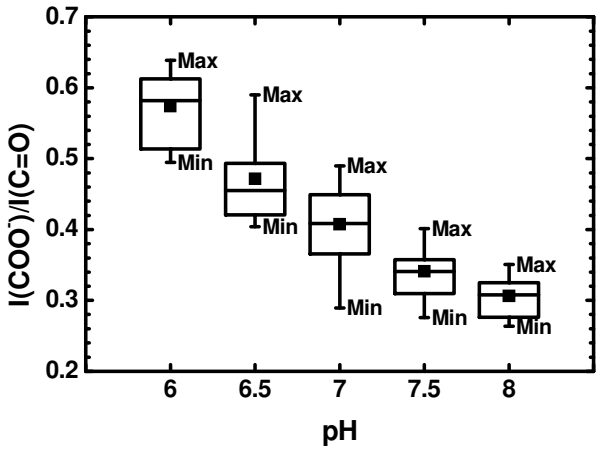

Figure 4.4. Calibration of the *p*MBA/dsDNA SERS pH sensor. The coverage of the dsDNA comprises 1% of the surface (of which 50% is unlabelled and 50% labelled), with a dense under-layer backfilling the remaining 99% of the surface, and comprising of approximately 50% MCH and 50% *p*MBA. Statistical box plot (percentages indicate quartile ranges) indicating the spectral change in the C=O/COO- peak ratio with pH. SERS spectra were recorded in static mode with a single 10 s acquisition at sphere segment void (SSV) substrate immersed in 10mM phosphate buffer (0.1 M NaCl) corrected to within 0.01 units of the desired pH.

4.2.3. Use of the pH probe in an Electrochemical Melting Experiment

To determine if a change in local pH is responsible for the denaturation of dsDNA into its constituent oligonucleotides during electrochemical melting three experiments were performed at pHs 6, 7 and 8. SERS was used to monitor denaturation (through the Texas Red peak intensity at 1500 cm^{-1} and 1650 cm^{-1}) whilst simultaneously monitoring the pH (through the 1393 cm^{-1} / 1702 cm^{-1} peak ratio) . The results of these experiments are plotted in Figure 4.5. For clarity, the *p*MBA C=O/COO^- peak ratio in each case is plotted on the same scale, and is overlaid with the interquartile range expected for the pH of the buffer used in the melting experiment.

Within experimental error, changes in surface pH were found to be insignificant as the potential is driven cathodic. Since a shift in pH to greater than 10 or less than 4 would be required to cause denaturation[1], changes in local pH cannot be responsible for electrochemical melting.

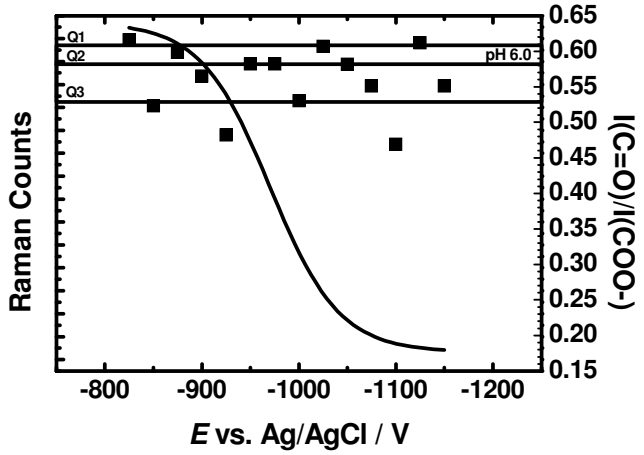
Q1
Q2
Q3
pH 6.0
Raman Counts
I(C=O)/I(COO-)
E vs. Ag/AgCl / V

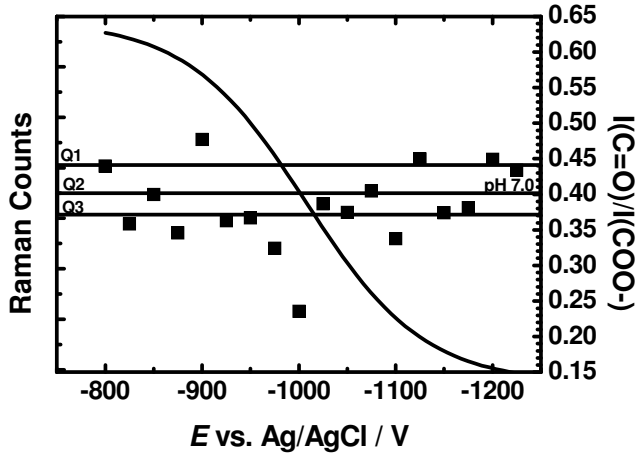
Q1
Q2
Q3
pH 7.0
Raman Counts
I(C=O)/I(COO-)
E vs. Ag/AgCl / V

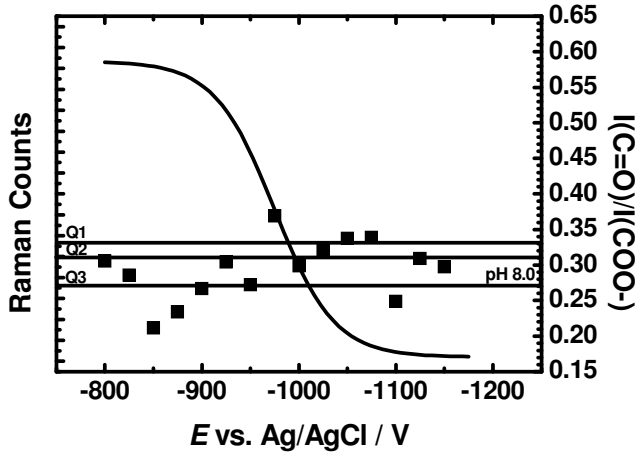
Q1
Q2
Q3
pH 8.0
Raman Counts
I(C=O)/I(COO-)
E vs. Ag/AgCl / V

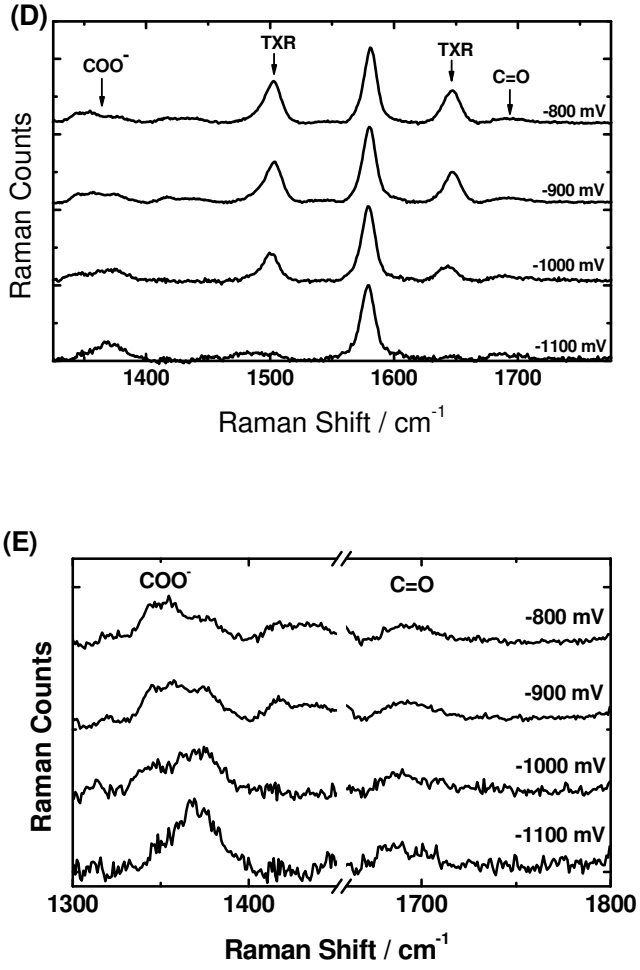

Figure 4.5. Electrochemical melting curves (black line) and C=O/COO^- peak ratios (black squares) as a function of applied potential at (a) pH 6, (b) pH 7 (c) pH 8, and (d, e) sample spectra as a function of potential at pH 6. The interquartile range of expected peak ratios for the pH of the buffer is overlaid as a guide to eye. SERS spectra were recorded in static mode with a single 10 s acquisition at a nano-void substrate immersed in 10mM phosphate buffer (0.1 M NaCl) corrected to within 0.01 units of the desired pH.

4.2.3. Effect of pH on the electrochemical melting potential

In addition to the data gathered for the local pH as a function of applied potential, these experiments permitted an opportunity to study the effect of pH on the melting potential itself. It was found that the melting potential is independent of pH over the range 6 -8 (Figure 4.6). This is in broad agreement with prior solution based thermal melting studies[1].

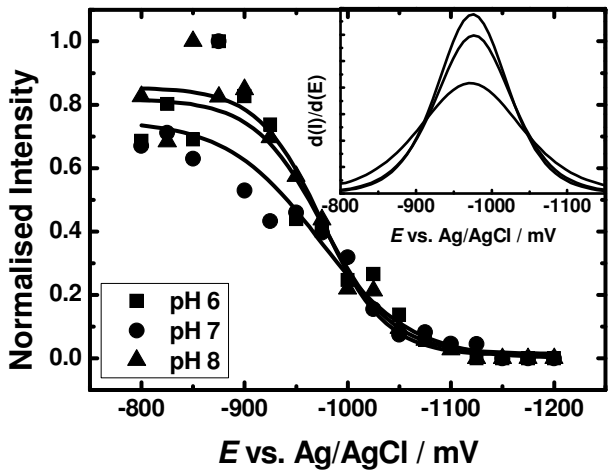

Figure 4.6. Electrochemical Melting curves and first derivative plots (inset) for melting experiments carried out at pH 6, 7 and 8. SERS spectra were recorded in static mode with a single 10 s acquisition at a nano-void substrate immersed in 10 mM phosphate buffer (0.1 M NaCl) corrected to within 0.01 units of the desired pH.

4.3. Effect of Ionic Strength on the Electrochemical Melting Potential

The ionic strength of a solution plays a pivotal role on the stability of dsDNA. In solution, the thermal melting temperature of a duplex increases rapidly as a function of the ionic strength (Figure 4.7). This is because the electrostatic interactions between phosphate groups are screened more readily as the number of counter-ions in solution increases. This is not a result of greater cation uptake by the duplex at higher salt concentrations, but rather, a shift in thermodynamic equilibrium.

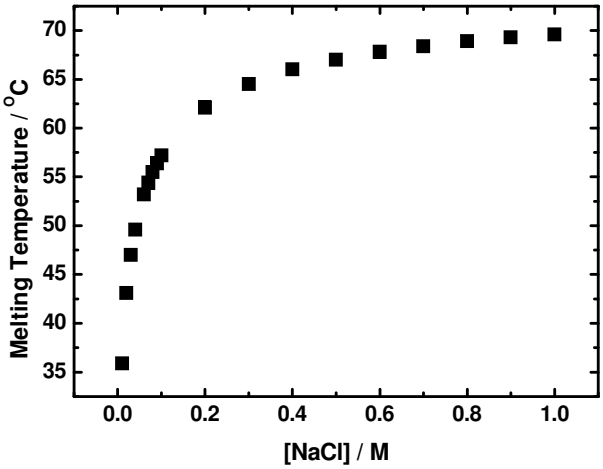

Figure 4.7. The effect of increasing salt concentration on nearest-neighbour melting temperature for 1 μM solution of dsDNA with the probe sequence AGGAAACACCAAAGATGATATT. Melting temperatures were calculated using the salt concentrations parameters of Owczarzy *et al.*[17], publicly available online at http://eu.idtdna.com/.

The number of cations that bind to single or double-stranded DNA remains constant regardless of the ionic strength of the bulk solution, and is determined only by the linear charge density (phosphate groups per unit length) of the DNA. This assumption is the cornerstone of Manning's theory of counter-ion condensation[18, 19*], which states that a fraction of the DNA charge will be compensated by counter-ions condensed at

[*] A more detailed mathematical treatment for DNA-cation binding involves utilization of the Poisson-Boltzmann and Debye-Huckel theories. A description of these models is well beyond the scope of this thesis but can be found in a recent review paper by Kornyshev *et al.*[19]

the surface. For a 1:1 salt, this fraction of charge, x, is given by the following expression:

$$x = 1 - \left(\frac{e^2}{\varepsilon k T b} \right)^{-1} = 1 - \left(\frac{b_j}{b} \right)^{-1} \qquad 4.1$$

Where e is the elementary charge, ε is the dielectric constant, k is the Boltzmann constant, T is the temperature, b_j is the Bjerrum length (~ 0.7 nm for water at 25 °C) and b is the axial distance between the charges. In DNA, these charges are the phosphate groups, which for ssDNA have a separation of 4 Å[17, 20, 21] and for dsDNA, 1.7 Å[17, 20]. Thus, for ssDNA the fraction of compensated charge is 0.44 and for dsDNA is 0.76.

Consider the equilibrium between DNA in its single and double forms.

$$\mathrm{ssDNA}_1(\mathrm{Na}^+)_{n_1} + \mathrm{ssDNA}_2(\mathrm{Na}^+)_{n_2} + \Delta n(\mathrm{Na}^+) \underset{\leftarrow}{\overset{\rightarrow}{}} \mathrm{dsDNA}_1(\mathrm{Na}^+)_{n_1+n_2+\Delta n} \qquad 4.2$$

Since the number of cations that bind to a dsDNA molecule is greater than the sum of the number of cations that bind to the two ssDNA molecules, hybridisation results in a net uptake of counter-ions. Conversely, denaturation of dsDNA into ssDNA results in a net release of counter-ions. At high ionic strengths, where there are a greater number of cations in solution, the equilibrium shifts the right and duplex stability increases. At low ionic strengths, where there are a smaller number of cations in solution, the equilibrium shifts to the left and denaturation is favoured.

As the ionic strength of the solution approaches and increases past 1 M, the melting temperature of DNA duplex begins to level off and then to decrease. At these very high ionic strengths, changes in dsDNA stability are determined by effects of the anion, which are known to destabilise dsDNA through hydrophobic interactions with the duplex and surrounding bulk water structure[20, 22, 23].

4.3.1. Reference Electrode Calibration

The spectro-electrochemical cell used for the electrochemical melting experiments employs a pseudo silver/silver chloride reference electrode which is in direct contact with the experimental buffer. As a consequence, the potential applied changes when the concentration of the salt in the buffer changes. To correct for this change, a calibration was performed by measuring the potential of the silver/silver chloride reference electrode *vs.* an external SCE electrode for each buffer used (Figure 4.8.). These corrections were applied to voltage values prior to data analysis and the determination of melting potentials. 10 mM Tris buffers (pH 7.2) of varying ionic strength were prepared by the addition of NaCl.

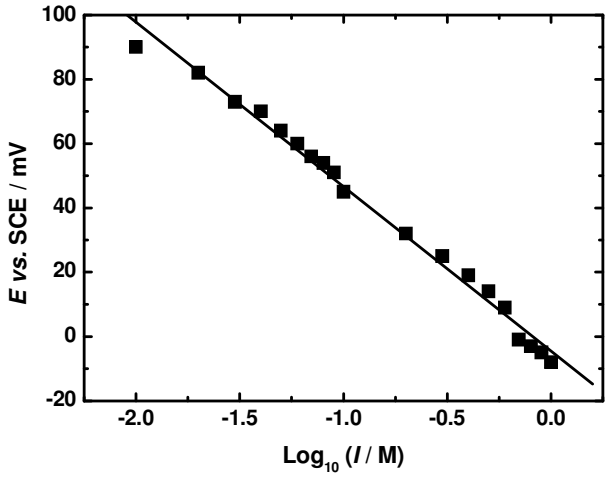

Figure 4.8. The potential of a pseudo Ag/AgCl reference electrode in contact with 10 mM Tris (pH 7.2) buffers of varying ionic strength at 22 °C.

The variation in the potential of the pseudo Ag/AgCl as a function of ionic strength was found to 51 mV M^{-1} (Figure 4.8). This is close to the expected value of 58 mV M^{-1} that would be predicted from the Nernst equation for the Ag/AgCl redox couple at 22 °C.

4.3.2. Effect of Ionic Strength on the Melting Potential

Electrochemical melting experiments were performed at a range of ionic strengths between 0.01 and 1 M. In each case all of the other experimental parameters (sweep rate, Raman acquisition times) were kept the same. Prior to experiment, the SSV substrate to which the dsDNA was immobilised was permitted to equilibrate for 30 minutes in a solution of the chosen ionic strength. The sequence of the probe DNA used in this experiment was AGGAAACACCAAAGATGATATT with a thiol anchor modification at the 5' as described in Chapter 2. The target sequence was perfectly complementary, and included a 3' Texas Red modification. Attenuation of the Texas red bands at 1500 cm^{-1} and 1650 cm^{-1} were used to monitor electrochemically driven denaturation, as described previously in Chapter 3.

The trend observed in the melting potentials is shown in Figure 4.9. At low ionic strengths (10 – 100 mM), the electrochemical melting potential was found to first become less cathodic, and then more cathodic again with increasing ionic strength. At high ionic strengths (> 100 mM) the electrochemical melting potential was found to decrease linearly with increasing ionic strength.

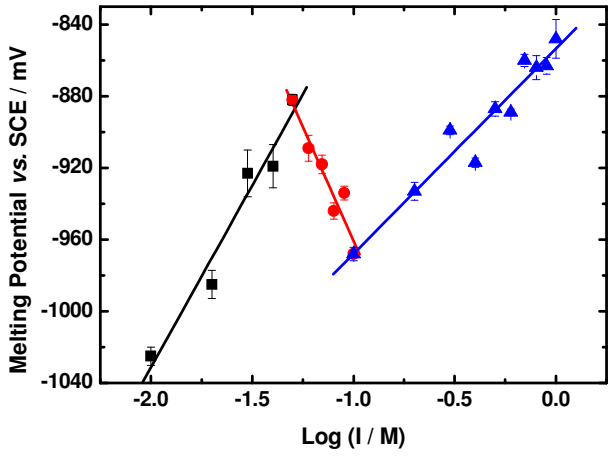

Figure 4.9. The observed effect of ionic strength on the electrochemical melting potential. The trend in melting potentials indicates electrochemical denaturation is hardest at low bulk ionic strengths, and easiest at the highest bulk ionic strengths.

Exemplar melting curves and first derivative plots are shown for electrochemical melting experiments at low ionic strengths in Figure 4.10 and for electrochemical melting experiments at high ionic strength in Figure 4.11.

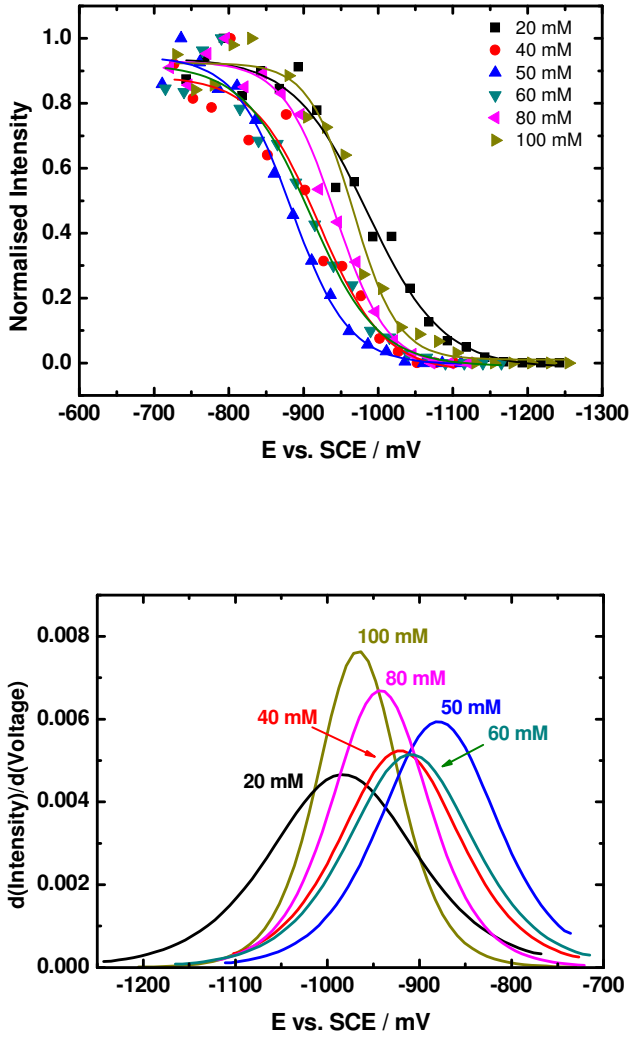

Figure 4.10. The trend in melting potential observed for the ionic strength range 10 – 100 mM. (A) The variation of the peak intensity at 1500 cm^{-1} as a function of applied potential. In each case the potential was swept at 1 mV s^{-1} from an initial potential of -0.3 V in pH 7.2 10 mM Tris buffer, and spectra collected in 25 mV intervals utilising a single 10 s acquisition. (B) First derivative plots indicative of melting potential based upon fitting a Boltzmann curve to the data set.

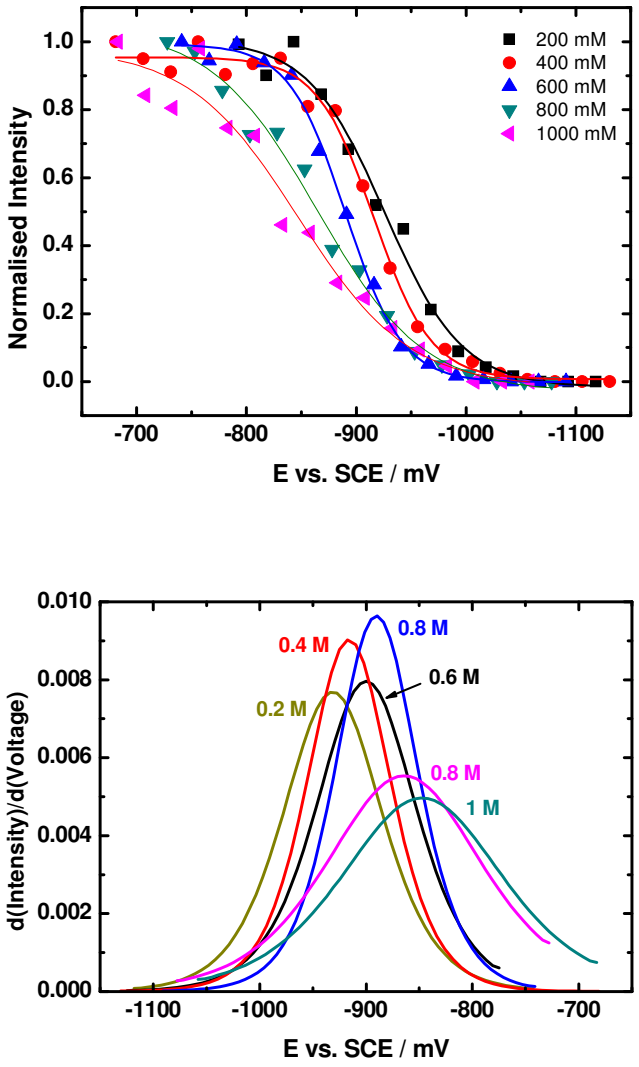

Figure 4.11. The trend in melting potential observed for the ionic strength range 100 – 1000 mM. (A) The variation of the peak intensity at 1500 cm^{-1} as a function of applied potential. In each case the potential was swept at 1 mV s^{-1} from an initial potential of -0.3 V in pH 7.2 10 mM Tris buffer, and spectra collected in 25 mV intervals utilising a single 10 s acquisition (B) First derivative plots indicative of melting potential based upon fitting a Boltzmann curve to the data set.

4.3.3. Discussion

The effect of ionic strength on the electrochemical melting potential is complex (Figure 4.9) and not easily explained. The following discussion examines what can be deduced about the composition of the solvent that surrounds the duplex and speculates about how this might affect the stability of the duplex.

The first difficulty is defining the precise nature of the solvent that surrounds the duplex, which in an electrochemical melting experiment, is surface bound. For the 22mer used in this study, it can be assumed that the duplex extends approximately 8.5 nm from the surface out into the solution. Whilst defining the bulk ionic strength is simple, applying a voltage at the electrode surface will result in a re-arrangement of the solvent as described by models for the electrochemical double layer (EDL)[24, 25].

The initial part of this discussion will utilise the Gouy-Chapman model, where the electric field drops exponentially as a function of distance from the electrode surface[24, 25].

Applying a potential of -0.9 V (with respect to the potential of zero charge) to a solution with a bulk ionic strength of 10 mM will result in the formation of an electrical double layer which extends approximately 3 nm from the surface and encompasses nearly half of the immobilised duplex. Within this EDL, the concentration of cations (Na^+) will be significantly greater than in the bulk.

The concentration of Na^+ at distance x from the electrode surface is given by[24]:

$$C_x^{Na^+} = C_0^{Na^+} \exp\left(-\frac{F\psi_x}{RT}\right) \qquad 4.3.$$

where F is the Faraday constant, R is the gas constant, T is the temperature and ψ_x is the potential at a distance x from the electrode surface, given by[24, 25]:

$$\psi_x = \psi_0 \exp(-kx) \qquad 4.4.$$

Here ψ_0 is the potential at the electrode surface and k^{-1} is the Debye length, which is determined by the ionic strength of the solution, I:

$$k^{-1} = \frac{1}{\sqrt{8\pi b_j N_A I}} \qquad 4.5.$$

where N_A is the Avogadro constant and b_j is the Bjerrum length (~ 0.7 nm at 25 °C).

Utilising equations, 4.3, 4.4 and 4.5 it is possible to make an estimate of the salt concentration 'felt' by the duplex at a distance x from the surface as a function of salt concentration (Figure 4.12).

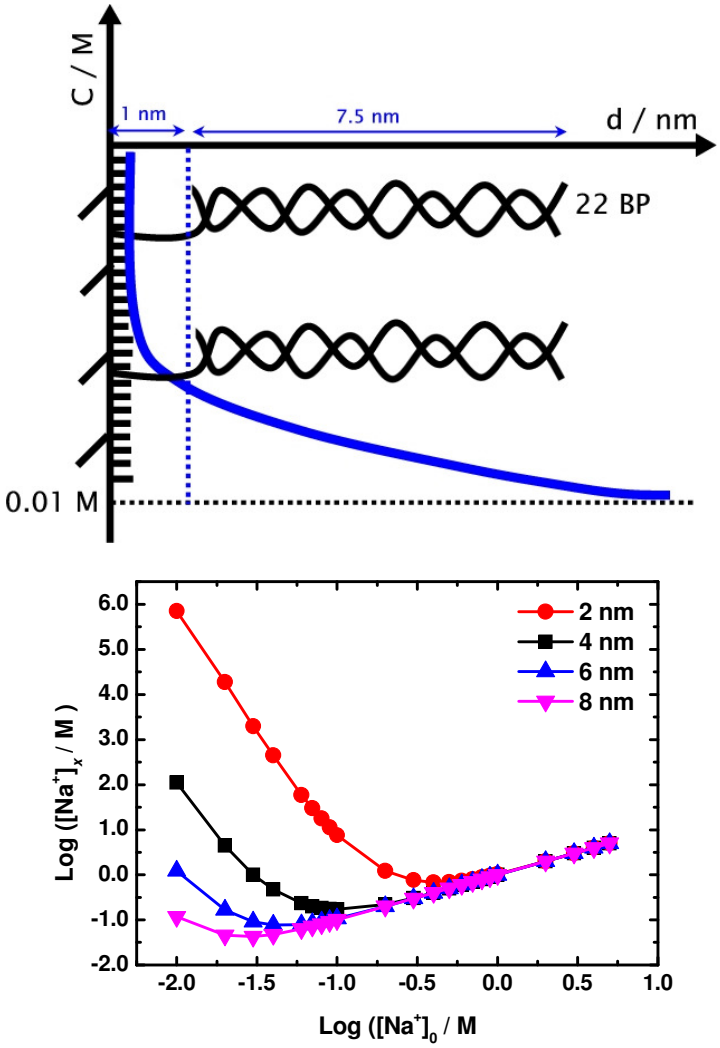

Figure 4.12. (A) graphical representation and (B) Calculated values demonstrating how the concentration of Na^+ ions at a distance *x* from the electrode surface varies relative to the bulk ionic strength at an applied potential of -0.9 V.

At low bulk concentrations, where the Debye length is large and the EDL extends far out into the solution, the DNA duplex experiences a salt concentration significantly higher than the bulk. As the bulk concentration increases and the Debye length decreases, the salt concentration 'felt' by the duplex reduces and eventually levels to the bulk salt concentration. In this regime, the electrical double layer is highly localised at the electrode surface and the salt concentration falls to the bulk value over the distance between the mercaptohexanol layer and the thiol anchor group (~ 0.5 nm), and before the first base-pair is reached.

The effective salt concentration can be utilised to explain the trends observed over low bulk salt concentrations (10 – 100 mM) where electrochemical melting becomes easier and then harder again. Figure 4.12 demonstrates that salt concentration 'felt' by the duplex decreases and then increases as the bulk concentration is increased, where the point of inflection depends on the values chosen for x and ψ_0, but is typically between 40 and 80 mM. It can therefore be argued that over the low range of ionic strengths (10 – 100 mM), the observed trend in melting potentials follows that observed for melting temperatures, once the local salt concentration at the surface is considered.

There is an assumption in this model that requires further clarification. The assumption is that the electric field does not contribute (or makes a minimal contribution to) the electrochemical denaturation. This assumption is justified because in Chapter 3 it was demonstrated that the mechanism of electrochemical melting was not an electrostatic repulsion between the sugar-phosphate backbone and the electrode surface through the denaturation of a peptide nucleic acid (PNA) duplex.

Whilst the aforementioned theory can be utilised to explain the trend over low bulk salt concentration, it does not give any insight into the electrochemical melting mechanism, nor does it explain the increasingly anodic melting potentials observed at high (> 100 mM) bulk ionic strengths. At these higher ionic strengths, the Debye length is short and the DNA duplex experiences no (or a very limited) electric field[24, 25]. The direct consequence of this is that the solvent surrounding the surface-immobilised duplex is anticipated to be of a similar structure to the bulk solution.

Until now the concentration of chloride ions has not been taken into consideration. At low bulk concentrations, where the EDL encompasses the DNA duplex, it will be comprised of very high concentrations of sodium ions but a minimal concentration of chloride ions by virtue of the Donnan exclusion principle. As the bulk salt concentration is increased, this will no longer be the case and the DNA duplex will be exposed to increasingly higher concentrations of chloride ions. Still ignoring any direct contribution to electrochemical melting by the electric field emanating from the electrode, the trend in melting potentials can now be depicted as an outcome of two competing factors. Whilst high concentrations of cations increase duplex stability and

push melting potentials to more cathodic values, high concentrations of anions decrease duplex stability and push melting potentials to more anodic values. Thus, the observed trend in melting potentials can now be explained by as follows (Figure 4.13):

1) At very low bulk salt concentrations, the effective Na^+ concentration felt by the duplex is very high and there is a significant stabilising effect. The concentration of Cl^- felt by the duplex is very low due to the Donan exclusion principle. When the bulk salt concentration increases to 50 mM, the effective Na^+ concentration felt by the duplex reaches a minimum because of the shortening Debye length, as shown in Figure 4.12.
2) Between 50 - 100 mM, the concentration of Na^+ again increases, and the electrochemical melting potentials become more cathodic. Increasing the salt concentration from 50 to 100 mM in a thermal melting experiment results in a large increase in dsDNA stability, and thus it can be assumed that over this range of bulk ionic strengths the stabilising effect of the increasing cation concentration is greater than the destabilising effect of the increasing anion concentration.
3) At some critical salt concentration (>100 mM), the destabilising effect of the anion becomes more significant than the stabilising effect of the cation and the electrochemical melting potentials become more anodic. This effect may be particularly potent for two reasons. Firstly, increasing the salt concentration beyond 100 mM in a thermal melting experiment results in only a small increase in stability. Secondly, the formation of a dense layer of cations near the electrode surface at high ionic strength may result in a region at some distance from the electrode surface where the net concentration of anions is greater than the net concentration of cations. This 'charge reversal' effect has been predicted by some recent simulations of the electrical double layer[26-29].

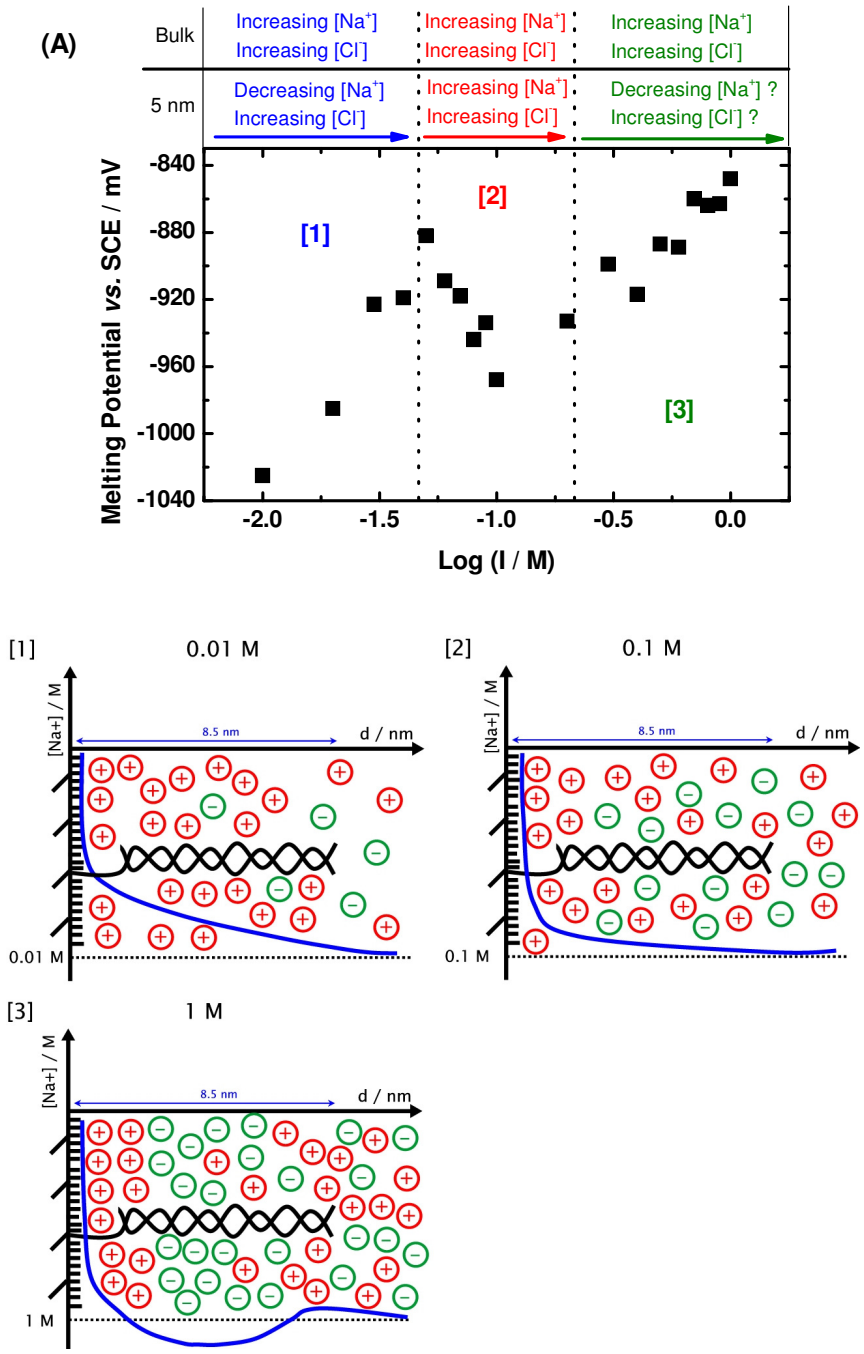

Figure 4.13. The impact of the electrical double layer of dsDNA stability as reflected by the observed trend in melting potentials. (A) The overall trend in melting potential as a function of bulk ionic strength, *I*. (B) Graphical representations illustrating the proposed structure of the double layer at bulk ionic strengths of [1] 0.01 M, [2] 0.1 M and [3] 1 M, where charge reversal might apply.[26-29]

4.3.4. The relationship between Ionic Strength, Strand Length, and Melting Potential

The effect of the electrical double layer on the stability on the immobilised dsDNA has important consequences when considering the relative melting potentials of DNA duplexes of different lengths. Consider the nature of the ionic environment in the proximity of a 14 and a 22 base-pair surface immobilised duplex when the bulk ionic strength is 0.1 M (Figure 4.14.). Upon applying a negative potential at the surface, the electrical double layer will form, and assuming a simple Gouy-Chapman model[24, 25], the concentration of cations at some distance x from the surface will given by Equation 4.1, as described earlier.

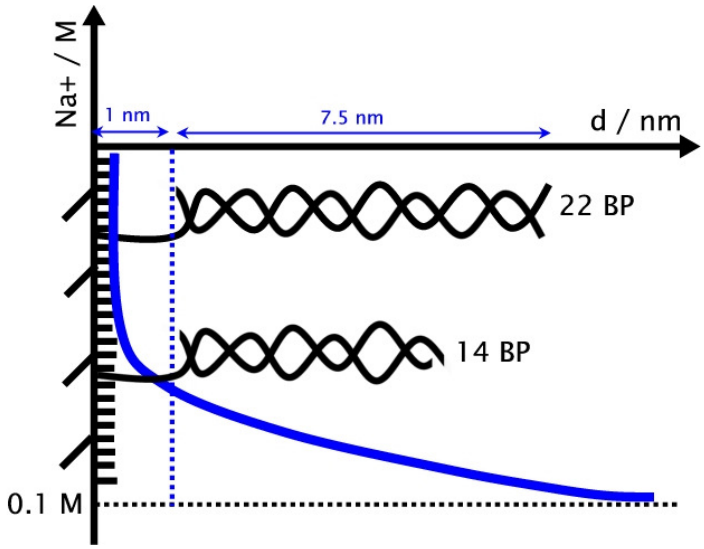

Figure 4.14. Graphical representation illustrating the extent to which the composition of the electrical double layer (EDL) can exert an influence on immobilised duplexes of differing length. At a bulk ionic strength of 0.1M, the majority of a 14bp duplex is expected to lie within the EDL, whilst much of a 22bp duplex is expected to lie outside of it.

A larger proportion of the shorter (14 base-pair) strand will lie within the region of electrical double layer which has heightened salt concentration relative to the bulk. The model described in Section 4.3.3. therefore predicts that shorter strands of immobilised dsDNA will be preferentially stabilised and have melting potentials that are more cathodic than longer strands of similar thermal stability.

Whilst a full study of the effect of dsDNA length on the electrochemical melting temperature was not performed, analysis of the existing available data appeared to validate this prediction (Figure 4.15.).

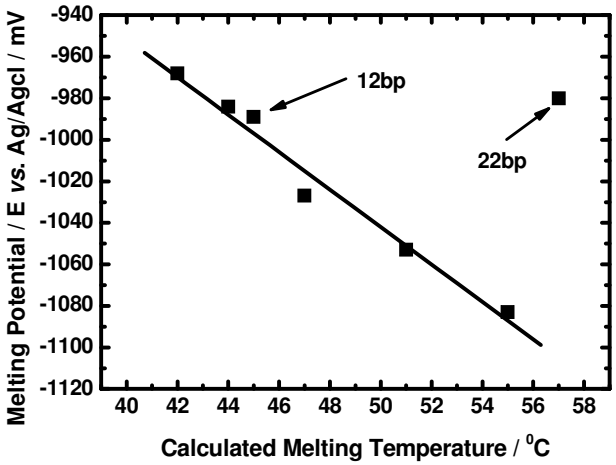

Figure 4.15. The relationship between nearest-neighbour melting temperature and melting potential described in Chapter 3, now overlain with new data for 12 and 22 base-pair duplexes. The longer 22 base-pair duplex has a melting potential significantly less negative than predicted.

Caution must therefore be advised when predicting the melting potential of a surface-immobilised dsDNA utilising the equations and methods described in Chapter 3, because the determined relationship between melting temperature and melting potential (1 °C = 9 mV) applies only to dsDNA that is 14 base-pairs in length.

Clearly, further experiments are required before it will be possible to fully characterise the relationship between melting potential and strand length. However, after this is accomplished, it should be possible to introduce a correction parameter into the formulae described in Chapter 3 so that the melting potential of any surface-immobilised dsDNA strand can be predicted, regardless of its length or structure.

4.4. The Effect of Different Cations on the Electrochemical Melting Potential

4.4.1. Overview

A series of experiments were performed to determine what affect different cations of chloride had on the electrochemical melting potential. So far, it has been shown that electrochemical melting potentials are directly related to their counterpart melting temperatures, suggesting that electrochemical melting directly probes the thermodynamics of the DNA duplex. It was therefore expected that any change in the cation used would result in only small changes in the melting potential (over the mono-valent salts), < 25 mV (3 °C), and would follow the well-established order[30, 31]:

$Na^+ \sim K^+ < Cs^+ \sim NH_4^+ < Cs^+ < Li^+ << Mg^{2+}$

Electrochemical melting curves were obtained in buffers of containing varying cations of chloride with a total ionic strength of 0.5 M. The sequence of the probe DNA used in these experiments was AGGAAACACCAAAGATGATATT with a thiol anchor modification at the 5' as described in Chapter 2. The target sequence was perfectly complementary, and included a 3' Texas Red modification. Attenuation of the Texas red bands at 1500 cm^{-1} and 1650 cm^{-1} were used to monitor electrochemically driven denaturation, as described previously in Chapter 3.

Melting profiles at an ionic strength of 0.5 M are shown in Figure 4.16.

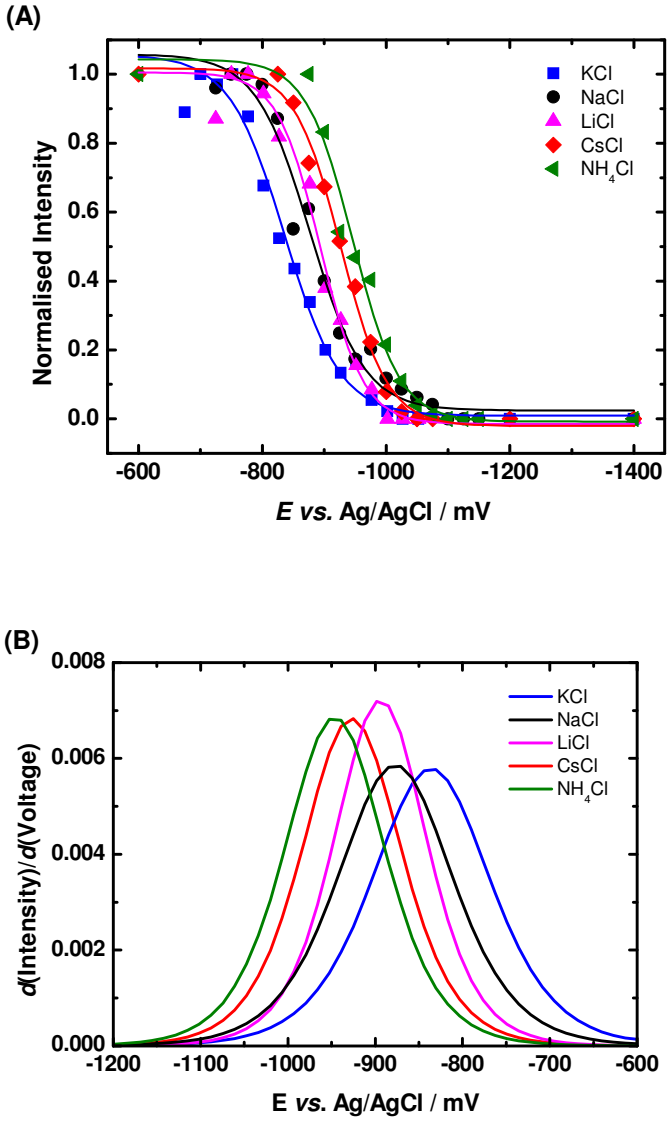

Figure 4.16. (A) The variation of the peak intensity at 1500 cm^{-1} as a function of applied potential. In each case the potential was swept at 1 mV s^{-1} from an initial potential of -0.3 V in pH 7.2 10 mM Tris buffer, and spectra were acquired every 25 mV in static mode with a single 10 s acquisition. (B) First derivative plots indicative of melting potential based upon fitting a Boltzmann curve to the data set.

4.4.2. Discussion

Different mono-valent cations have been shown to have a very minor effect on the thermal stability (< 3 °C as measured by melting temperature from Na^+ to Li^+) of a dsDNA duplex, where the order observed is[30, 31]:

$$Na^+ \sim K^+ < Cs^+ \sim NH_4^+ < Li^+$$

However, the ordering of the cations in terms of stability under an applied potential gradient (as measured by the melting potential) is as follows:

$$K^+ < Na^+ < Li^+ < Cs^+ < NH_4^+$$

In addition to a very different sequential order, the effect of changing the cation is much more pronounced than for thermal melting, that is, there is almost a 90 mV shift in the melting potential from K^+ to NH_4^+, which based on our previous results, equates to melting temperature shift of 12 °C. This compares to just a 3 °C shift in melting temperatures observed between K^+ and NH_4^+ observed in thermal melting experiments.

It is possible to speculate about the observed mono-valent cation order by comparing our results to those previously published that describe the relative binding affinity of different mono-valent cations for DNA.

Bleam *et al.* obtained binding affinity data for a variety of mono-valent cations by using NMR line-width measurements[32]. In a series of experiments, they measured the displacement of Na^+ ions from a DNA helix upon introduction of another cation, and obtained the following order:

$$Na^+ < K^+ < Li^+ < Cs^+ < NH_4^+$$

With the exception of K^+, the ordering is identical to that observed for the melting potentials in our experiments. Indeed, plotting data for the competition parameter, *D*, (a measure of how easily Na^+ is displaced from DNA by another cation) obtained from their work as a function of the melting potential yields a straight line with a strong correlation (Figure 4.17).

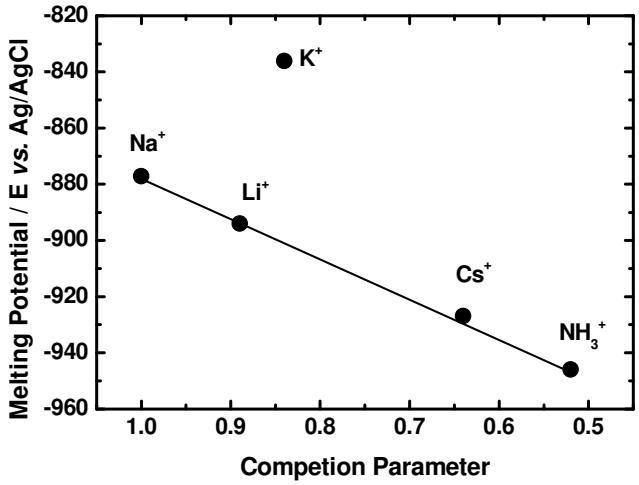

Figure 4.17. Plot of melting potentials vs. the competition parameter, an indicator of relative binding affinity, at a fixed ionic strength of 0.5 M. Values for the competition parameter have been taken from reference 32.

Denisov and Halle reported the same ordering as Bleam *et al.* in a recent publication where they used ^{23}Na NMR quadrapole relaxation studies to determine cation-binding affinity[33]. Electrophoretic measurements by Ross and Scrugs[34] deduced the relative binding affinity to be $K^+ < Na^+ < Li^+$, in perfect agreement with the order of melting potentials we have obtained.

In addition to experiments designed to directly measure relative binding affinities, there have been several studies that propose to indirectly reflect relative binding affinities because of the importance of the cations on dsDNA conformation. Anderson and Bauer[35] measured the extent of DNA super-coiling using viral PM2 DNA as a function of ion type and concentration, and obtained the following order:

$Na^+ < K^+ < Li^+ < Rb^+ < Cs^+ < NH_4^+$

Again, this order is identical to which we have obtained, with the exception of K^+ whose position differs not only with the electrochemical melting data but also with the results of Bleam *et al.* Precisely the same order was also obtained by Hanlon *et al.*, who examined the effect of different cations on the circular dichroism of calf thymus DNA in solution[36-38].

In a simplistic model, the ionic environment around a dsDNA helix can be separated into two parts. There are ions that sit in a diffuse cloud around the DNA helix, and secondly, ions that deeply penetrate into the dsDNA structure and are partially condensed in the spine of hydration and/or the duplex grooves[19, 32, 33]. Based on the data presented here, it seems pertinent to conclude that these deeply penetrating ions are highly involved in the underlying electrochemical melting mechanism, as changing the mono-valent cation involved has a significant impact on the melting potential.

4.5. Summary

This chapter has described the way in which the pH and ionic composition of the experimental buffer affects the electrochemical melting potential. In addition, some possible mechanisms for the electrochemical melting process have been disproved.

It was shown that *p*MBA adsorbed at an SSV substrate can be used as an effective pH sensor over the pH range 6 – 8. *In situ* monitoring of local pH conditions during a spectro-electrochemical experiment by using SERS was demonstrated for the first time. The results show that there is no pH change during the potential driven melting of immobilised dsDNA, and that the electrochemical melting potential is independent of pH over the range 6 - 8, in broad agreement with prior solution based thermal melting studies.

The way in which the electrochemical melting potential varies as a function of ionic strength was found to be complex. A qualitative hypothesis for the trend in melting potentials has been described based on the structure of the electrochemical double layer at the SSV surface. At low ionic strengths, where the double layer encompasses most of dsDNA length, the concentration of cations 'felt' by the DNA is higher than the bulk. As the ionic strength increases, the localised cation concentration falls and then rises again, reflecting the trend in melting potentials. At high ionic strengths (> 0.1 M), the melting potentials become more anodic again. One possible explanation for this is that the compact layer of cations close to the electrode surface results in a net increase in anions in proximity to the DNA due to charge reversal[26-29].

Finally, the effect of changing the cation in the experimental buffer was described. The results suggest that those ions that bind most tightly to the duplex cause the greatest increase in duplex resistance to electrochemical melting.

4.6. References

1. R. H. Garrett and C. M. Grisham, *Biochemistry*, Brooks/Cole, Cengage Learning, Boston, MA, 2010.
2. J. Kneipp, B. Wittig, H. Bohr and K. Kneipp, *Theor. Chim. Act.*, 2010, **125**, 319-327.
3. J. Kneipp, H. Kneipp, B. Wittig and K. Kneipp, *Nano Lett.*, 2007, **7**, 2819-2823.
4. S. W. Bishnoi, C. J. Rozell, C. S. Levin, M. K. Gheith, B. R. Johnson, D. H. Johnson and N. J. Halas, *Nano Lett.*, 2006, **6**, 1687-1692.
5. A. M. Schwartzberg, T. Y. Oshiro, J. Z. Zhang, T. Huser and C. E. Talley, *Anal. Chem.*, 2006, **78**, 4732-4736.
6. J. Kneipp, H. Kneipp, B. Wittig and K. Kneipp, *J. Phys. Chem. C.*, 2010, **114**, 7421-7426.
7. S. Zong, Z. Wang, J. Yang and Y. Cui, *Anal. Chem.*, 2011, **83**, 4178-4183.
8. C. E. Talley, L. Jusinski, C. W. Hollars, S. M. Lane and T. Huser, *Anal. Chem.*, 2004, **76**, 7064-7068.
9. Š. Bálint, S. Rao, M. Marro, P. Miškovský and D. Petrov, *J. Raman. Spec.*, 2011, **42**, 1215-1221.
10. D. Erts, B. Polyakov, H. Olin and E. Tuite, *J. Phys. Chem. B.*, 2003, **107**, 3591-3597.
11. C.-Y. Lee, P. Gong, G. M. Harbers, D. W. Grainger, D. G. Castner and L. J. Gamble, *Anal. Chem.*, 2006, **78**, 3316-3325.
12. S. D. Keighley, P. Estrela, P. Li and P. Migliorato, *Biosens. Bioelectron.*, 2008, **24**, 906-911.
13. U. Rant, K. Arinaga, S. Fujita, N. Yokoyama, G. Abstreiter and M. Tornow, *Nano Lett.*, 2004, **4**, 2441-2445.
14. U. Rant, K. Arinaga, S. Scherer, E. Pringsheim, S. Fujita, N. Yokoyama, M. Tornow and G. Abstreiter, *Proc. Nat Acad. Sci.*, 2007, **104**, 17364-17369.
15. S. Mahajan, J. J. Baumberg, A. E. Russell and P. N. Bartlett, *Phys. Chem. Chem. Phys.*, 2007, **9**, 6016-6020.
16. K. Arinaga, U. Rant, M. Tornow, S. Fujita, G. Abstreiter and N. Yokoyama, *Langmuir*, 2006, **22**, 5560-5562.
17. R. Owczarzy, Y. You, B. G. Moreira, J. A. Manthey, L. Huang, M. A. Behlke and J. A. Walder, *Biochemistry*, 2004, **43**, 3537-3554.
18. G. S. Manning, *J. Chem. Phys.*, 1969, **51**, 924-933.
19. A. A. Kornyshev, D. J. Lee, S. Leikin and A. Wynveen, *Rev. Mod. Phys.*, 2007, **79**, 943.
20. S. Tomac, M. Sarkar, T. Ratilainen, P. Wittung, P. E. Nielsen, B. Nordén and A. Gräslund, *J. Am. Chem. Soc.*, 1996, **118**, 5544-5552.
21. U. Rant, K. Arinaga, T. Fujiwara, S. Fujita, M. Tornow, N. Yokoyama and G. Abstreiter, *Biophys. J.*, 2003, **85**, 3858-3864.
22. K. Hamaguchi and E. P. Geiduschek, *J. Am. Chem. Soc.*, 1962, **84**, 1329-1338.
23. R. Owczarzy, University of Illinois, Chicago, 1999.
24. D. Pletcher, *A First Course in Electrode Processes*, RSC Publishing, Cambridge, 2009.
25. A. Bard and L. Faulkner, *Electrochemical Methods: Fundamentals and Applications, Second Edition*, John Wiley & Sons, New York, 2000.

26. G. I. Guerrero-García, E. González-Tovar, M. Chávez-Páez and M. Lozada-Cassou, *J. Chem. Phys.*, 2010, **132**, 054903 - 054913.
27. F. Jiménez-Ángeles and M. Lozada-Cassou, *J. Phys. Chem. B.*, 2004, **108**, 7286-7296.
28. L. Sjöström, T. Åkesson and B. Jönsson, *Ber Bunsen. Phys. Chem.*, 1996, **100**, 889-893.
29. G. I. Guerrero-García, E. González-Tovar and M. Chávez-Páez, *Phys. Rev. E.*, 2009, **80**, 021501.
30. D. E. Dix and D. B. Straus, *Arch. Biochem. Biophys.*, 1972, **152**, 299-310.
31. S.-i. Nakano, M. Fujimoto, H. Hara and N. Sugimoto, *Nucleic Acids Res.*, 1999, **27**, 2957-2965.
32. M. L. Bleam, C. F. Anderson and M. T. Record, *Biochemistry*, 1983, **22**, 5418-5425.
33. V. P. Denisov and B. Halle, *Proc. Nat Acad. Sci.*, 2000, **97**, 629-633.
34. P. D. Ross and R. L. Scruggs, *Biopolymers*, 1964, **2**, 231-236.
35. P. Anderson and W. Bauer, *Biochemistry*, 1978, **17**, 594-601.
36. A. Chan, R. Kilkuskie and S. Hanlon, *Biochemistry*, 1979, **18**, 84-91.
37. S. Hanlon, S. Brudno, T. T. Wu and B. Wolf, *Biochemistry*, 1975, **14**, 1648-1660.
38. B. Wolf and S. Hanlon, *Biochemistry*, 1975, **14**, 1661-1670.

5. Label Free DNA Detection and Discrimination

5.1. Overview

In Chapters three and four, it was demonstrated that the denaturation of dsDNA at an electrode surface can be monitored by the changes in SERS signal from a reporter molecule covalently attached to the target strand. This method can be utilised to distinguish between different sequences in DNA. Unfortunately, the need to covalently attach a SERS active label to the DNA target prior to detection reduces the effectiveness of the technology because synthetic pre-treatment of the DNA target to be analysed is required.

This is a common problem with many DNA detection and discrimination assays. The time, difficulty and expense of synthetically pre-treating a target analyte greatly diminishes the effectiveness of the assay. Furthermore, the synthesis, which must be conducted in a laboratory, inherently makes the technology challenging to integrate into a device that could be used at the point of care. To this end, there has been a growing interest in 'label free detection'.

The precise definition of 'label free' is often unclear, because most 'label free' assays still rely on the detection of a reporter molecule by using a spectroscopic or electrochemical method of some description. In the context of the research described in this thesis, 'label free' refers to the detection and discrimination of DNA without the requirement to synthetically pre-treat the DNA to be detected prior to analysis.

Several groups have reported label-free methods of detecting DNA in recent years, including the use of carbon nano-tube network field-effect transistors[1, 2], florescence[3], nano-mechanical cantilevers[4] and surface plasmon resonance[5, 6].

Plaxco *et al.* have pioneered the use of methylene blue labelled aptamers that produce an increased electrochemical response upon binding of a target oligonucleotide[7-10]. Initially, the methylene blue redox label is held at a position far from surface. Upon binding, the aptamer folds such that the methylene blue is in a position closer to the

electrode surface, permitting electron transfer, and the recorded Faradic current increases significantly[8, 11]. This type of assay can be 'termed' label free because no-prior modification of the target strand to be detected is required. Label free detection using impedance spectroscopy has also been reported[12-14], but the sensitivity of impendence measurements to small changes in environmental conditions leaves the reproducibility and reliability of this method open to debate.

There are very few reports of label-free detection of DNA utilising SERS. Halas and co-workers have demonstrated the label-free detection of DNA by substitution of adenine in a surface-immobilised probe sequence with 2-amino purine[15]. This substitution removes the characteristic adenine bands that typically dominate the SERS spectra of DNA[16]. A target oligonucleotide can then be detected by re-appearance of adenine bands in the spectra upon hybridisation. A recent report by Bell *et al.* demonstrated that single-base mismatches can be detected directly from unlabelled and unmodified oligonuclotides by utilising $MgSO_4$ aggregated silver colloids[17]. In this report, the DNA is bound non-specifically through the individual bases which lie perpendicular to the colloid surface.

In this Chapter, the 'label free' detection of DNA via the use of dsDNA selective binding agents is demonstrated. These binding agents interact non-covalently and selectively with surface-immobilised dsDNA and thus no synthetic pre-treatment of the target oligonucleotide to be detected is required. The 'Label free' detection of dsDNA at an SSV surface has been combined with the thermal and electrochemical denaturation methods developed in previous chapters to demonstrate the discrimination of DNA sequences responsible for the mutations in the CFTR gene.

5.2. DNA Binding Molecules

5.2.1. Modes of Binding

There are three main ways in which dsDNA can bind non-covalently to a small molecule (Figure 5.1):

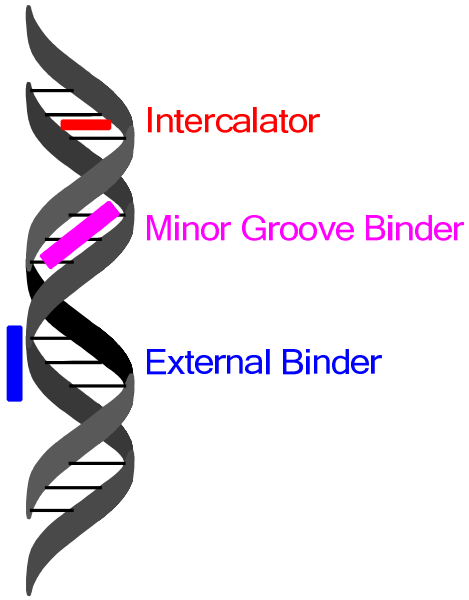

Figure 5.1. Diagram illustrating the various ways in which small molecules can bind non-covalently to DNA, including groove-binding, intercalation and electrostatic interactions.

External Binders

Positively charged molecules can bind electrostatically to the backbone of DNA through the negative charges on the phosphate backbone. Although electrostatic interactions could be used to detect the presence of DNA at the SERS surface, it is not specific to dsDNA and therefore not suitable for monitoring DNA denaturation.

Intercalation

A number of flat, aromatic molecules can interact by intercalation between base pairs in DNA. Intercalation typically results in conformational changes in the DNA duplex. Intercalated molecules are generally flat and aromatic, and they lie in plane with the base pairs of DNA. In an electrochemical melting assay, the DNA bases are assumed to be parallel to the surface, and by virtue of the Raman surface selection[18, 19] rule this

theoretically makes intercalated molecules very difficult to detect. Examples of intercalators include acridine orange and ethidium bromide. An additional consideration when utilising intercalating molecules is their high toxicity. Ethidium bromide for example, is highly mutagenic and requires specialist handling and disposal procedures.

Minor groove binders

Minor groove binders interact with DNA by binding into the deep narrow groove of dsDNA upon. Examples of minor groove binders include the DNA stains DAPI and Hoechst 33258. Since the interaction is specific to dsDNA, and the minor groove is not typically parallel to the SERS surface, this class of molecule theoretically offers the best prospects for monitoring dsDNA denaturation.

5.2.2. Choice of Binding Agent.

In total, six binding agents were screened as potential DNA binding agents for utilisation in a SERS detection and discrimination assay, the structures of which are shown in Figure 5.2. Both intercalators and minor-groove binders were screened as potential binding agents. Whilst minor-groove binders will theoretically provide better SERS signals than intercalators because of their orientation with respect to the surface, most intercalators have at least some functional groups that lie perpendicular to the base-pairs between which they are situated, and these should still be detectable.

The properties of the six binding agents are shown in Table 5.1. Three of the dyes chosen are resonant with the pump laser (633 nm HeNe) used to collect the SERS spectra, and it was anticipated that this would provide an additional resonant Raman effect and increase the sensitivity of detection.

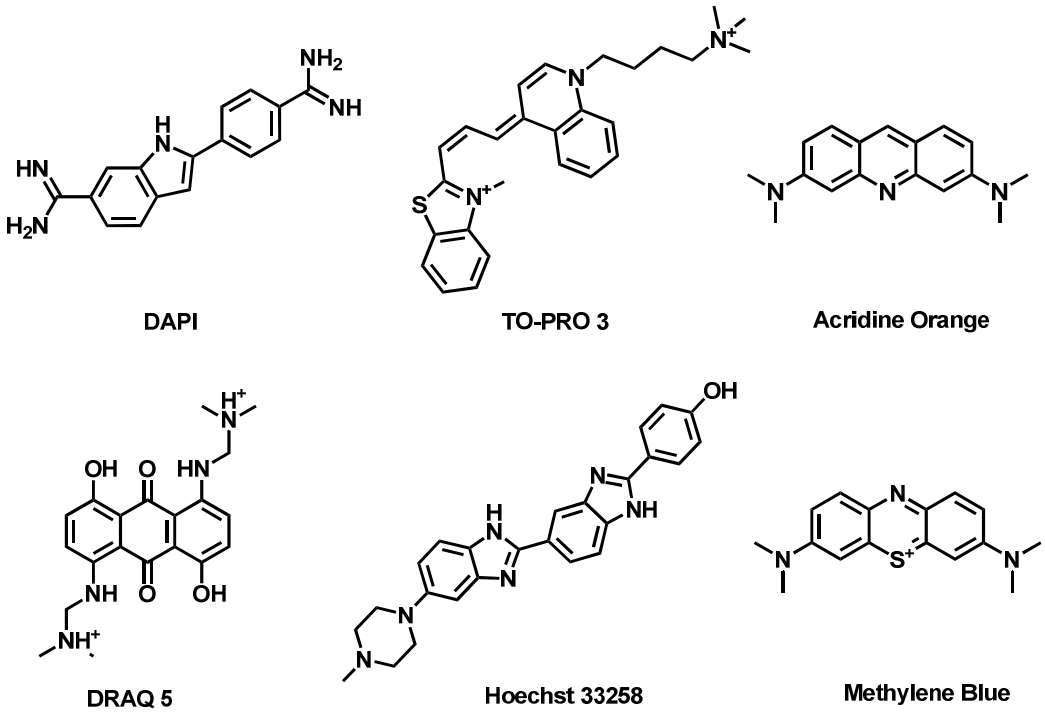

Figure 5.2. Structures of the six binding agents used in this study.

Table 5.1. Properties of the six DNA binding agents used in this study.

Binding Agent	Molecular Weight / g mol^{-1}	Mode of Binding	Excitation λ / nm	Emission λ / nm
Acridine Orange	265.35	Intercalation	502	525
DRAQ 5™	412.54	Intercalation	647	670
Hoechst 33258	533.88	Minor Groove	352	461
DAPI	277.32	Minor Groove	358	461
Methylene Blue	319.85	Multiple*	664	682
To-Pro 3®	671.42	Multiple†	642	661

* Methylene blue binds selectively to dsDNA through both a minor-groove interaction and intercalation.
† To-Pro 3® also binds strongly to ssDNA in solution. Modes of binding to dsDNA are thought to be intercalation, minor-groove and electrostatic interactions.

5.3. DNA Preparation and Design

Sequences in the gene responsible for coding the Cystic Fibrosis Transmembrane Regulator (CFTR) protein were used as a model system to demonstrate the label-free SERS detection and discrimination of mutations. Sequences from the CFTR gene were chosen because of an existing familiarity with this system[20, 21].

Each dsDNA was composed of a 5' modified probe oligonucleotide and an unmodified target oligonucleotide. The probe sequence, which remained constant in all the experiments, was designed to bind to the gold substrates through three di-thiol phosphoramidites attached to the probe at the 5' end. The structure and attachment of this modification is described in Chapter 2. The complementary target sequence used was either the 'wild type' perfect match, or one of two destabilising mutations; a triplet deletion or a single nucleotide polymorphism (Table 5.3.).

Table 5.3. Sequences of the probe, and target oligonuclotides used in this study. Mutations in the ΔF508 triple deletion and 1653C/T single nucleotide polymorphism (SNP) oligonucleotides are highlighted in bold.

Probe	HXHXHX-5'	AGGAAACACCAAAGATGATATT	3'
Wild type	3'	TCCTTTGTGGTTTCTACTATAA	5'
ΔF508 Deletion	3'	TCCTTTGTGGTTT**T**TACTATAA	3'
1653C/T SNP	3'	TCCTTTGTGG**- - -** CTACTATAA	3'

5.4. Label Free Detection of DNA

5.4.1. Detection of dsDNA at an SSV Surface

Sphere segment void substrates with immobilised dsDNA were prepared as described in Chapter 2. Following hybridisation of the target strand, substrates were exposed to a 1mM solution of the chosen DNA binding agent for three hours. Substrates were then rinsed thoroughly with a 10 mM Tris buffer solution (pH 7.2) containing 1 M NaCl before measurement.

It was possible to detect dsDNA immobilised at an SSV substrate with five of the six binding agents studied. The SER(R)S spectra of Hoechst 33258, DAPI, methylene blue, and To-PRO® in the presence of surface immobilised single-stranded and double-stranded DNA are shown in Figure 5.3.

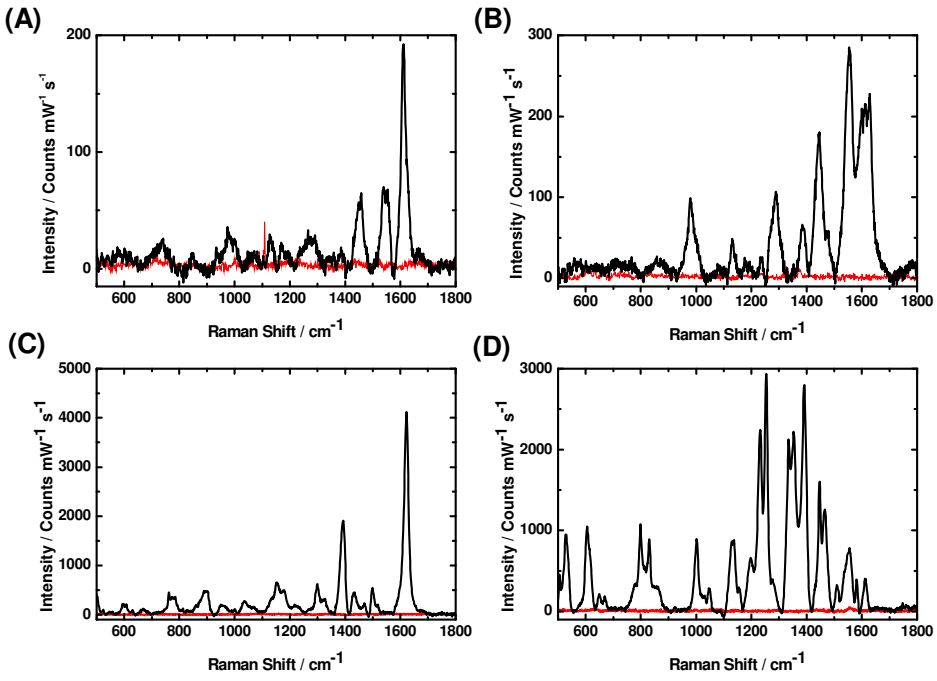

Figure 5.3. SERS spectra of (A) DAPI (B) Hoechst 33258, (C) methylene blue and (D) To-Pro® 3 in the presence of surface immobilised single-stranded (red line) and double-stranded (black line) DNA. Spectra were collected in extended mode using 2 averaged acquisitions. Collection times have been normalised and spectra have been background subtracted for clarity and ease of comparison.

DAPI, Hoechst 33258, acridine orange, methylene blue and To-Pro® 3 were found to be selective for dsDNA in our detection assay. Whilst these molecules are often used in ssDNA staining protocols, the interaction between the binding agent and the ssDNA is typically weak and only electrostatic in nature. Stronger intercalation and groove-binding interactions can only occur in dsDNA. Furthermore, ssDNA immobilised at a surface is significantly less accessible than in solution, particularly at high salt concentrations and at room temperature where it adopts a compressed orientation close to the electrode surface, with little extension out into the solution[22].

Prior to measurement, substrates were rinsed thoroughly in a 10 mM Tris buffer (pH 7.2) containing 1 M NaCl. The large quantity of ions in solution screens the electrostatic interactions between the binding agent and the ssDNA, and molecules bound through just a weak electrostatic interaction are washed away from the surface.

Acquisition of SER spectra at an SSV surface in the presence of the fluorescent label DRAQ-5™ resulted in immediate saturation of the detector during measurement, even when very short acquisition times (< 5 s) and low laser powers (< 1 mW) were used. This suggests that whilst DRAQ 5™ intercalates successfully into surface immobilised dsDNA, the strong florescence of this molecule makes detection with SERS impossible with a 633 nm excitation source.

In Chapter 3, it was demonstrated that the florescent label Texas red covalently attached to target DNA was an effective reporter molecule in a SERS based discrimination assay. However, in this case the label is attached proximal to the surface of the SERS substrate, and the majority of the florescence is quenched. Since the position at which DRAQ-5™ intercalates into the immobilised dsDNA cannot be reliably controlled, the metal-flurophore quenching is not as effective.

The same problem did not occur with Methylene blue or To-PRO®-3, which despite their use as florescent stains produced very intense Raman spectra. The spectra of these two molecules were found to be significantly more intense than those observed for DAPI, Hoechst 33258 or acridine orange due to resonance excitation by the 633 nm laser. This resonance Raman effect gives rise to ~10^3 enhancement, creating a ~ 10^9 enhancement overall when combined with SERS[23].

The minor-groove binders DAPI and Hoechst 33258 have been shown to bind to repeating AT tracks and are highly selective for dsDNA[24, 25]. For the oligonuclotides used in this study, the AT repeat region is at the 3' end of the probe strand and at the 5' of the target strand respectively. In our assay, where the probe strand is attached to the gold substrate through a thiol anchor at the 5' end, it is reasonable to assume that these binding agents are held in the minor groove approximately 20 base pairs (9 nm) from the surface. Previously, we have shown that the surface coverage of these

oligonucleotides immobilised at an SSV surface is roughly 1×10^{12} molecules cm^{-2}, and assuming that one molecule of DAPI or Hoechst binds to each dsDNA molecule, the SERS spectra were collected from approximately 12,500 molecules.

This demonstrates the outstanding capabilities of the sphere segment void substrate, where it is possible to detect molecules at the atto-mole level even when the conditions are highly unfavourable. In this case, the molecule to be detected is not resonant with the excitation source and is far from the metal-dielectric boundary where the enhancing surface plasmons modes are most intense.

The detection of multiple binding agents also highlights the flexibility of our label-free SERS detection assay. Whilst resonant methylene blue and To-Pro® 3 proved the best choice for use as reporter molecules with the 633 nm excitation laser used in our study, it should be possible to obtain the resonant SERS effect from other DNA binding agents by utilising another excitation wavelength. For example, Hoesct 33258 and DAPI would be resonant with a UV (363 nm) laser. A more practical example is the nucleic acid stain To-Pro® 5, which is similar in structure to the To-Pro® 3 used in this study. To-Pro® 5 has excitation and emission maxima of 745 nm and 770 nm respectively, and is resonant with a 785 nm (diode) laser. These types of laser are portable, low cost and can easily be integrated into small point-of-care devices.

5.4.2. Peak Assignments and Binding Orientation

The SERRS spectra of methylene blue, Hoechst 33258 and DAPI were in good agreement with those reported previously, and peaks were assigned based on the literature values available for these molecules (table 5.3.). The SERS spectrum of To-PRO® has not previously been reported, but shows characteristics that are typical of cyanine dyes. Some of the major peaks for this molecule have been tentatively assigned based on literature values for cyanine dyes.

Table 5.3. Major peak assignments for the DNA binding agents methylene blue, DAPI, Hoechst 33258 and To-Pro® 3.

Molecule	λ / cm^{-1}	Assignment	Reference
Methylene Blue‡	1622	C=N stretch	
	1432	CH_3 stretch	26-29
	1388	C=C ring stretch	26-29
	902	C= C Ring stretch	26-29
	480	C-S stretch	26-29
DAPI§	1612	C=N stretch	30
	1540	C=C stretch, C=N stretch	
	1459	CH_3 stretch	
	979	C-C ring deformation, C-N ring deformation	
Hoechst	1628	C=N stretch, C=C stretch	31
	1553	C=N stretch, C=C stretch	31
	1445	Skeletal ring in-plane bend	31
	1290	C-H deformation	31
	979	C-C ring deformation, C-N ring deformation	31
To-Pro 3®	1556	Chromophore C=N stretch	23, 32-34
	1448	-CH asymmetric deformation, chromophore ring stretch	23, 32-34
	1393	C=C chromophore ring stretch	23, 32-34
	1254	Aromatic CH in-plane bend	23, 32-34
	1138	CH_3-CH-CH_3 skeletal stretch	23, 32-34
	1002	Chromophore aromatic C-C	23, 32-34
	531	Methine chain stretch	23, 32-34

‡ The peak at 1622 cm^{-1} is typically assigned to a C=C ring stretch in literature reports[26-29]. However, the results presented in Figure 5.7 suggest that a C=N ring stretch is a more suitable assignment.
§ These peaks were assigned based on similarities between the spectra of DAPI and Hoechst 33258.

The spectrum of acridine orange bound to dsDNA immobilised DNA was not in agreement with previously reported SERS studies of this molecule[35], as only some of the expected peaks were present. This can be explained by considering the Raman surface selection rule[18, 19], and the orientation of the acridine orange with respect to the SSV surface.

The Raman surface selection rule states that those bands in the spectra that are most intense will be associated with a vibrational mode that has a polarisability tensor in a direction perpendicular to the surface[18, 19]. Weaker contributions to the spectra will come from vibrational modes that have a polarisability tensor parallel to the surface.

Since the binding mechanism of acridine orange to dsDNA is exclusively intercalation[36, 37], in our assay the molecule will lie in a position parallel to the SSV surface. In this orientation, the vibrational modes with large polarisability components perpendicular to the surface will typically be deformations of the methyl groups that lie out-of-plane with the aromatic ring.

Conversely, when acridine orange is perpendicular to the SERS surface, as described in the study by Zimmermann *et al.*[35], the vibrational modes with large polarisability components perpendicular to the surface will be stretches of the aromatic ring.

The orientation of acridine orange with respect to the surface was confirmed by a further experiment. A 1 mM acridine orange solution was dropped onto an SSV substrate and permitted to dry, providing an ensemble of random molecular orientations at the surface. The SERS spectrum of dsDNA bound acridine orange (in a fixed orientation) was compared with the SERS spectrum of acridine orange in random orientations (Figure 5.4.).

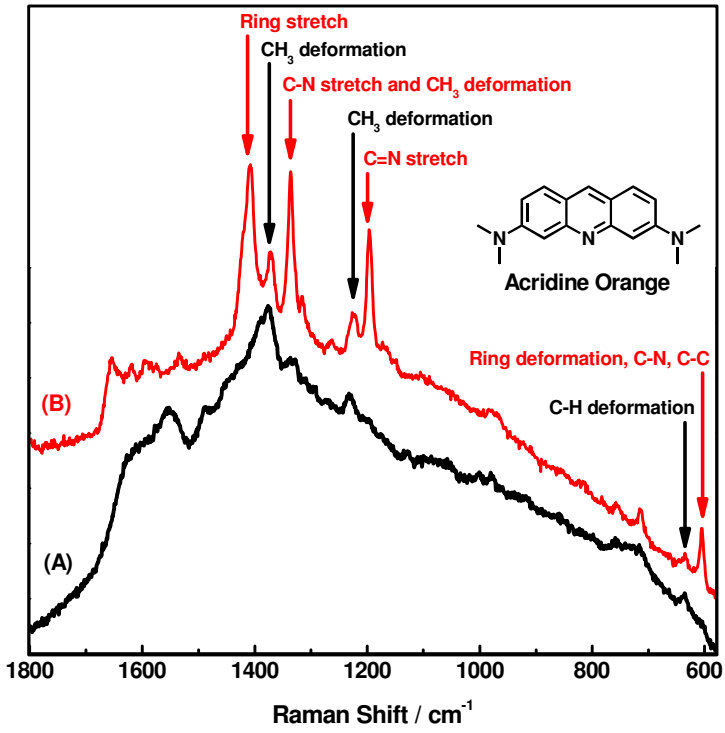

Figure 5.4. SERS Spectra of acridine orange (A, black line) bound to dsDNA and held in a fixed orientation parallel to an SSV surface and (B, red line) in an ensemble of orientations at an SSV surface. Spectra were collected with (A) 2 x 45s and (B) 1 x 10s acquisition, and are presented without further correction for clarity. Peaks assignments are based on those reported by Zimmerman *et al.*[35]

Table 5.4. Major peak assignments for the DNA intercalator acridine orange, based on those reported by Zimmerman *et al.*[35]

λ / cm^{-1}	**Assignment**
1655	Ring stretch
1409	C-C Ring stretch
1373	CH_3 deformation
1336	C-N stretch and CH_3 deformation
1227	CH_3 deformation
1196	C=N stretch
635	C-H deformation
603	C-N ring deformation, C-C ring deformation

The spectrum of acridine orange in an ensemble of orientations was in good agreement with previous literature reports. Peaks in the spectra of acridine orange were assigned based on a very detailed SERS study by Zimmerman *et al.*[35] Comparison of the two spectra in Figure 5.4 gives direct spectroscopic for the Raman surface selection rule, and highlights how SERS can be used to determine the mechanism and orientation to which molecules bind to dsDNA. From this result it can be deduced that acridine orange binds to dsDNA exclusively through intercalation, which is consistent with literature reports[36, 37].

The spectra of the other binding agents studied (Hoescht 33258, DAPI, methylene blue and To-Pro®) were found to be similar regardless of whether the binding agent was an ensemble of random molecular orientations at the surface or bound to surface immobilised dsDNA (Figure 5.5). Whilst some of the molecules may be bound to the dsDNA by intercalation, this result suggests that the majority are bound to dsDNA through minor-groove and/or electrostatic interactions. This is consistent with reported binding mechanisms for the Hoechst 33258, DAPI, and To-Pro® 3 stains. The exact mode of MB binding to dsDNA has been the subject of extensive research, particularly in computational simulations[28, 37-39]. For AT rich sequences, minor groove binding is believed to be favoured over intercalation[38]. In the case of the sequences used in this study, the AT content is >70 %, and it can be assumed that the majority of the methylene blue is bound via a minor groove interaction in the surface immobilised dsDNA used in this study.

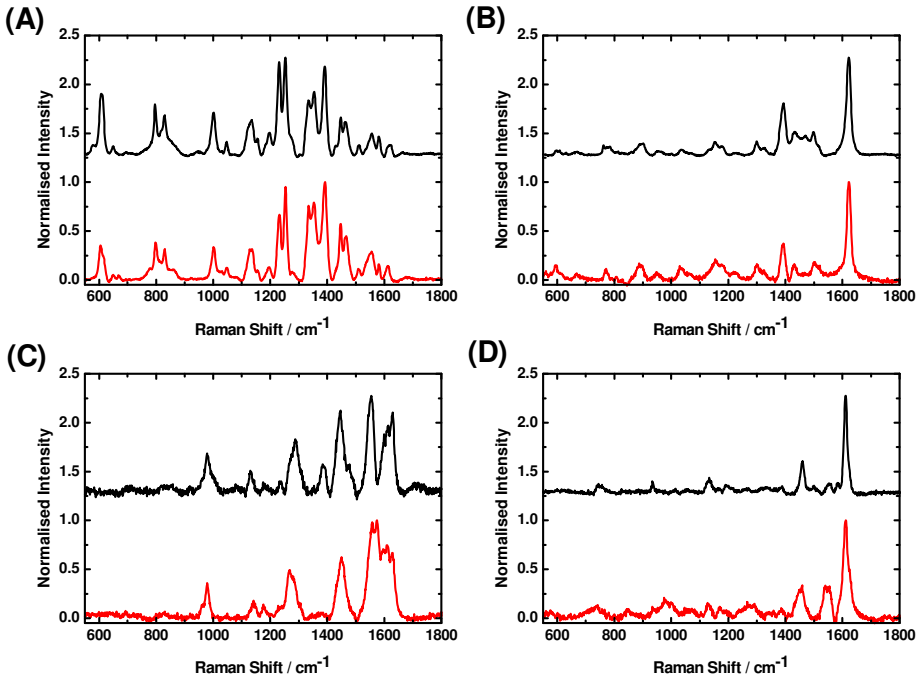

Figure 5.5. SERS of (A) To-PRO3 (B) methylene blue (C) Hoesct 33258, and (D) DAPI bound to dsDNA at an SSV surface and (black line) and in an ensemble of orientations at an SSV surface (red line). Spectra were collected from a single acquisition in extended mode, and have been background corrected and normalised to maximum.

5.5. Thermally Driven DNA Melting

5.5.1. Methylene Blue

Methylene blue is a relatively non-toxic dsDNA binding agent that is resonant with a 633 nm excitation and as such made an ideal candidate for initial label free SERS melting experiments. Upon heating, dsDNA denaturation occurs, and this is monitored via the methylene blue peaks at 1621 cm^{-1} and 1388 cm^{-1}, which are assigned as the C=N and C=C aromatic ring stretches respectively.

Representative SERS spectra and thermal melting curves for three dsDNA strands from the CTFR gene are shown in Figure 5.6. The perfectly complementary 'wild-type' sequence has the highest thermal stability, whilst the single nucleotide polymorphism and triplet deletion have lower but similar thermal stabilities. The results are in general agreement with our previous SERS melting studies in which the target molecule was labelled covalently with Texas Red and solution based thermal melting, although the melting temperatures obtained here are lower than in both of those cases[21]. The increase in stability of a duplex upon covalently attaching a label is well documented, whilst the lower melting temperatures observed for surface bound duplexes has been observed by a number of researchers, and is generally attributed to repulsive charge effects due to the density of the immobilized probes at the substrate surface[40].

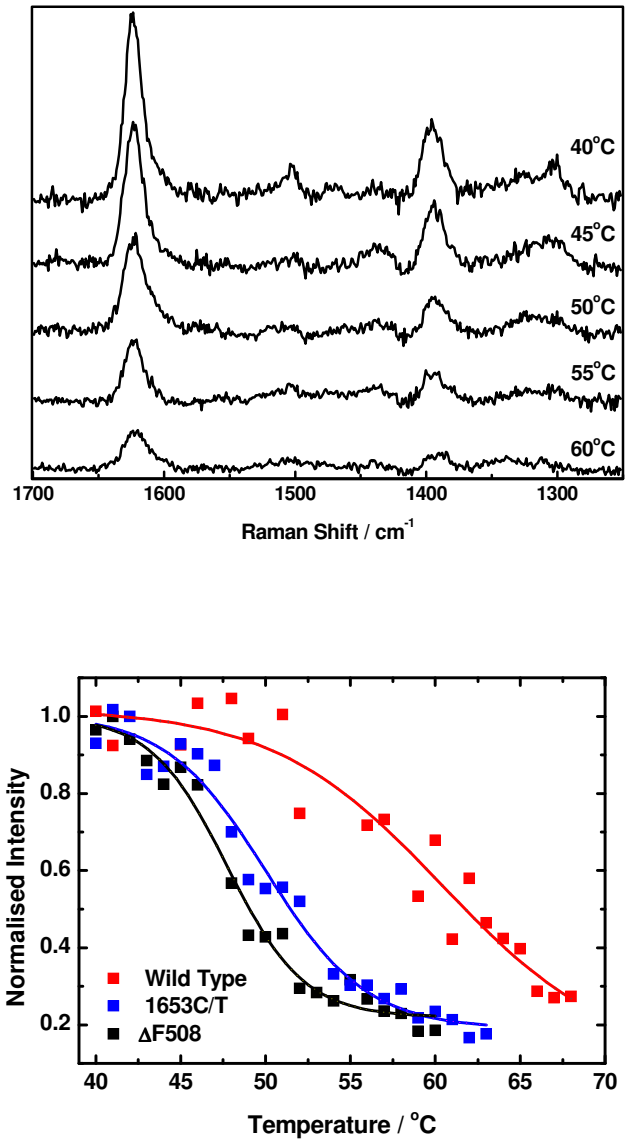

Figure 5.6. (a) Representative SERS spectra and (b) melting curves illustrating discrimination of a wild-type, single nucleotide polymorphism and triplet deletion in the CTFR gene with label free thermal melting carried out in the presence of a 10 mM phosphate buffer (pH 8.1) with 1 M NaCl at a ramp rate of 0.5 °C per minute.

5.6 Electrochemically Driven Melting

5.6.1. The Electrochemistry of Methylene Blue

As well as use for monitoring during thermal denaturation, it was envisaged that methylene blue could be used to monitor electrochemical denaturation as the surface potential is driven negative. However, its use is complicated as MB is readily reduced at negative potentials to its colourless leuco form (LMB), which is not resonant with the 633 nm excitation wavelength and has a slightly different structure. Using SER(R)S it is possible to monitor the reduction and oxidation of methylene blue whilst bound to the minor groove of the dsDNA. SERRS can effectively be turned on or off by switching the molecule between its resonant and non-resonant forms (Figure 5.7).

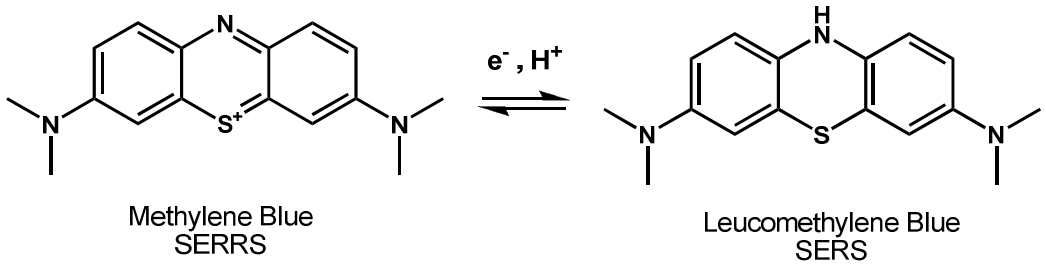

Figure 5.7. Diagram illustrating the structural changes that occur when methylene blue is electrochemically reduced to leuco-methylene blue.

The transformation of MB to LMB can be observed from the peaks at 1621 cm^{-1} and 1388 cm^{-1}, which are assigned as the C=N and C=C aromatic ring stretches respectively. As the MB is gradually reduced, both the 1621 cm^{-1} and 1388 cm^{-1} drop rapidly in intensity due to the loss of resonance with the excitation wavelength. Eventually, the 1621 cm^{-1} peak is lost completely due to the destruction of the C=N bond whilst the 1388 cm^{-1} remains. Upon reversing the potential, the C=N band re-appears and overall the intensity of the spectra increase as the leuco-methylene blue is oxidised back to methylene blue and the resonance of the molecule with the excitation wavelength is restored (Figure 5.8).

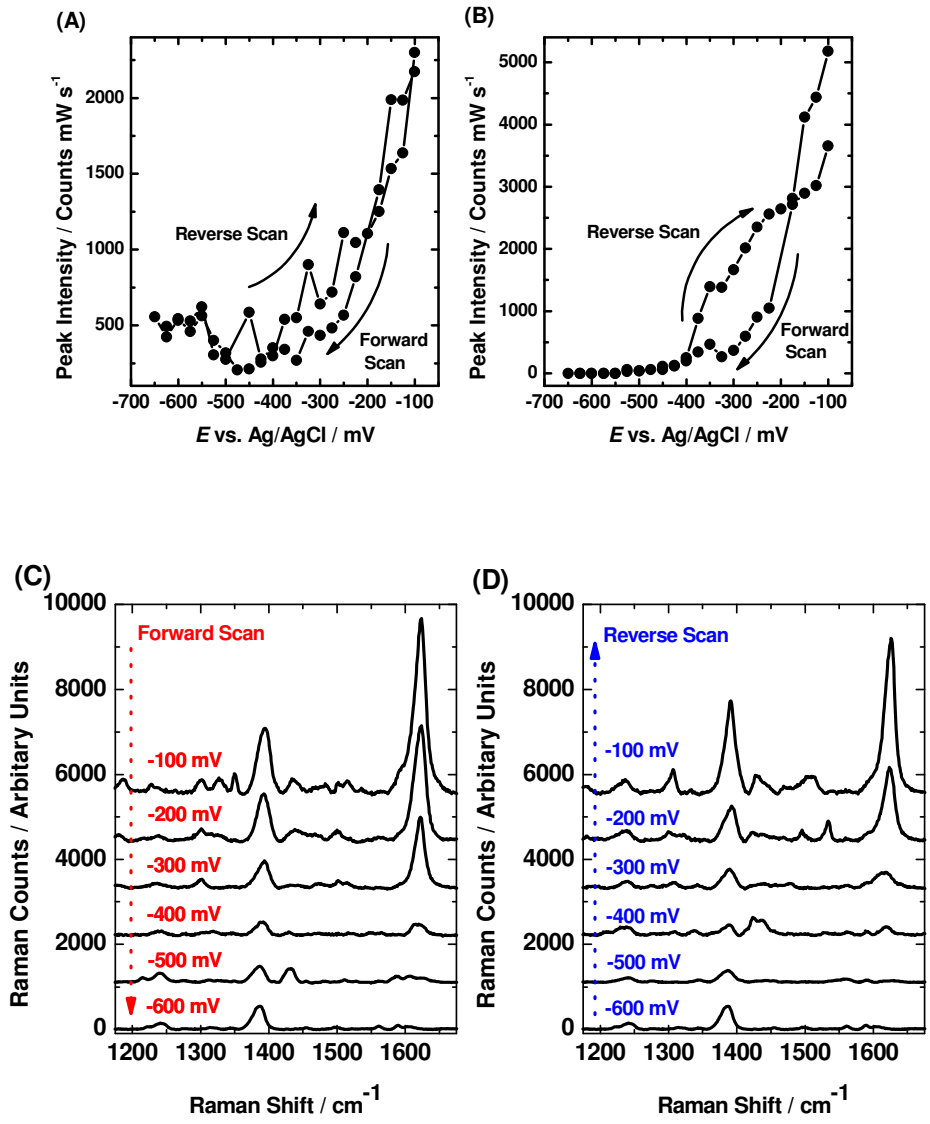

Figure 5.8. Changes in the peak height of (A) the C=C stretch at 1580 cm^{-1} and (B) C=N stretch at 1622 cm^{-1} as a function of applied potential; and representative spectra illustrating this change during the (C) forward and (D) reverse scan of a cyclic voltammetry experiment in which methylene blue was bound to the minor grove of surface immobilised dsDNA. The potential at the electrode surface was swept at 0.5 mV s^{-1} between -0.1 and -0.65 V in a 10 mM Tris buffer (pH 7.2) containing 1 M NaCl.

5.6.2. Discrimination of Mutations with Leuco-Methylene Blue

Whilst no longer resonant with the 633 nm excitation source, dsDNA bound leuco-methylene blue could still be detected with SERS and therefore used as a reporter molecule in a label-free SERS assay.

The peak intensities of the bands at 1388, 1450, 1584 and 1641 cm^{-1} for the methylene blue/leuco-methylene blue were monitored as a function of applied potential during an electrochemical melting experiment in which the potential was swept between -100 and -1400 mV vs. Ag/AgCl (Figure 5.9).

When the methylene blue is reduced to leuco-methylene blue, the 1641 cm^{-1} band no longer appears in the SERS spectrum. As the C=N band attenuates, it is replaced by a weak band at 1584 cm^{-1} which is tentatively assigned as the C-N-C stretch of leuco-methylene blue. The most intense band in leuco-methylene blue is the C=C ring stretch. After the initial loss of intensity caused by the reduction of methylene blue, the peak intensity of the C=C band begins to increase again. This increase occurs when the potential is scanned cathodic between -800 and -1000 mV. This intensity increase has been observed previously in electrochemical melting assays where the labels Texas Red[20, 21, 41] and anthraquinone[20, 42] were covalently bound to the DNA. A similar trend is seen in the intensity of the 1450 cm^{-1} band attributed to the CH_3 deformation. However, in comparison to the C=C band, the peak is significantly less intense overall and the changes in peak height as a function of potential are less well-defined. Upon driving the potential cathodic beyond -1000 mV vs. Ag/AgCl, there is an irreversible loss in SERS intensity which can be attributed to the electrochemically driven DNA denaturation.

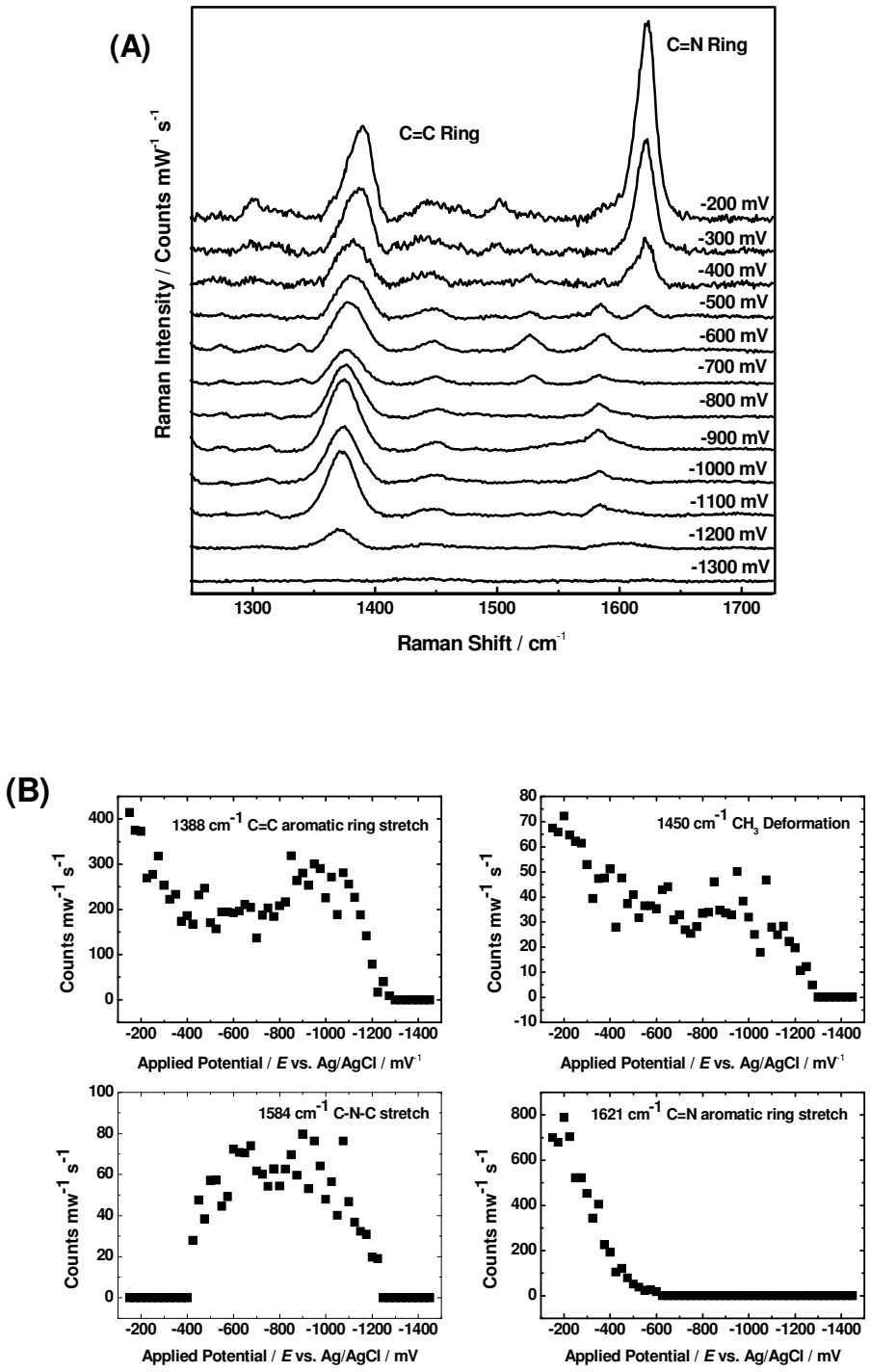

Figure 5.9. (a) Representative SERS spectra and (b) changes in peak height as a function of applied potential illustrating electrochemical reduction of dsDNA bound methylene blue and subsequent electrochemical melting. The potential was swept a scan rate of 0.05 mV s^{-1} in a 10 mM Tris Buffer (pH 7.2) with 1 M NaCl. Spectra were acquired with a 2.7 mW 633 nm excitation laser, and have been background subtracted and normalised with respect to laser power and accumulation time.

Changes in the C=C stretch of methylene blue as a function of applied potential were utilised to monitor electrochemically driven DNA denaturation of mutations in the CTFR gene (Figure 5.10.) The results highlight that a single nucleotide polymorphism and a triplet deletion can be clearly distinguished from a fully complementary sequence in a label-free electrochemical melting experiment in which leuco-methylene blue is used as the reporter molecule.

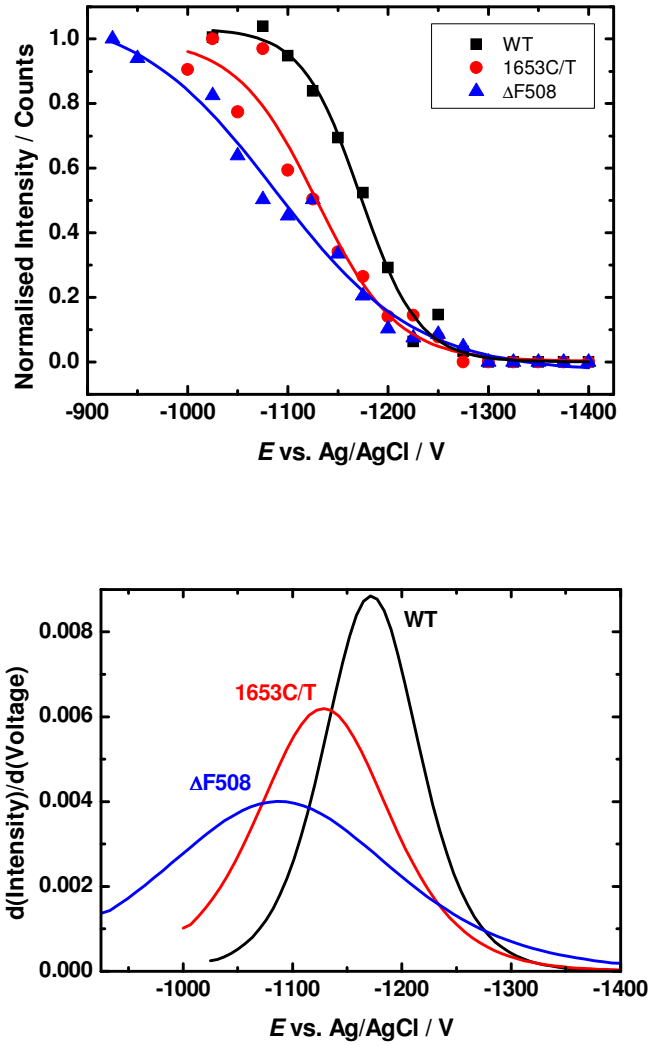

Figure 5.10. Discrimination of mutations in the CTFR gene utilising label-free *E*-melting. (A) The variation of the peak intensity at 1388 cm^{-1} as a function of applied potential. In each case the potential was swept at 0.5 mV s^{-1} from an initial potential of -0.3 V in pH 8.1 10 mM phosphate buffer containing 0.1 M NaCl. Spectra were acquired every 25 mV in static mode with a single 10 s acquisition. (B) First derivative plots indicative of melting potential based upon fitting a Boltzmann curve to the data set for each oligonucleotide.

5.6.3. Discrimination of Mutations with To-PRO® 3

Electrochemical melting experiments were carried out with the DNA binding agent To-PRO® 3. Despite the appearance of a number of waves in the linear sweep voltammeterry upon driving the potential cathodic (Figure 5.11), there were no notable changes to the SERS spectra before the dsDNA began to denature. Whilst the voltametry suggests that the molecule undergoes electrochemically induced changes whilst bound to dsDNA, this did not affect the appearance of the SERS, the resonance of the molecule or its ability to remain bound to dsDNA.

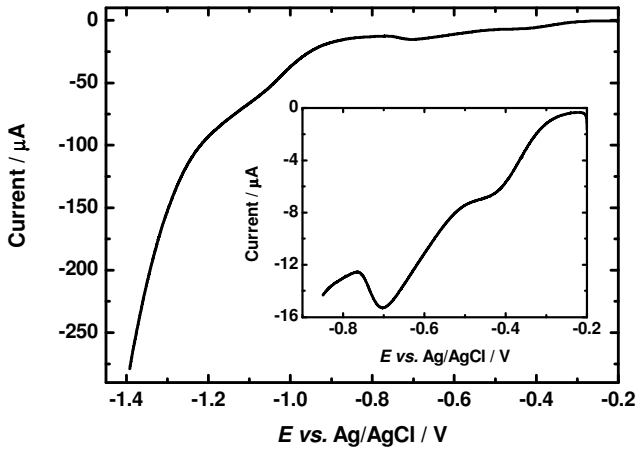

Figure 5.11. Linear sweep voltamagram recorded during the electrochemical melting of dsDNA in the presence of bound To-Pro® 3. The potential was driven cathodic from an initial potential of -0.3 V at 1 mV s^{-1} in pH a 10 mM Tris buffer (pH 7.2) containing 1 M NaCl. The approximate surface area of the electrode was 0.25 cm^{-2}.

The stability and high intensity of the signal from the To-Pro 3 dye makes it very attractive as a choice of binding agent for a label-free electrochemical melting assay. The SERS spectrum contains a large number of peaks, any of which are suitable for following the electrochemical denaturation of DNA upon applying a negative potential (Figure 5.12). However, care must be taken to ensure that the same peak is used when constructing melting curves for different dsDNA samples. This is because the melting potential obtained will differ depending on which peak height is monitored.

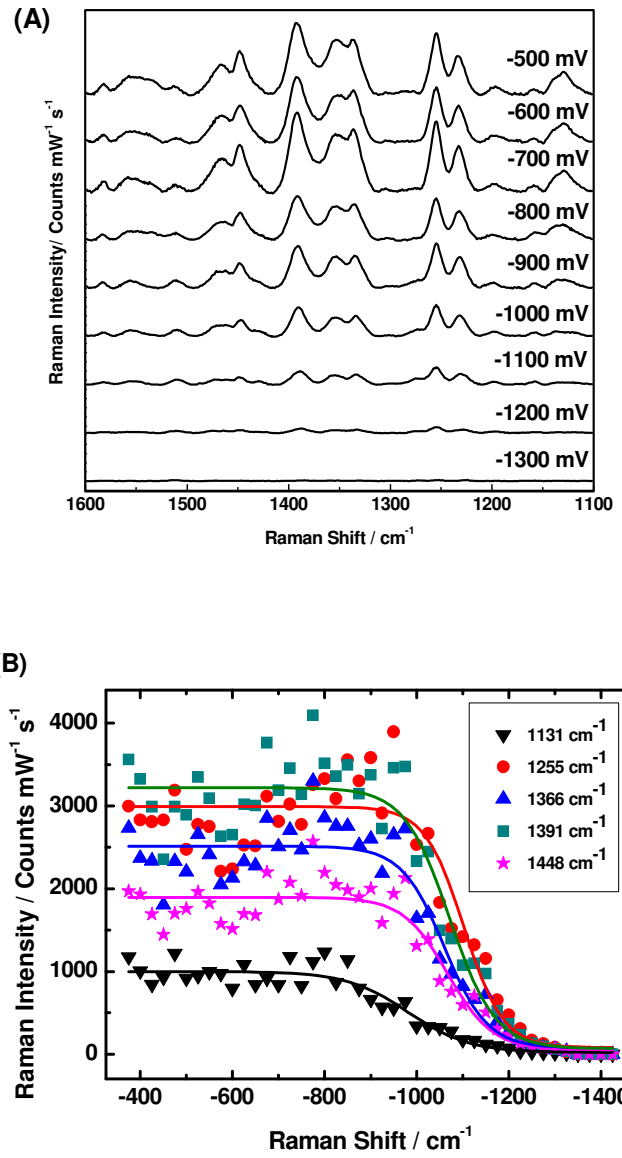

Figure 5.12. (A) Representative SERS spectra and (B) melting profiles demonstrating the change in selected peak heights of dsDNA bound To-Pro™ as the potential is driven cathodic from an initial potential of -0.3 V at 1 mV s^{-1} in pH a 10 mM Tris buffer (pH 7.2) containing 1 M NaCl.

To-PRO 3 was utilised to discriminate between a wild type, single nucleotide polymorphism and a triplet deletion in the CTFR gene (Figure 5.13) As observed for methylene blue, the perfectly complementary 'wild-type' sequence has the most cathodic melting potential, followed by the single nucleotide polymorphism and the least stable triplet deletion.

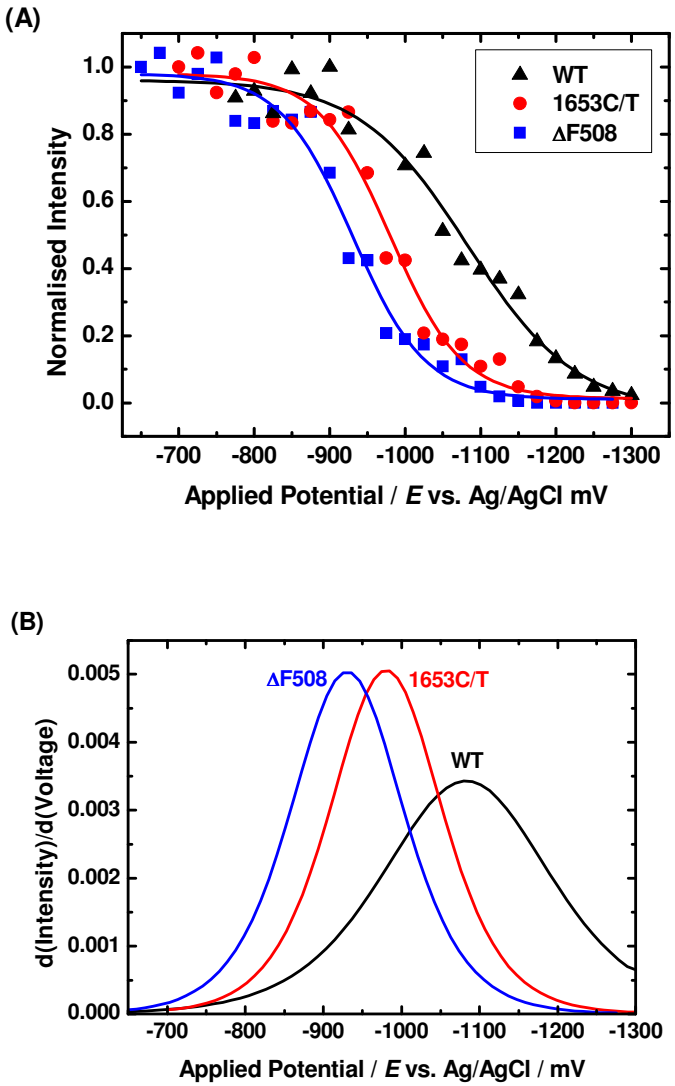

Figure 5.13. Discrimination of mutations in the CTFR gene utilising To-Pro® 3 in a label-free *E*-melting assay. (A) The variation of the peak intensity at 1255 cm^{-1} as a function of applied potential. In each case the potential was swept at 1 mV s^{-1} from an initial potential of -0.3 V in pH a 10 mM Tris buffer (pH 7.2) containing 1 M NaCl. Spectra were acquired every 25 mV in static mode with a single 5 s acquisition. (B) First derivative plots indicative of melting potential based upon fitting a Boltzmann curve to the data set for each oligonucleotide.

5.7. Summary

DNA binding agents have been used to discriminate between single and double stranded DNA immobilized at an SSV surface. The orientation of the binding agent with respect to the DNA base-pairs can be deduced from the peaks that appear in the SERS spectra and applying the Raman surface selection rule[18, 19].

The discrimination of mutations in the CTFR gene without the need to synthetically attach a label dye to the target strand has been demonstrated. SER(R)S is used to monitor DNA denaturation from the spectra of dsDNA binding agents, where the driving force used for the denaturation can be either thermal or electrochemical. The general applicability of the label-free SERS discrimination assay is explored by demonstrating that five different binding agents can be detected when bound to dsDNA at an SSV surface.

The correct choice of binding agent is critical to the success of a label free SERS discrimination assay, particularly because it is not possible to control the position of the reporter molecule such that it is in close proximity to the surface. Factors such as resonance with the pump laser, orientation relative to the electrode surface and toxicity must all be considered.

5.8. References

1. A. Star, E. Tu, J. Niemann, J.-C. P. Gabriel, C. S. Joiner and C. Valcke, *Proc. Nat. Acad. Sci.*, 2006, **103**, 921-926.
2. S. Sorgenfrei, C.-y. Chiu, R. L. Gonzalez, Y.-J. Yu, P. Kim, C. Nuckolls and K. L. Shepard, *Nat Nano*, 2011, **6**, 126-132.
3. U. Rant, K. Arinaga, S. Scherer, E. Pringsheim, S. Fujita, N. Yokoyama, M. Tornow and G. Abstreiter, *Proc. Nat Acad. Sci.*, 2007, **104**, 17364-17369.
4. R. McKendry, J. Zhang, Y. Arntz, T. Strunz, M. Hegner, H. P. Lang, M. K. Baller, U. Certa, E. Meyer, H.-J. Güntherodt and C. Gerber, *Proc. Nat. Acad. Sci.*, 2002, **99**, 9783-9788.
5. X. Yao, X. Li, F. Toledo, C. Zurita-Lopez, M. Gutova, J. Momand and F. Zhou, *Anal. Biochem.*, 2006, **354**, 220-228.
6. Q. Luan, Y. Xue and X. Yao, *Sensors and Actuators B: Chemical*, 2010, **147**, 561-565.
7. C. Fan, K. W. Plaxco and A. J. Heeger, *Proc. Nat Acad. Sci.*, 2003, **100**, 9134-9137.
8. T. Uzawa, R. R. Cheng, R. J. White, D. E. Makarov and K. W. Plaxco, *J. Am. Chem. Soc.*, 2010, **132**, 16120-16126.
9. F. Xia, R. J. White, X. Zuo, A. Patterson, Y. Xiao, D. Kang, X. Gong, K. W. Plaxco and A. J. Heeger, *J. Am. Chem. Soc.*, 2010, **132**, 14346-14348.
10. F. Xia, X. Zuo, R. Yang, R. J. White, Y. Xiao, D. Kang, X. Gong, A. A. Lubin, A. Vallée-Bélisle, J. D. Yuen, B. Y. B. Hsu and K. W. Plaxco, *J. Am. Chem. Soc.*, 2010, **132**, 8557-8559.
11. A. A. Lubin and K. W. Plaxco, *Acc. Chem. Res.*, 2010, **43**, 496-505.
12. S. D. Keighley, P. Estrela, P. Li and P. Migliorato, *Biosens. Bioelectron.*, 2008, **24**, 906-911.
13. A. Li, F. Yang, Y. Ma and X. Yang, *Biosens. Bioelectron.*, 2007, **22**, 1716-1722.
14. J. Kafka, O. Pänke, B. Abendroth and F. Lisdat, *Electrochim. Acta*, 2008, **53**, 7467-7474.
15. A. Barhoumi and N. J. Halas, *J. Am. Chem. Soc.*, 2010, **132**, 12792-12793.
16. A. Barhoumi, D. Zhang, F. Tam and N. J. Halas, *J. Am. Chem. Soc.*, 2008, **130**, 5523-5529.
17. E. Papadopoulou and S. E. J. Bell, *Angew. Chem. Int. Ed.*, 2011, n/a-n/a.
18. X. Gao, J. P. Davies and M. J. Weaver, *J. Phys. Chem.*, 1990, **94**, 6858-6864.
19. M. Moskovits and J. S. Suh, *J. Phys. Chem.*, 1984, **88**, 5526-5530.
20. S. Mahajan, PhD Thesis, University of Southampton, Southampton, 2008.
21. S. Mahajan, J. Richardson, T. Brown and P. N. Bartlett, *J. Am. Chem. Soc.*, 2008, **130**, 15589-15601.
22. W. Kaiser and U. Rant, *J. Am. Chem. Soc.*, 2010, **132**, 7935-7945.
23. S. Mahajan, J. J. Baumberg, A. E. Russell and P. N. Bartlett, *Phys. Chem. Chem. Phys.*, 2007, **9**, 6016-6020.
24. D. E. Gilbert and J. Feigon, *Current Opinion in Structural Biology*, 1991, **1**, 439-445.
25. S. Neidle, L. H. Pearl and J. V. Skelly, *Biochem. J.*, 1987, **243**, 1 -13.
26. W.-X. Chen, H. Jiang, Z.-D. Xu and Y. Lu, *Chin. J. Chem* . 1999, **17**, 125-131.
27. R. R. Naujok, R. V. Duevel and R. M. Corn, *Langmuir*, 1993, **9**, 1771-1774.

28. S. H. A. Nicolai and J. C. Rubim, *Langmuir*, 2003, **19**, 4291-4294.
29. G.-N. Xiao and S.-Q. Man, *Chem. Phys. Lett.*, 2007, **447**, 305-309.
30. X. Dou, T. Takama, Y. Yamaguchi, K. Hirai, H. Yamamoto, S. Doi and Y. Ozaki, *Appl. Opt.*, 1998, **37**, 759-763.
31. F. Zimmermann, B. Zimmermann, J. C. Panitz and A. Wokaun, *J. Raman. Spec.*, 1995, **26**, 435-441.
32. K. Kneipp, H. Kneipp and M. Rentsch, *J. Mol. Struct.*, 1987, **156**, 331-340.
33. H. Sato, M. Kawasaki, K. Kasatani and M.-a. Katsumata, *J. Raman. Spec.*, 1988, **19**, 129-132.
34. X. Wang, H. Wen, T. He, J. Zuo, C. Xu and F.-C. Liu, *Spectrochimica Acta Part A: Molecular and Biomolecular Spectroscopy*, 1997, **53**, 2495-2504.
35. F. Zimmerman, B. Hossenfelder, J. C. Panitz and A. Wokaun, *J. Phys. Chem.*, 1994, **98**, 12796-12804.
36. M. B. Lyles and I. L. Cameron, *Biophys. Chem.*, 2002, **96**, 53-76.
37. S. Nafisi, A. A. Saboury, N. Keramat, J.-F. Neault and H.-A. Tajmir-Riahi, *J. Mol. Struct.*, 2007, **827**, 35-43.
38. R. Rohs, I. Bloch, H. Sklenar and Z. Shakked, *Nucleic Acids Res.*, 2005, **33**, 7048-7057.
39. E. Tuite and B. Norden, *J. Am. Chem. Soc.*, 1994, **116**, 7548-7556.
40. H. Nasef, V. Beni and C. K. O'Sullivan, *Electrochem. Commun.*, 2010, **12**, 1030-1033.
41. D. K. Corrigan, N. Gale, T. Brown and P. N. Bartlett, *Angew. Chem.*, 2010, **122**, 6053-6056.
42. S. Mahajan, J. Richardson, N. B. Gaied, Z. Zhao, T. Brown and P. N. Bartlett, *Electroanalysis*, 2009, **21**, 2190-2197.

6. Conclusions & Further Work

6.1. Overview

The application of a negative potential at an electrode surface can be utilised to denature a nucleic acid helix (either DNA or PNA) into its constituent strands. Whilst one of these strands remains covalently attached to the surface ('the probe'), the other strand ('the target') diffuses away from the surface and into the bulk solution.

The denaturation process is monitored with surface enhanced Raman spectroscopy (SERS), where the signal of a reporter molecule attenuates as the number of target molecules at the surface decreases. The resistance of an immobilised helix to electrochemical denaturation is described by the melting potential, which is defined as the point at which the signal from the reporter molecule falls to 50 % of its initial value.

In Chapter three, the effect of varying nucleic acid structure on the melting potential was explored. For immobilised dsDNA, the melting potential was found to scale linearly with the calculated and experimental melting temperatures of the same duplex in solution. Further, it was established that immobilised dsPNA could also be electrochemically denatured, ruling out a simple electrostatic repulsion interaction between the dsDNA sugar-phosphate backbone and the electrode surface as the mechanism for electrochemical melting.

In Chapter four, the effects of pH and ionic strength on the melting potential were described. Localised pH changes close to the electrode surface were ruled out as a possible mechanism for electrochemical melting through a series of experiments in which the surface pH and electrochemical denaturation were monitored simultaneously. The effects of ionic strength on electrochemical melting were rationalised through consideration of the structure of the electrical double layer.

In Chapter five, electrochemical melting without the need to attach a dye label to the desired target nucleotide was demonstrated. This presents a significant milestone

towards the development of a point-of-care electrochemical melting assay, because label-free detection methods offer a way of detecting the target nucleotide without the need for synthetic treatment prior to measurement.

In this Chapter, the insights gained into the electrochemical melting mechanism are discussed in greater detail, and a mechanism for the denaturation that fits with the currently available data is proposed. Finally, some future experiments that should help further our understanding of the process are described, along with some ways in which the reliability and commercial viability of the technique can be improved.

6.2. Understanding Electrochemical Melting

6.2.1. Disproved Mechanisms for Electrochemical Melting

During the course of this work, a wide-variety of possible mechanisms for electrochemical melting have been proposed and then later disproved through further experimentation or a more detailed analysis of the available data.

Electrostatic repulsion between the sugar-phosphate backbone of the immobilised dsDNA and the negatively-charged electrode surface received significant consideration as the denaturation mechanism in the early stages of this work. Early melting experiments were generally performed in very low ionic strength buffer (10 mM), so the electric field emanating from the electrode surface was expected to be able to exert an effect on the immobilised duplex. However, later experiments showed that electrochemical denaturation was still possible at very high ionic strengths (1 M) where the majority of the electric field is dropped in less than a nanometre. Under these conditions it is unlikely that the duplex experiences any electric field at all.

Conclusive proof that electrostatic repulsion was not responsible for the denaturation process came through experiments in which PNA was employed as the target strand during an electrochemical melting experiment. PNA is a neutral analogue of DNA that is completely uncharged under physiological pH conditions. Despite this,

denaturation was still possible by applying cathodic potentials of a similar magnitude to those required for immobilised duplexes constructed from DNA.

Localised pH Changes were ruled out as a possible mechanism through a series of experiments in which the pH at the surface of an electrode was monitored simultaneously with electrochemical denaturation. The pH was monitored spectroscopically through the ratio of COO^- and COOH bands of *para*-mercaptobenozic acid. No change in the band ratio was observed as the potential was scanned cathodic.

Chemical or electrochemical damage to the surface immobilised duplex is thought to be a highly unlikely mechanism for electrochemical denaturation. Primarily, this is because the same surfaces (with the same immobilised probe DNA) can be reused multiple times. Any damage to the structure of the helix as a result of chemical or electrochemical damage is unlikely to be confined to the target strand, and if the probe strand were damaged it is unlikely that it could re-hybridise. In addition, analysis of the linear sweep voltammograms recorded during an electrochemical melting experiment show little in the way of redox activity (Figure 6.1). This is consistent with literature reports, where the reduction of DNA bases (specifically cytosine and adenine) has been demonstrated to occur only at cathodic potentials < -1.4 V vs. SCE[1-3]. Electrochemical reduction of the DNA occurs well after melting potential is reached and in most cases is also after the complete separation of the target from the probe.

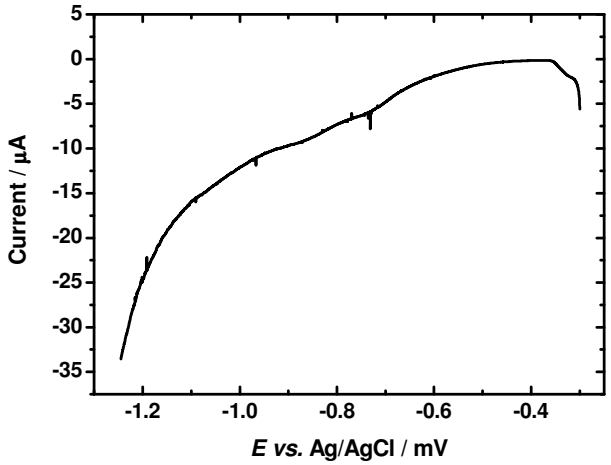

Figure 6.1. Linear sweep voltammogram of Cy3-labelled, surface immobilised dsDNA recorded during an electrochemical melting experiment. The potential was swept from -0.3 to -1.3 V vs. Ag/AgCl at a scan rate of 0.5 mV s^{-1} in a 10mM phosphate buffer (pH 8.1) containing 100 mM NaCl. The approximate surface area of the electrode was 0.25 cm^2. The large increase in current after – 1 V is attributed to oxygen reduction.

Joule Heating was also considered as a possible mechanism for electrochemical melting. Extensive research by Barton and co-workers has demonstrated that dsDNA can act as a molecular wire, where the electrons shuttle through the π-stack of the helix[4-8]. In joule heating, the movement of electrons through a wire generates heat. The magnitude of the heat generated, Q is given by the following expression:

$$Q = I^2 Rt \qquad 6.1$$

Where I is the current flow through a wire, R is the resistance of the wire, and t is the length of time for which the current flows.

Joule heating is an unlikely mechanism for electrochemical melting because the currents generated during an experiment are very small (typically microamperes, Figure 6.1).Very large currents would be required to generate the magnitude of heat required to overcome the hybridisation enthalpy for a duplex.

6.2.2. Current Theory

Based on our current understanding, the following mechanism for electrochemical melting is proposed (Figure 6.2). As the potential of the electrode surface is driven cathodic, electrons are conducted through the base-pairs of the surface immobilised dsDNA. The number of electrons present in the DNA helix at a given moment will be dependent on the applied potential. As the potential is driven to a more negative value, the number of electrons within the DNA helix will increase. In this sense the DNA is acting like a molecular wire, as described by the research of Barton and co-workers[4-8]. However, in an electrochemical melting experiment, the DNA helix is also acting like a capacitor, because there is nowhere for the electrons to go. There is a build-up of charge until at some point the electrostatic interactions between the increasing numbers of electrons becomes too great and the duplex denatures into its constituent strands. The point at which this occurs will depend on the thermodynamic stability of the helix.

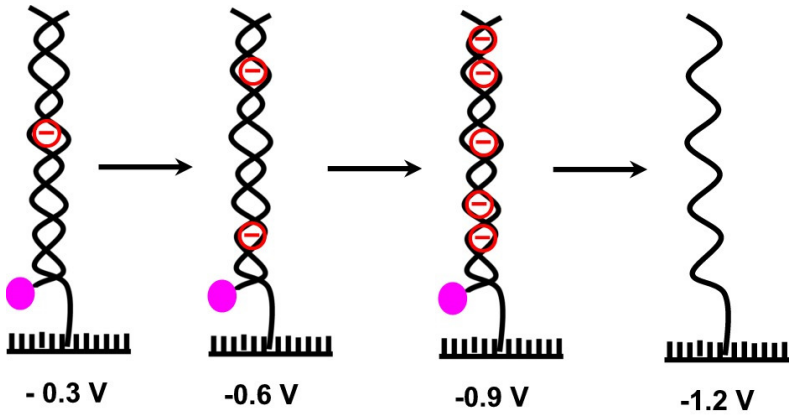

Figure 6.2. Simplified illustration demonstrating the proposed mechanism for electrochemical melting. As the potential is driven cathodic, electrons flow into the immobilised dsDNA π-stack from the electrode surface. At some given potential, the energy generated by the electrostatic forces between the electrons in the π-stack will be greater than the enthalpy of formation for the helix, and denaturation occurs.

This theory explains why there is a strong correlation between melting temperature and melting potential (Chapter 3). Increasing the GC content of the duplex increases its binding enthalpy, meaning that a greater number of electrons must be built up within the duplex before denaturation occurs.

Based on this theory, a number of predictions can be made about the how the electrochemical melting potential will vary when the experimental conditions are changed. Electrochemically induced denaturation is likely to become significantly more difficult if the interactions between the electrons travelling within the π-stack of the helix are screened in some way. This was observed in label-free melting experiments (Chapter 5), where the use of DNA binding agents resulted in a more cathodic melting potential relative to a duplex of the same sequence externally labelled with Texas Red (Figure 6.3).

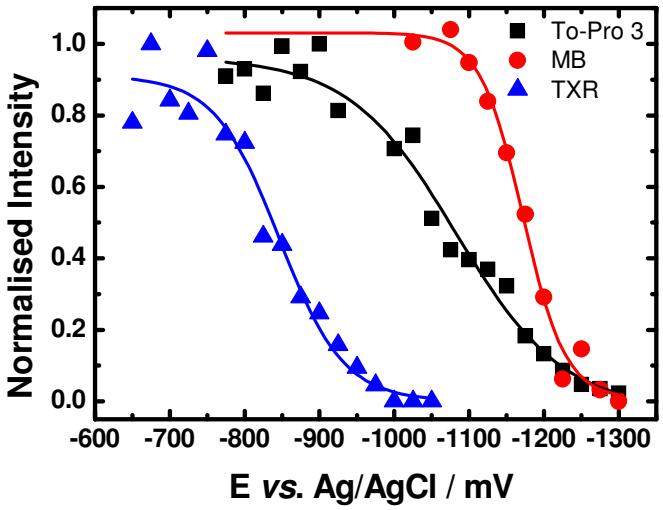

Figure 6.3. Electrochemical melting curves for the wild-type sequence . The reporter molecule utilised for monitoring denaturation was either synthetically attached Texas red (TXR, red circles), or non-covalently bound methylene blue (MB, blue triangles) or To-Pro 3 (black squares). In each instance potential was swept cathodic from -0.3 V vs. Ag/AgCl at 1 mV s^{-1} in 10 mM Tris buffer (pH 7.2) containing 1 M NaCl. Denaturation was monitored through attenuation of the band at 1500 cm^{-1} for Texas red, 1388 cm^{-1} for methylene blue, and 1255 cm^{-1} for To-Pro 3.

This would also explain why the electrochemical melting potential scales with DNA-cation binding affinity (Chapter 4). Those cations that have the highest binding affinity for the duplex are the most effective at screening the interactions between the electrons travelling within the π-stack of the helix.

The concept of dsDNA acting as a molecular wire has been explored in detail by Barton and co-workers[4-8], who have shown that the π-stack of dsDNA is still an effective conductor of electrons even over distance as large as 34 nm[9] – well below the 22 base-pair (~ 9 nm) duplexes used in the electrochemical melting experiments presented in this thesis. Disruption of this electron-conducting π-stack (through mutation or damage of the base-pairs) has been shown to result in a significant drop in current flow[5, 6, 9].

Although the electrochemical denaturation of mutation-containing DNA sequences has been demonstrated to occur at less cathodic potentials (Chapter 5), this can be explained by considering the overall length of strand and the position of the mutation relative to the electrode surface. Consider the 1653C/T sequence utilised for demonstrating the discrimination of mutations in the CTFR gene (Chapter 5). Assuming that electrons can flow up to the point of the base-pair mismatch, the length of the duplex prior to the mutation will denature as the potential is driven negative. The remaining five base-pair sequence (TAC TAT AA) has a nearest-neighbour melting temperature of just 13.6 °C in 1 M NaCl and so will readily denature without any external influence at room temperature.

Perhaps the hardest result to rationalise is the significantly less negative than predicted melting potential of duplexes that contain PNA (Chapter 4). Very few studies of electron transfer through PNA duplexes have been reported[10-12], and differences in the π-stack between DNA and PNA duplexes has not been explored. The higher surface density of probes was given as one possible explanation for the ease of denaturation of PNA-containing duplexes. Another possibility is that electrons residing within the π-stack of PNA are less effectively screened than those residing within the π-stack of DNA due to lower counter-ion uptake.

6.3. Further Work

6.3.1. Understanding Electrochemical Melting

There are number of potential experiments that could be used to test the validity of the mechanism proposed in section 2.3. The build up of electrons within the DNA π-stack requires that an efficient transportation pathway is maintained. Disrupting the pathway should severely inhibit electrochemical melting. One possible method of disrupting the π-stack is through the use of the intercalative agents such as ethidum bromide or acridine orange that will cause a distortion to the duplex.

Introducing base-pair mismatches into a DNA duplex also severely inhibit electron transfer through the π-stack[5, 9]. A long, dual-labelled, target strand could be utilised to validate the proposed mechanism by introducing a mismatch half way up the strand (Figure 6.4). If the proposed mechanism is valid, then, upon scanning cathodic, only the base-pairs before the mutation will denature, and the melting potential will reflect this. Upon scanning anodic, the denatured portion of the duplex should quickly anneal again.

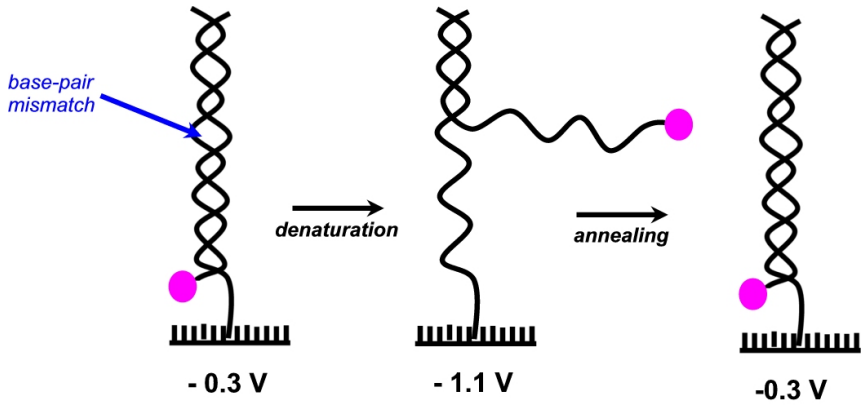

Figure 6.4. The predicted behaviour of surface immobilised dsDNA that contains a mismatch midway into the base-pair sequence. Upon scanning cathodic, charge will build up in the helix up to the point of the mutation and this portion of the strand will denature. Assuming that remaining portion of the strand is stable at room temperature, then upon scanning anodic, charge in the helix will dissipate and the full strand will re-anneal.

Another method for disrupting electron transfer through the π-stack is through the distance of the duplex from the electrode surface. Currently, the thiol anchor group

holds the dsDNA approximately 1 nm from the surface. Increasing the length of this anchor group should result in a reduction in electron transfer rate, resulting in a more stable duplex.

The results presented in Chapter 4 suggest that values for the electrochemical melting potential are strongly related to the structure of the electrical double layer (EDL). Experiments are currently under way to 'map out' the electric fields emanating from an electrode as a function of both ionic strength and distance from the surface. This is accomplished by utilising surface immobilised DNA that is labelled with a nitrile-modified Cy3 label. The Raman shift at which the nitrile peak occurs is dependent on the electric field it experiences, as described by the Stark effect[13-15]. These experiments will be supported by computational modelling of the surface immobilised duplex and the electrical double layer by the research group of Timo Jacob at the University of Ulm.

6.3.2. Improving Electrochemical Melting Assays

There are a number of ways in which the capabilities and performance of electrochemical melting can be improved, the most of obvious of which is to boost the signal intensity from the reporter molecule, which can either be synthetically attached to the target strand or non-covalently bound to the duplex. In addition to increasing sensitivity, an improvement to the signal would allow electrochemical melting experiments to be performed at faster scan rates because lower acquisition times would be required.

There are two main ways in which an improvement in the signal intensity could be achieved, either through improving the performance of the underlying substrate, or through better control of the position and structure of the reporter molecule.

The sphere segment void (SSV) substrates utilised in this work are prepared entirely from gold and provide typical enhancement factors of 10^9 over flat gold. Recent research within our group has demonstrated that this enhancement can be improved further through nanoparticle-void coupling[16, 17]. Thus, it should be possible to improve

the sensitivity of an electrochemical melting assay through the use of nanoparticle labelled target DNA.

It is also possible to obtain more intense and more reproducible SER spectra through better control of the reporter molecule. In a typical electrochemical melting assay, the reporter molecule, such as Cy3, is covalently attached to the target strand through a long linker molecule to the sugar phosphate backbone. Thus, the position and orientation of the label relative to the sphere segment void (SSV) surface is poorly defined because the label group will be in constant motion. Recent research by the Brown group at the University of Southampton has shown that cyanine labels can also be attached to dsDNA through a modified thymine base. Utilising this type of synthetic modification, the linker group is significantly shorter and the cyanine label is believed to reside within the minor groove of the dsDNA. Some initial SERS experiments in which Cy3 was attached to the target strand utilising this labelling strategy gave SERS spectra that were significantly more intense than labelled targets that were prepared using the previous methodology (Figure 6.5). This suggests that not only is the position of the label better defined, but that the orientation relative to the surface is now more favourable as well.

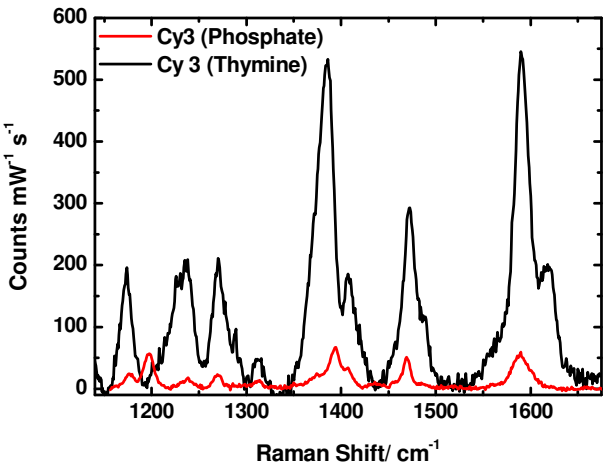

Figure 6.5. SERS spectra of cy-3 labelled surface-immobilised dsDNA. The label is either attached via a long linker to the end of the sugar-phosphate backbone (red line) or via a very short linker to a modified thymine base (black line). Spectra have been baseline corrected and normalised for acquisition times and laser power.

The resonance or (near resonance) of some molecules with the 633 nm laser employed for SERS measurements has often been exploited to improve the signal from an electrochemical melting assay over the course of this thesis. However, the reporter molecule chosen for use in electrochemical melting experiments has been limited to those that are commercially available. One area of potential future research is the custom design and synthesis of novel reporter molecules, either for synthetic attachment to the target strand or for use as non-covalent binding agents in label-free assays. For example, the ideal binding agent for a label-free electrochemical melting assay would be resonant with a 633 or 785 nm laser, non-fluorescent, not electrochemically active, and have a high selectivity for dsDNA over ssDNA.

Clearly, a great deal of further work is required before electrochemical melting can be optimised and the underlying science fully understood. Nevertheless, the exquisite capabilities of electrochemical melting for detecting changes in DNA structure have been demonstrated in extensive detail. The work presented in this thesis has laid down the foundations upon which a wide-range of applications for electrochemical melting can be developed in the future, spanning from medical diagnosis through to criminal forensics.

6.4. References

1. E. Palecek, *Collect. Czech. Chem. Commun.*, 1974, **39**, 3449 - 3460.
2. E. Palecek, *Bioelectrochem. Bioenerg.*, 1992, **28**, 71-83.
3. A. M. Brett, in *Bioelectrochemistry: Fundamentals, Experimental Techniques and Applications*, ed. P. N. Bartlett, John Wiley & Sons, Chichester, United Kingdom, 2008, pp. 411 - 442.
4. M. R. Arkin, Y. Jenkins, C. J. Murphy, J. N. Turro and J. K. Barton, in *Mechanistic Bioinorganic Chemistry*, eds. H. H. Thorp and V. L. Pecoraro, American Chemical Society, Washington DC, 1996, pp. 449-469.
5. S. Delaney and J. K. Barton, *J. Org. Chem.*, 2003, **68**, 6475-6483.
6. J. C. Genereux and J. K. Barton, *Chem. Rev.*, 2009, **110**, 1642-1662.
7. J. C. Genereux, A. K. Boal and J. K. Barton, *J. Am. Chem. Soc.*, 2010, **132**, 891-905.
8. A. A. Gorodetsky, M. C. Buzzeo and J. K. Barton, *Bioconjugate Chem.*, 2008, **19**, 2285-2296.
9. J. D. Slinker, N. B. Muren, S. E. Renfrew and J. K. Barton, *Nat Chem*, 2011, **3**, 228-233.
10. A. Paul, R. M. Watson, E. Wierzbinski, K. L. Davis, A. Sha, C. Achim and D. H. Waldeck, *J. Phys. Chem. B.*, 2009, **114**, 14140-14148.
11. R. Venkatramani, K. L. Davis, E. Wierzbinski, S. Bezer, A. Balaeff, S. Keinan, A. Paul, L. Kocsis, D. N. Beratan, C. Achim and D. H. Waldeck, *J. Am. Chem. Soc.*, 2010, **133**, 62-72.
12. M. u. A. Wolak, A. Balaeff, S. Gutmann, H. J. Helmrich, R. Vosloo, M. M. Beerbom, E. Wierzbinski, D. H. Waldeck, S. Bezer, C. Achim, D. N. Beratan and R. Schlaf, *J. Phys. Chem. C.*, 2011, **115**, 17123-17135.
13. V. Oklejas and J. M. Harris, *Langmuir*, 2003, **19**, 5794-5801.
14. V. Oklejas, C. Sjostrom and J. M. Harris, *J. Am. Chem. Soc.*, 2002, **124**, 2408-2409.
15. V. Oklejas, C. Sjostrom and J. M. Harris, *J. Phys. Chem. B.*, 2003, **107**, 7788-7794.
16. F. M. Huang, D. Wilding, J. D. Speed, A. E. Russell, P. N. Bartlett and J. J. Baumberg, *Nano Lett.*, 2011, **11**, 1221-1226.
17. J. D. Speed, R. P. Johnson, J. T. Hugall, N. N. Lal, P. N. Bartlett, J. J. Baumberg and A. E. Russell, *Chem. Commun.*, 2011, **47**, 6335-6337.